Atomic and Molecular Low-n Rydberg States in Supercritical Fluids

by

Luxi Li

A dissertation submitted to the Graduate Faculty in Chemistry
in partial fulfillment of the requirements
for the degree of Doctor of Philosophy,
The City University of New York.

2009

This manuscript has been read and accepted for the
Graduate Faculty in Chemistry in satisfaction of the
dissertation requirements for the degree of Doctor of Philosophy.

Date	Dr. Cherice M. Evans, Chair of Examining Committee
Date	Dr. Mahesh K. Lakshman, Executive Officer

Dr. Gary L. Findley

Dr. Seogjoo Jang

Dr. Lawrence W. Johnson
Supervisory Committee

THE CITY UNIVERSITY OF NEW YORK

Abstract

Atomic and Molecular Low-n Rydberg States in Supercritical Fluids

by

Luxi Li

Advisor: Dr. Cherice M. Evans

The structure of low-n Rydberg states doped into supercritical fluids represents an important probe to investigate solvation effects, especially near the solvent (or perturber) critical point. We have investigated the solvation of excited atomic and molecular dopants in various perturbing fluids (both atomic and molecular). This systematic study was performed from low perturber number densities to the density of the triple point liquid, at both non-critical temperatures and on an isotherm near the critical isotherm. Dopant low-n Rydberg states were investigated using vacuum ultraviolet photoabsorption spectroscopy. The absorption spectra of these states were then simulated using a semi-classical statistical line shape function. With accurate line shape simulations, the perturber induced energy shift of the primary transition was obtained using a standard moment analysis.

The moment analysis indicated that the dopant low-n Rydberg state energy blue shifts as a function of perturber number density without a significant temperature effect (except near the critical isotherm). A significant critical point effect was ob-

served in all dopant/pertuber systems investigated here. This critical point effect is caused by a large increase in the dopant/perturber radial distribution function near the critical temperature of the perturber. Since the first perturber solvent shell shields the cationic core, the binding energy of the optical electron decreases. This acts to increase the dopant low-n Rydberg state excitation energy. However, the overall blue shift and critical point effect varies from atomic to molecular perturber systems due to the structure of the perturber. These differences are also discussed in more detail in this work.

Acknowledgments

I wish to thank my major professor, Dr. Cherice M. Evans for all of her advice and guidance during the duration of this study. I wish to thank Dr. Gary L. Findley for giving so greatly of his expertise during both the data acquisition and the analysis required in this project. I wish to thank my Supervisory Committee Dr. Seogjoo Jang and Dr. Lawrence W. Johnson for the valuable yearly discussions. I wish to thank our group members Mr. Xianbo Shi and Ms. Gina M. Moriarty for all of their help in my experimental and theoretical work. I also wish to thank the staff at the University of Wisconsin Synchrotron Radiation Center for their help throughout these experimental studies.

All of the measurements presented here were performed at the University of Wisconsin Synchrotron Radiation Center (NSF DMR-0537588) in Stoughton, WI. This work was supported by grants to Dr. Cherice M. Evans from the Petroleum Research Fund (41378-G6) and the Professional Staff Congress of the City University of New York (PSC 60074-34 35, PSCREG-36-233, PSCREG-37-593, PSCREG-38-146, PSCREG-39-249), as well as by grants to Dr. Gary L. Findley from the Petroleum Research Fund (45728-B6) and the Louisiana Board of Regents (LEQSF(2006-09)-RD-A33). Special thanks are also extended to the Graduate Center of the City University of New York for providing numerous travel grants and small research grants

to support this work. Finally, I would like to thank the Queens College Department of Chemistry and Biochemistry for their support throughout the duration of this project.

Contents

1 Introduction **1**

2 Perturber effects on low-n Rydberg states **4**

2.1 Supercritical fluids 4

2.2 Rydberg states 8

2.3 Theoretical model 10

2.4 Previous studies 15

2.4.1 Xe in Ar, Ne and He 16

2.4.2 CH_3I in Ar and Kr 19

2.4.3 NO in Ar 20

3 Experiment and Modeling **24**

3.1 Experimental apparatus 24

3.2 Sample information and preparation 26

3.3 Data acquisition and analysis 33

3.4 Line shape simulations 36

3.4.1 Line shape function 36

3.4.2 Fast Fourier transform 37

3.4.3 Radial distribution function 39

3.4.4 Intermolecular potentials 41

4 Atomic perturbers **43**

4.1 Xe low-n Rydberg states in Ar 43

4.1.1 Xe absorption 43

4.1.2 Line shape simulations 46

4.1.3 Discussion 48

4.2 CH_3I low-n Rydberg states in Ar, Kr and Xe 53

4.2.1 CH_3I absorption 53

4.2.2 Line shape simulations 58

4.2.3 Discussion 61

4.3 Conclusions 72

5 Molecular perturbers **73**

5.1 Xe $6s$ Rydberg state in CF_4 73

5.2 CH_3I low-n Rydberg states in CH_4 76

5.3 CH_3I low-n Rydberg states in CF_4 82

5.4 Discussion 83

5.5 Autocorrelation function study 88

5.6 Conclusions 91

6 Conclusion **93**

References **105**

List of Tables

4.1 Intermolecular potential parameters for Xe in Ar. 46

4.2 Intermolecular potential parameters for CH_3I in atomic perturbers. . 60

5.1 Intermolecular potential parameters for Xe in CF_4. 74

5.2 Intermolecular potential parameters for CH_3I in CH_4. 78

5.3 Intermolecular potential parameters for CH_3I in CF_4. 82

6.1 A summary of the intermolecular potential parameters used in these studies. 96

List of Figures

2.1 The ratio of the local argon density to the bulk argon density around Ar and around CH_3I. 5

2.2 Typical behavior of the ratio of the average local density to the bulk density as a function of the bulk density. 6

2.3 Spectroscopic studies of various dopants in supercritical fluids. 7

2.4 Schematic presentation of an optical electron in a high-n Rydberg state orbital, a low-n Rydberg state orbital and a valence state orbital. D^+ is the dopant cationic core and P are the perturber particles. 9

2.5 An example of the absorbance of the Xe $6s$ and $6s'$ transitions doped into Ar. 17

2.6 Argon induced energy shifts for the Xe $6s$ and $6s'$ Rydberg transitions plotted as a function of argon number density. 18

2.7 An example of the absorbance of the CH_3I $6s$ and $6s'$ transitions doped into Ar. 19

2.8 Comparison of line shape simulations with experimental data for CH_3I in supercritical argon for selected perturber number densities. 21

2.9 Argon induced energy shifts for the NO valence and Rydberg transitions in comparison to the simulated energy shifts. 23

3.1 Schematic of the experimental endstation 25

3.2 Schematic of the copper experimental cell. 26

3.3 Schematic representation for a typical arrangement of the gas handling system. 27

3.4 Phase diagram of Ar. 28

3.5 Data analysis routine. 35

4.1 Selected absorption spectra for the Xe $6s$ Rydberg transition in Ar. . 44

4.2 Selected absorption spectra for the Xe $6s'$ Rydberg transition in Ar. . 44

4.3 A sample Xe $6s$ line shape simulation in Ar. 47

4.4 Comparison of the simulated line shapes with the Xe $6s$ absorption spectra in Ar. 49

4.5 Comparison of the simulated line shapes with the Xe $6s'$ absorption spectra in Ar. 50

4.6 The first moment of the Xe low-n Rydberg transitions in Ar. 51

4.7 Temperature study of the Xe $6s$ Rydberg transition near the argon critical point. 53

4.8 Selected absorption spectra for the CH_3I $6s$ Rydberg transition in Ar. 55

4.9 Selected absorption spectra for the CH_3I $6s$ Rydberg transition in Kr. 56

4.10 Selected absorption spectra for the CH_3I $6s$ Rydberg transition in Xe. 56

4.11 Selected absorption spectra for the CH_3I $6s'$ Rydberg transition in Ar. 57

4.12 Selected absorption spectra for the CH_3I $6s'$ Rydberg transition in Kr. 57

4.13 Selected absorption spectra for the CH_3I $6s'$ Rydberg transition in Xe. 58

4.14 A sample CH_3I $6s$ line shape simulation in Ar. 59

4.15 Comparison of the simulated line shapes with the CH_3I $6s$ absorption spectra in Ar. 62

4.16 Comparison of the simulated line shapes with the CH_3I $6s$ absorption spectra in Kr. 63

4.17 Comparison of the simulated line shapes with the CH_3I $6s$ absorption spectra in Xe. 64

4.18 Comparison of the simulated line shapes with the CH_3I $6s'$ absorption spectra in Ar. 65

4.19 Comparison of the simulated line shapes with the CH_3I $6s'$ absorption spectra in Kr. 66

4.20 Comparison of the simulated line shapes with the CH_3I $6s'$ absorption spectra in Xe. 67

4.21 The first moment of CH_3I $6s$ Rydberg transition in atomic perturbers. 69

4.22 The first moment of CH_3I $6s'$ Rydberg transition in atomic perturbers. 70

5.1 Comparison of the simulated line shapes with the Xe $6s$ absorption spectra in CF_4. 75

5.2 The first moment of the Xe $6s$ Rydberg transition in CF_4. 76

5.3 Comparison of the simulated line shapes with the CH_3I $6s$ absorption spectra in CH_4. 79

5.4 Comparison of the simulated line shapes with the CH_3I $6s'$ absorption spectra in CH_4. 80

5.5 The first moment of the CH_3I low-n Rydberg transitions in CH_4. . . . 81

5.6 Comparison of the simulated line shapes with the CH_3I $6s$ absorption spectra in CF_4. 84

5.7 Comparison of the simulated line shapes with the CH_3I $6s'$ absorption spectra in CF_4. 85

5.8 The first moment of the CH_3I low-n Rydberg transitions in CF_4. . . . 86

5.9 Dependence of the line shape of the CH_3I $6s$ Rydberg transition in CH_4 on the autocorrelation function. 90

5.10 Investigation of the dependence of the first moment on the autocorrelation function. 91

Chapter 1

Introduction

Supercritical fluids, especially molecular supercritical fluids, have been used increasingly in industrial [1–6] and environmental [1, 7–10] applications. Due to their special properties (e.g., high compressibility), supercritical fluids are often used in continuous extractions [2–4, 8], in improving the separation of compounds in chromatography [7, 10, 11], in catalysis [12–15] and polymerization [16, 17], and in the control of chemical reaction products [14, 18–20]. Therefore, investigation of the structure of supercritical binary systems (i.e., dilute dopant/supercritical perturber systems) is very important for studying solvation effects and photochemistry.

Since electronic excited states are sensitive to the local fluid environment, dopant electronic transitions in supercritical fluids are an appropriate probe to study the structure of supercritical fluids, especially near the critical point. In comparison to valence states, Rydberg states are more sensitive to their environment [21]. However, high-n Rydberg states are usually too sensitive to perturber density fluctuations, which makes these individual dopant states impossible to investigate. (Nevertheless, under the assumption that high-n Rydberg states behave similarly to the ionization threshold of the dopant, dopant high-n Rydberg state behavior in supercritical fluids can be probed indirectly by studying the energy of the quasi-free electrons, through

photoinjection [22–31] and field ionization [32–39].) Low-n Rydberg states, on the other hand, are excellent spectroscopic probes to investigate excited state/fluid interactions.

The study of low-n Rydberg states in supercritical fluids began with the photoabsorption of alkali metals in rare gas fluids [40, 41]. Later researchers expanded the investigation into rare gas dopants in supercritical rare gas fluids [42–46], and molecular dopants in atomic and molecular perturber fluids [47–56]. However, none of these previous groups studied dilute solutions near the critical point of the solvent. (The single theoretical study of a low-n Rydberg state in a supercritical fluid near the critical point was performed by Larrégaray, *et al.* [55]; this investigation predicted a change in the line shape and in the perturber induced shift of the Rydberg transition.) These results from previous experimental and theoretical investigations of low-n Rydberg states in dense gases are reviewed in in Chapter 2.

In this dissertation, we have systematically investigated the photoabsorption of atomic and molecular dopant low-n Rydberg transitions in supercritical fluids [57–59]. The individual systems probed allowed us to investigate atomic/atomic interactions (i.e., Xe/Ar), molecular/atomic interactions (i.e., CH_3I/Ar, CH_3I/Kr, CH_3I/Xe), atomic/molecular interactions (i.e., Xe/CF_4) and molecular/molecular interactions (i.e., CH_3I/CH_4 and CH_3I/CF_4). Our studies begin with the measurement of perturber density and temperature effects on the absorption spectra of dopant low-n Rydberg transitions using vacuum ultraviolet spectroscopy. A semi-classical statistical line shape analysis is then used to simulate the experimental spectra. The experimental techniques and theoretical methodology are discussed in Chapter 3. Chapter

4 presents our experimental and theoretical results for low-n atomic and molecular Rydberg states in atomic supercritical fluids. The accuracy of the line shape analysis is demonstrated and the results are then used to obtain the perturber-induced energy shifts of the primary low-n Rydberg transitions. A striking critical point effect in this energy shift is observed for all of the dopant/perturber systems presented here. A discussion of the ways in which the dopant/perturber interactions influence in the perturber-induced energy shift is also presented in Chapter 4.

In Chapter 5 we present absorption spectra of atomic and molecular low-n Rydberg transitions in molecular perturbers [59], and we then extend our semi-classical line shape analysis to the investigation of electronic transitions in molecular perturbers. The accuracy of the line shape analysis again allows us to obtain the perturber-induced energy shift of the primary electronic transition investigated. Using this shift, we then highlight how the behavior of electronic transitions in a molecular perturber differs from that in atomic perturbers, and we demonstrate that a critical point effect is still apparent. A discussion of the origin of the differences observed in atomic and molecular perturbers is then presented. We conclude with an explanation of the importance of the inclusion of three-body interactions in the line-shape analysis, and with a discussion of how this model will change when dealing with non-spherical perturbers and polar fluids.

Chapter 2

Perturber effects on low-n Rydberg states

2.1 Supercritical fluids

A supercritical fluid (SCF) is a fluid at a temperature higher than its critical temperature and, therefore, has properties of both a liquid and a gas [20, 60]. For example, SCFs have the large compressibility characteristic of gases, but the potential to solvate materials like a liquid. Near the critical point, the correlation length of perturber molecules becomes unbounded, which induces an increase in local fluid inhomogeneities [20, 60]. This change in the local density of a fluid is currently being used to explain the small size distributions in nanoparticles synthesized in SCF solvents [61–64]. However, to fully understand the mechanism of nanoparticle formation, a better understanding of solute/solvent interactions in SCFs, especially near the critical point, must first be developed.

The local density $\rho(r)$ of a perturbing fluid around a central species (either the dopant or a single perturber) is defined by [65, 66]

$$\rho(r) \;=\; g(r)\,\rho\;,$$

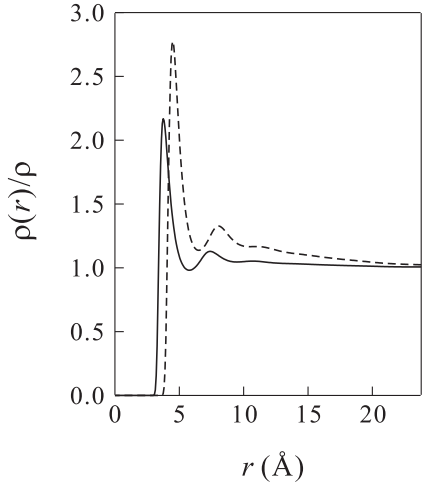

Figure 2.1: The ratio of the local argon density $\rho(r)$ to the bulk argon density ρ around (—) Ar and around (- - -) CH_3I at a bulk argon number density of 8.20×10^{21} cm^{-3}. Notice the two areas of enhancement indicative of the presence of solvent shells in the SCF. See Chapter3 for details of these calculations.

where $g(r)$ is the radial distribution function and ρ is the bulk density. For neat fluids and for most dilute dopant/perturber systems, the interactions between the species in the system are attractive in nature. Thus, the perturber forms at least one solvent shell around the dopant (or a central perturber). An example of the increase in local density caused by these solvent shells is shown in Fig. 2.1. As the dilute dopant/perturber system approaches the critical density and temperature of the perturber, the intermolecular interactions increase. This increase leads to a change in the behavior of the local density as a function of the bulk density, which is schematically shown in Fig. 2.2. Therefore, the changes in SCF properties near the critical point are due to the higher correlation between the species in the fluid. These intermolecular correlations are usually probed spectroscopically by dissolving a dopant molecule in the SCF. Since electronic excited states are incredibly sensitive

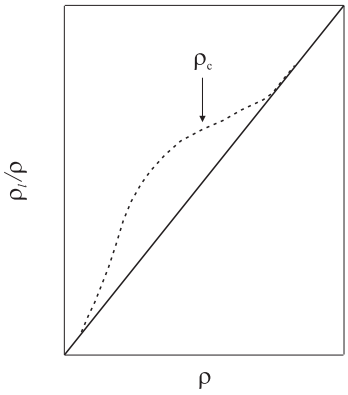

Figure 2.2: Typical behavior of the ratio of the average local density $\rho_\ell = g_{\max}\rho$ to the bulk density ρ as a function of the bulk density for (—) non-critical temperatures and for (- - -) the critical isotherm. Notice the significant enhancement near the critical density ρ_c along the critical isotherm. This increase is caused by increased intermolecular interactions. Adapted from [60].

to local fluid environment, changes in the fluid environment can be investigated using changes in the absorption or emission of the dopant.

Fig. 2.3 gives three example spectroscopic studies of a dopant in an SCF near the critical density and temperature of the fluid. Fig 2.3a shows the energy position of an anthracene emission line for anthracene doped into supercritical carbon dioxide near the critical isotherm and density of the perturber [67]. Unfortunately, no emission data on non-critical isotherms were taken in this fluorescence emission study. However, the maximum emission position shows a striking critical effect in comparison to a calculated baseline. A more complete investigation of temperature effects on the local density of SCFs via UV photoabsorption [68] of ethyl p-(N,N-dimethylamino)benzoate (DMAEB) in supercritical CHF_3 is presented in Fig. 2.3b for three isotherms near the critical isotherm. The isotherms shown are at the reduced temperature T_r [where $T_r \equiv T/T_c$ with T_c being the critical temperature of the fluid] of 1.01, 1.06 and 1.11. Although the three isotherms are evenly spaced, the

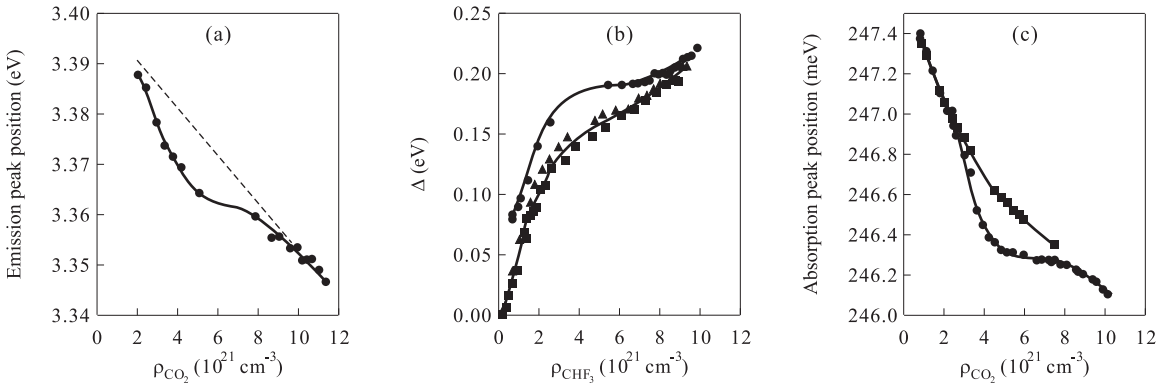

Figure 2.3: (a) The energy of fluorescence emission for (•) anthracene doped into supercritical carbon dioxide at a reduced temperature $T_r \simeq 1.01$ plotted as a function of carbon dioxide number density ρ_{CO_2}. The dashed line (- - -) is a reference line calculated using perturber bulk densities. Adapted from [67]. (b) The perturber induced energy shifts of the photoabsorption maximum for DMAEB doped into supercritical CHF_3 at (•) 30.0°C [i.e., $T_r \simeq 1.01$], (▲) 44.7°C, and (■) 59.6°C, plotted as a function of CHF_3 number density ρ_{CHF_3}. Adapted from [68]. (c) The energy position of infrared absorption for the $W(CO)_6$ CO stretching mode in supercritical carbon dioxide at (•) 33°C [i.e., $T_r \simeq 1.01$] and at (■) 50°C, plotted as a function of ρ_{CO_2}. Adapted from [69, 70]. The solid lines in (a) - (c) are provided as a visual aid.

photoabsorption shifts are very similar on the $T_r = 1.06$ and $T_r = 1.11$ isotherms, while the shift on the $T_r = 1.01$ isotherm is significantly different. Therefore, the perturber induced shift is only temperature sensitive near the critical point of the perturber. Urdahl, *et al.* [69, 70] studied the $W(CO)_6$ T_{1u} asymmetric CO stretching mode doped into supercritical carbon dioxide, ethane and trifluoromethane by IR photoabsorption. All three systems show similar behavior, an example of which is presented in Fig. 2.3c. Again, the absorption band position changes significantly along the critical isotherm near the critical density. However, extracting the data presented in Fig. 2.3 is difficult. Moreover, most of the previous work [60] has used dopant valence transitions as probes, and these states tend to be less sensitive to local environments [21]. In the present work, we will investigate SCFs near the crit-

ical point of the fluid by using low-n Rydberg state transitions as the probe. Since Rydberg states are hydrogen-like, it should be possible to model these states within the statistical mechanical theory of spectral line-broadening.

2.2 Rydberg states

Rydberg states are highly excited electronic states in which the optical electron is so distant from the cationic core that the core appears to the electron as a massive point charge. These states are defined by the excitation energy

$$E_n \;=\; I \;-\; \frac{R_y}{(n \;-\; \mu_\ell)^2} \;, \tag{2.1}$$

where I is the dopant ionization energy, R_y is the Rydberg constant (i.e., 13.606 eV), n is the principal quantum number, and μ_ℓ is the angular momentum (ℓ) dependent quantum defect. Rydberg state orbitals have an average radius of $a_0 n^2$ (where $a_0 \simeq$ 0.53 Å). A high-n Rydberg state optical electron is spatially distant from the cationic core and, therefore, does not interact with the core electrons. Within a semi-classical approximation, high-n Rydberg electrons tend to have circular orbits [71]. A low-n Rydberg state optical electron, especially one with low angular momentum, tends to interact more strongly with the cationic core. Thus, in a semi-classical approximation, low-n Rydberg electrons tend to have elliptic orbits [71].

One significant difference between valence transitions and Rydberg transitions is the disparate behavior when these excited states interact with a perturber fluid [21]. Valence transitions tend to show only slight changes in energy position (cf. Fig. 2.3, for example) and line shape broadening. Moreover, the line shape broadening tends to be symmetric. Rydberg transitions, however, show a significant energy shift and

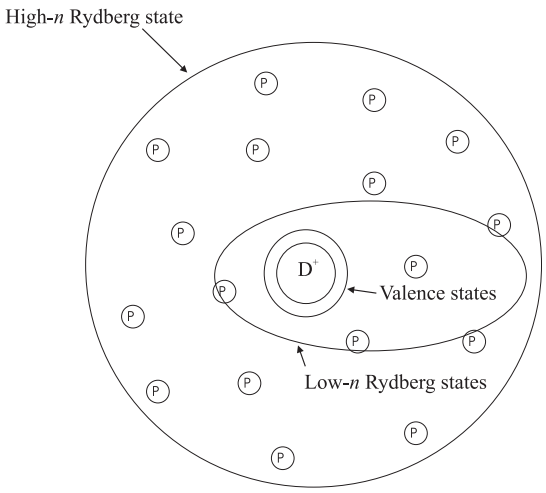

Figure 2.4: Schematic presentation of an optical electron in a high-n Rydberg state orbital, a low-n Rydberg state orbital and a valence state orbital. D^+ is the dopant cationic core and P are the perturber particles.

asymmetric line shape broadening. Fig. 2.4 shows a schematic of a dopant atom interacting with a perturbing fluid. The valence orbitals are spatially close to the dopant cationic core and, therefore, do not sample as much of the perturbing fluid as do Rydberg orbitals. The low-n and high-n Rydberg optical electrons both have orbitals that are spatially distant from the cationic core. Thus, these orbitals are shielded from the Coulomb potential of the core by the structure of the perturbing fluid. The higher the n of the Rydberg state, the stronger the shielding by the perturber fluid. In fact, the high-n Rydberg states are so sensitive to perturber density [21] that these states broaden too much to be used as spectroscopic probes for electronic excited states in SCFs. (Nevertheless, field ionization of these states can be used as a source of quasi-free electrons in studies of fluid conduction [32–39].) Since, low-n Rydberg states are more sensitive than valence transitions, but not as sensitive as high-n Rydberg states, they serve as excellent spectroscopic probes to investigate excited state/fluid interactions. Moreover, since a low-n Rydberg orbital can more strongly mix with

the cationic core, the perturber effects on these excited state transitions will depend both upon the perturber and upon the dopant. Thus, the perturber-dependent energy shift should be sensitive to the ground-state and excited-state dopant/perturber intermolecular potentials, which implies that a spectroscopic study of low-n Rydberg states in dense and supercritical fluids can probe the intermolecular potential energy surface.

2.3 Theoretical model

Due to the hydrogenic properties of Rydberg states, the optical electron is in general insensitive to the structure of the cationic core. Therefore, both atomic and molecular Rydberg transitions can be modeled within the same theory. In a very dilute dopant/perturber system, assuming that the dopant Rydberg transition is at high energy [i.e. $\beta\,(E_g - E_e) \gg 1$, $\beta = 1\,/\,(k\,T)$], the Schrödinger equation is

$$H|\Psi\rangle = E|\Psi\rangle\ , \tag{2.2}$$

where the eigenfunction $|\Psi\rangle$ is a product of the dopant electronic wavefunction $|\alpha\rangle$ and the individual perturber wavefunctions $|\psi_i;\,\alpha\rangle$. The Hamiltonian H in eq. (2.2) is the sum of several individual Hamiltonians, namely the Hamiltonian for the free dopant, the Hamiltonian for the free perturber, and the Hamiltonian for the dopant/perturber intermolecular correlation. The Hamiltonian $H_{\rm FD}$ for the free dopant is [72]

$$H_{\rm FD} = \sum_{\alpha} E_\alpha |\alpha\rangle\langle\alpha|\ , \tag{2.3}$$

where $\alpha = e, g$ with e and g representing the excited state and ground state of the free dopant. The Hamiltonian $H_{\rm FP}$ for the free non-interacting perturber is given by [72]

$$H_{\rm FP} \;=\; -\sum_{i}^{N} \frac{\hbar^2}{2\,m}\,\nabla_i^2\;, \tag{2.4}$$

where N is the total number of perturbing atoms in the range of the Rydberg optical electron. Finally, the Hamiltonian $H_{\rm PD}$ for the intermolecular interaction is [72]

$$H_{\rm PD} \;=\; \sum_{\alpha}\sum_{i}\left[V_\alpha(r_i) \;+\; V'(r_i)\right]\,|\Psi\rangle\langle\Psi|\;, \tag{2.5}$$

where $V(r)$ is the dopant/perturber intermolecular potential, and $V'(r)$ is the perturber/perturber intermolecular potential. Therefore, the total Hamiltonian H is [72]

$$H \;=\; H_{\rm FD} \;+\; H_{\rm FP} \;+\; H_{\rm PD}\;, \tag{2.6}$$

which can be rewritten as a ground state Hamiltonian H_g and an excited state Hamiltonian H_e.

The absorption coefficient function is given as the Fourier transform [72]

$$\mathfrak{L}(\omega) \;\equiv\; \frac{1}{2\,\pi}\int_{-\infty}^{\infty} dt\;{\rm e}^{-i\,\omega\,t}\;\langle\;\overrightarrow{\mu}(0)\;\cdot\;\overrightarrow{\mu}(t)\;\rangle\;, \tag{2.7}$$

where the autocorrelation function (i.e., $\langle\cdots\rangle$) is the thermal average of the scalar product of the dipole moment operator (i.e., $\overrightarrow{\mu}$) of the dopant at two different times. This autocorrelation function can be resolved within the Liouville operator formalism to give [72]

$$\langle\;\overrightarrow{\mu}(0)\;\cdot\;\overrightarrow{\mu}(t)\;\rangle \;\equiv\; \exp\left[\rho_{\rm P}\,\langle{\rm e}^{i\,L_g\,t}\;-\;1\rangle_g\right]\;, \tag{2.8}$$

where the two-body Liouville operator L_g is defined by

$$L_g\,\Omega \;=\; H_e\,\Omega \;-\; \Omega\,H_g \;=\; [H_g,\,\Omega] \;+\; (E_e \;-\; E_g)\,\Omega\;, \tag{2.9}$$

where Ω is an arbitrary operator. However, if lifetime broadening is neglected, only the dopant/perturber interaction and the dopant electronic energy change during the transition. Therefore, the autocorrelation function can be rewritten as [72]

$$\langle\; \overrightarrow{\mu}(0) \;\cdot\; \overrightarrow{\mu}(t)\;\rangle \;\equiv\; \mathrm{e}^{i\,\omega_0\,t}\;\exp\left[\rho_{\mathrm{P}}\,\langle \mathrm{e}^{i\,\Delta V\,t} \;-\; 1\,\rangle_g\,\right]\;, \tag{2.10}$$

where ω_0 is the transition frequency of the neat dopant, ρ_{P} is the perturber density, and $\Delta V \;=\; V_e - V_g$, with V_e and V_g being the excited-state dopant/ground-state perturber and ground-state dopant/ground-state perturber intermolecular potentials, respectively.

In semi-classical line shape theory, the line shape function for an allowed transition is given by [40],

$$\mathfrak{L}(\omega) \;=\; \frac{1}{2\,\pi}\int_{-\infty}^{\infty} dt\;\mathrm{e}^{-i\,[\omega(\mathbf{R})\,-\,\omega_0]\,t}\;\;\frac{Z\,(\beta\,V_g \;+\; i\,t\,\Delta V)}{Z\,(\beta\,V_g)}\;, \tag{2.11}$$

where Z is the partition function and $\mathbf{R}$ denotes the collection of all dopant/perturber distances. Under the classical fluid approximation [73], the autocorrelation function $\Phi(t)$ is given by a density expansion [40]

$$\Phi(t) \;=\; \ln Z\,(\beta\,V_g \;+\; i\,t\,\Delta V) \;-\; \ln Z\,(\beta\,V_g) \;=\; A_1(t) \;+\; A_2(t) \;+\; \cdots\;, \tag{2.12}$$

where [40, 45]

$$A_n(t) \;=\; \frac{1}{n!}\int\cdots\int\,\prod_{j=1}^{n} d^3R_j\;\mathfrak{F}(\mathbf{R}_1,\ldots,\mathbf{R}_n) \\ \times\;\prod_{j=1}^{n}\;[\exp(-i\;\Delta V(\mathbf{R}_j)\;t)\;-\;1] \quad . \tag{2.13}$$

In eq. (2.13), $\mathfrak{F}(\mathbf{R}_1,\ldots,\mathbf{R}_n)$ is the Ursell distribution function [45,46,73], and $\Delta V(\mathbf{R}) = V_e(\mathbf{R}) - V_g(\mathbf{R})$. The Ursell distribution function for two body interactions [45, 46] is $\mathfrak{F}(\mathbf{R}) = \rho_{\rm P}\; g_{\rm PD}(\mathbf{R})$, where $g_{\rm PD}(\mathbf{R})$ is the perturber/dopant radial distribution function. The three body Ursell distribution function is estimated using the Kirkwood superposition approximation [74] to be

$$\mathfrak{F}(\mathbf{R}_1,\mathbf{R}_2) \;=\; \rho_{\rm P}^2\;[\,g_{\rm PP}(|\mathbf{R}_1\;-\;\mathbf{R}_2|)\;-\;1\,]\;g_{\rm PD}(\mathbf{R}_1)\;g_{\rm PD}(\mathbf{R}_2)\;, \tag{2.14}$$

where $g_{\rm PP}(\mathbf{R})$ is the perturber/perturber radial distribution function. The density expansion terms are multibody interactions between dopant and perturber over all space. $A_1(t)$ is the dopant/perturber two-body interaction, $A_2(t)$ is the dopant/perturber three-body interaction, and $A_n(t)$ is the dopant/perturber $n+1$ body interaction. Substitution of these Ursell distribution functions into eq. (2.13) under the assumption of spherically symmetric potentials, gives [45, 46, 57]

$$A_1(t) \;=\; 4\,\pi\,\rho_{\rm P}\int_0^\infty dr\;r^2\;g_{\rm PD}(r)\,[\;{\rm e}^{-\,i\,t\,\Delta V(r)}\;-\;1\;] \quad , \tag{2.15}$$

and

$$A_2(t) \;=\; 4\,\pi\,\rho_{\rm P}^2\int_0^\infty dr_1\;r_1^2\;g_{\rm PD}(r_1)\;\left[{\rm e}^{-\,i\,t\,\Delta V(r_1)}\;-\;1\,\right] \\ \times\;\int_0^\infty dr_2\;r_2^2\;g_{\rm PD}(r_2)\;\left[\;{\rm e}^{-\,i\,t\,\Delta V(r_2)}\;-\;1\;\right] \\ \times\;\frac{1}{r_1\;r_2}\;\int_{|r_1-r_2|}^{|r_1+r_2|} s\;[\;g_{\rm PP}(s)\;-\;1\;]\,ds\;. \tag{2.16}$$

Since the strength of the interaction decreases as the number of bodies involved increases, and since higher order interactions are more difficult to model, most line shape simulations are truncated at the second term $A_2(t)$.

The autocorrelation function can be written as a power series expansion at $t = 0$, namely [41, 72, 75, 76]

$$\Phi(t) \;=\; \sum_{n=1}^{\infty} \frac{i^n}{n!}\, m_n\, t^n \;, \tag{2.17}$$

where the expansion coefficients m_i are given by

$$m_n \;=\; \frac{1}{(\sqrt{-1})^n} \;\; \frac{d^n}{dt^n} \Phi(t) \,\Big|_{t\,=\,0} \;. \tag{2.18}$$

Using eq. (2.12) with $A_1(t)$ and $A_2(t)$ from eqs. (2.15) and (2.16), the first two expansion coefficients become [45]

$$m_1 \;=\; -\,4\,\pi\,\rho_{\rm P} \int_0^{\infty} dr\; r^2\; g_{\rm PD}(r)\; \Delta V(r) \;, \tag{2.19}$$

and

$$\begin{aligned} m_2 \;=& \, m_1^2 \;+\; 4\,\pi\,\rho_{\rm P} \int_0^{\infty} dr\; r^2\; g_{\rm PD}(r)\; \Delta V(r)^2 \\ &+\; 8\,\pi^2\; {\rho_{\rm P}}^2 \int_0^{\infty} \int_0^{\infty} dr_1\; dr_2\; r_1\; r_2\; g_{\rm PD}(r_1)\; g_{\rm PD}(r_2) \\ &\times\; \Delta V(r_1)\; \Delta V(r_2) \int_{|r_1\,-\,r_2|}^{|r_1\,+\,r_2|} s\; [\; g_{\rm PP}(s) \;-\; 1\;]\; ds \;. \end{aligned} \tag{2.20}$$

The above expansion coefficients are equivalent to the moments of the optical coefficient, which are defined by [45]

$$m_n \;=\; \int \mathfrak{L}(E)\; E^n\; dE \;. \tag{2.21}$$

Thus, the perturber induced shift $\Delta(\rho_{\rm P})$ in the energy position of the optical coefficient maximum is [45, 46]

$$\Delta(\rho_{\rm P}) \;=\; M_1 \;=\; \frac{m_1}{m_0} \;=\; \int \mathfrak{L}(E)\, E\, dE \Big/ \int \mathfrak{L}(E)\, dE \;\;, \tag{2.22}$$

while the full-width-half-maximum of the experimental absorption spectrum is proportional to

$$M_2 \;=\; \left[\frac{m_2}{m_0} - M_1^2\right]^{1/2} \;=\; \left[\left(\int \mathfrak{L}(E)\, E^2\, dE \Big/ \int \mathfrak{L}(E)\, dE\right) \;-\; M_1^2\right]^{1/2} \;\;, \tag{2.23}$$

where $\mathfrak{L}(E)$ is the absorption band for the transition and $E = \hbar(\omega - \omega_0)$ [$\hbar \equiv$ reduced Planck constant].

2.4 Previous studies

The interaction of dopant low-n Rydberg states doped with supercritical fluids has previously been the subject of some interest both experimentally and theoretically [21, 42–56]. The first detailed investigation of these interactions was a study of Xe low-n Rydberg states doped into the dense rare gas fluids (i.e., argon, neon and helium) by Messing, *et al.* [45, 46]. In the same year, Messing, *et al.* [47, 48] presented their studies of molecular low-n Rydberg states in dense Ar and Kr. A decade later, Morikawa, *et al.* [54] investigated the NO valence and low-n Rydberg state transitions in dense argon and krypton. All of these experiments [45–48, 54] used a basic moment analysis of absorption bands to obtain the energy shifts of these bands as a function of perturber number density. The photoabsorption energy shifts were then simulated [45–48, 54] using eq. (2.19) for various assumptions of intermolecular potentials and radial distribution functions. Messing, *et al.* also performed line shape simula-

tions under the assumption of a Gaussian line shape [45–48] for selected perturber number densities. As molecular dynamics developed, research groups [50,51,53,55,56] returned to absorption line shape simulations in an attempt to match the asymmetric broadening observed experimentally. We will summarize the results of these studies below.

2.4.1 Xe in Ar, Ne and He

When Xe $6s$ and $6s'$ Rydberg state transitions are excited in the presence of low density supercritical argon or krypton, satellite bands appear on the higher energy wing of the absorption or emission spectra [42–44]. These blue satellite bands increase with increasing perturber density [42–44] and with decreasing temperature. Therefore, Castex, *et al.* [42–44] concluded that these blue satellites are caused by the formation of dopant/perturber ground state and excited state dimers. An example of the Xe $6s$ and $6s'$ Rydberg transitions in the presence of argon is shown in Fig. 2.5. The primary Xe absorption transition, or [57]

$$\mathrm{Xe} \; + \; h\nu \quad \stackrel{\mathrm{Ar}}{\longrightarrow} \quad \mathrm{Xe}^* \; , \tag{2.24}$$

is indicated in Fig. 2.5 as a. The XeAr dimer transitions that yield the blue satellite bands are [42–44]

$$\mathrm{XeAr} \; + \; h\nu \quad \stackrel{\mathrm{Ar}}{\longrightarrow} \quad \mathrm{Xe}^* \; + \; \mathrm{Ar} \; , \tag{2.25}$$

and

$$\mathrm{XeAr} \; + \; h\nu \quad \stackrel{\mathrm{Ar}}{\longrightarrow} \quad \mathrm{Xe}^*\mathrm{Ar} \; . \tag{2.26}$$

These transitions are indicated in Fig. 2.5 as b and c, respectively.

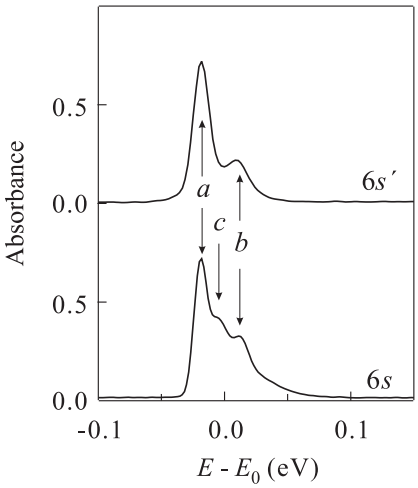

Figure 2.5: Photoabsorption spectra (relative units) of the Xe $6s$ and $6s'$ transitions doped into Ar at an argon number density of $\rho_{\mathrm{Ar}} = 1.47\times10^{21}$ cm^{-3} and a temperature of 23.6°C. a corresponds to eq. (2.24), b to eq. (2.25), and c to eq. (2.26). For the $6s$ Rydberg state $E_0 = 8.437$ eV and for the $6s'$ Rydberg state $E_0 = 9.570$ eV. Data from the present work.

Detailed investigations [45] of the Xe $6s$ Rydberg state doped in supercritical argon indicated that the energy position at the photoabsorption peak maximum shifted slightly to the red at low argon density and then strongly to the blue (cf. Fig. 2.6a). Similar results, which are shown in Fig. 2.6b, were then observed for the Xe $6s'$ Rydberg states in supercritical argon [46]. These studies [45, 46] concluded that both the perturber-induced energy shift and the line shape broadening were temperature independent. However, since the blue satellite bands grow and broaden as a function of perturber number density, the energy position of the maximum absorption (or the first moment from a moment analysis) is not an accurate energy position for the primary Xe Rydberg transition. Thus, modeling the experimental first moment M_1 and second moment M_2 using eqs. (2.20) and (2.21) required three groups of intermolecular potential parameters for different perturber density ranges.

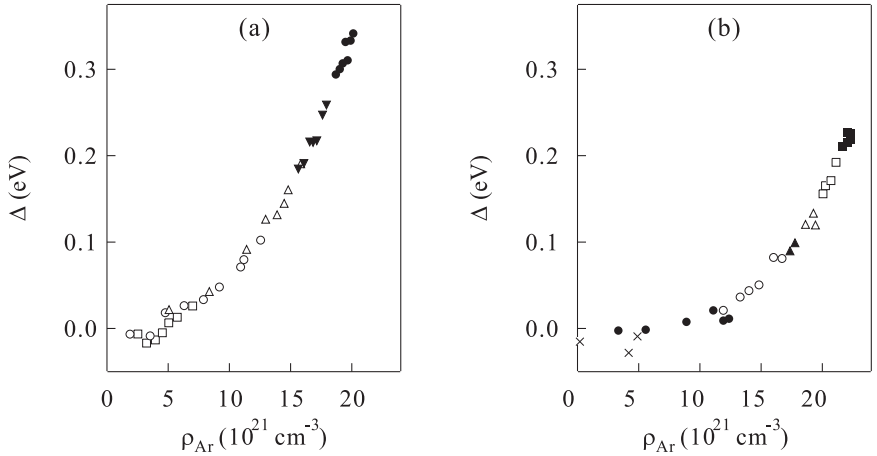

Figure 2.6: The perturber induced shift Δ of (a) the Xe $6s$ [45] and (b) the Xe $6s'$ [46] absorption maximum plotted as a function of argon number density ρ_{Ar} at different temperatures. In (a), the markers are (□) 25°C; (○) −83°C; (△) −118°C; (▼) −138°C; and (●) −163°C. In (b), the markers are for temperature ranges of (×) −23°C to 27°C; (●) −93°C to −63°C; (○) −123°C to −113°C; (▲) −138°C to −128°C; (△) −158°C to −148°C; (□) −173°C to −163°C; and (■) −186°C to −178°C.

The Xe $6s$ and $6s'$ Rydberg transitions [46] in supercritical helium and neon show a similar perturber density dependence as that shown in Fig. 2.6. However, these two systems do not form ground state or excited state dimers and, therefore, do not have blue satellite bands. Thus, the moment analysis of the photoabsorption spectra presented a more accurate perturber induced shift as a function of perturber number density. Because of the simplicity of the absorption bands, Messing, *et al.* [46] simulated the line shapes of the Xe $6s$ and $6s'$ transitions in both helium and neon at a single perturber number density using eqs. (2.11) and (2.12). These simulations indicated that an accurate line shape could be obtained without blue satellite bands [46]. Unfortunately, no temperature dependence was reported in these papers [45,46].

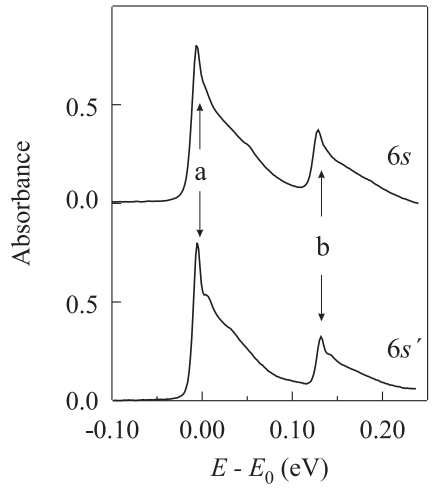

Figure 2.7: Photoabsorption spectra (relative units) of the CH_3I $6s$ and $6s'$ transitions doped into Ar at an argon number density of $\rho_{Ar} = 1.89\times10^{21}$ cm^{-3} and a temperature of -79.8°C. *a* corresponds to eq. (2.27) and *b* to eq. (2.28). For the $6s$ Rydberg state $E_0 = 6.154$ eV and $E_0 = 6.767$ eV for the $6s'$ Rydberg state. Data from the present work.

2.4.2 CH_3I in Ar and Kr

Since CH_3I is a molecular dopant, vibrational transitions as well as adiabatic transition appear in the photoabsorption spectra. The adiabatic transition is given by [57]

$$CH_3I + h\nu \longrightarrow CH_3I^* , \tag{2.27}$$

denoted *a* in Fig. 2.7, as well as one quantum of the CH_3 deformation vibrational transition ν_2 in the excited state, or

$$CH_3I + h\nu \longrightarrow CH_3I^* (\nu_2) , \tag{2.28}$$

denoted *b*, in Fig. 2.7. Although vibrational transitions are apparent, CH_3I [47–49,52] has been investigated extensively because of the "atomic" like nature of the adiabatic $6s$ and $6s'$ Rydberg transitions. Messing, *et al.* [47, 48] extracted the perturber dependent shift $\Delta(\rho_P)$ of the CH_3I $6s$ and $6s'$ Rydberg states by performing a moment

analysis on the photoabsorption bands using eq. (2.22). This analysis indicated that $\Delta(\rho_P)$ tended first to lower energy and then to higher energy as ρ_P increased from low density to the density of the triple-point liquid, similar to the trends shown in Fig. 2.6 for Xe in Ar. However, Messing, *et al.* [47, 48] did not explore critical temperature effects on $\Delta(\rho_P)$, nor did they correctly account for the vibrational bands on the blue side of the adiabatic Rydberg transition. Messing, *et al.* [48] did attempt to model the CH_3I $6s$ Rydberg transition in argon using a semi-classical statistical line shape function under the assumption that the adiabatic and vibrational transitions have exactly the same line shapes, although no comparison between the experimental spectra and the simulated line shapes was provided. Later researchers [50–53] concentrated on the simulation of the CH_3I $6s$ Rydberg state doped into argon using both molecular dynamics and semi-classical integral methods. Egorov, *et al.* [53] showed that the semi-classical integral method can yield results comparable to the molecular dynamics calculations of Ziegler, *et al.* [50–52]. Comparing the semi-classical method and molecular dynamics simulation to experimental spectra (cf. Fig. 2.8) shows that both methods can be used to simulate the experimental spectra with an appropriate choice of intermolecular potentials.

2.4.3 NO in Ar

Morikawa, *et al.* [54] investigated valence and low-n Rydberg transitions doped into supercritical argon. They used eq. (2.22) to determine the perturber induced shift $\Delta(\rho_P)$ for several low-n Rydberg transitions as well as a valence transition. Under the assumption of spherically symmetric potentials for the ground and excited states of the NO/Ar systems, an accurate moment analysis using eq. (2.19) was performed

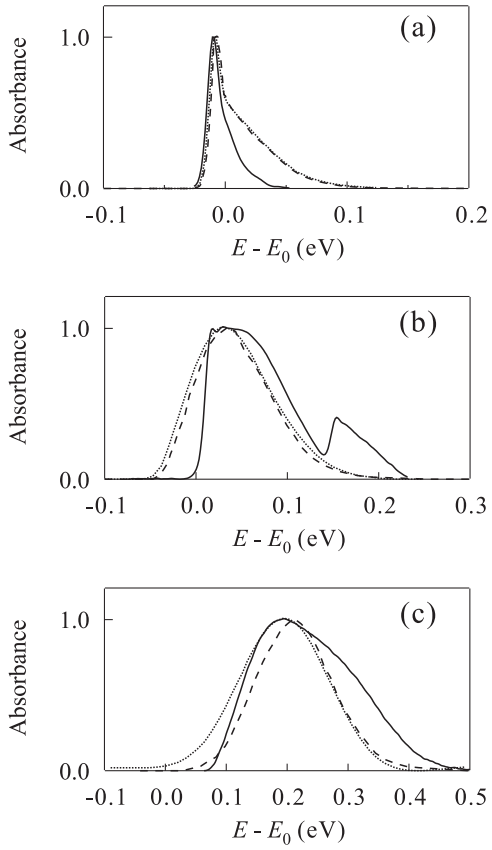

Figure 2.8: The line shape simulation of the CH_3I 6s transition doped into supercritical argon using (- - -) a semi-classical line shape function data [53] and using ($\cdots$) molecular dynamics [52] in comparison to (—) the photoabsorption spectra at (a) $\rho_{\mathrm{Ar}} = 2.0 \times 10^{21}$ cm^{-3}, (b) $\rho_{\mathrm{Ar}} = 7.6 \times 10^{21}$ cm^{-3}, and (c) $\rho_{\mathrm{Ar}} = 2.0 \times 10^{22}$ cm^{-3}. Experimental data are from the present work.

(cf. Fig. 2.9). In The NO valence state transition (cf. Fig. 2.9a) shows a slight perturber-induced red shift, which differs significantly from the obvious blue shift of the low-n NO Rydberg state transitions shown in Figs. 2.9b and c. Fig. 2.9 also shows that low-n Rydberg states make a more sensitive probe to perturber effects than valence transitions. Later groups [55,56] did line shape simulations to model the experimental spectra. Larrégaray, *et al.* [55] measured the NO $3s\sigma$ transition doped into supercritical argon at selected argon densities. Then, using molecular dynamics they successfully modeled the line shape of the transition. Once the intermolecular potentials and boundary conditions for the molecular dynamics simulations had been set against experimental data, Larrégaray, *et al.* [55] calculated the line shape for NO in Ar at the critical density and temperature. These calculations predicted that the photoabsorption peak maximum position would shift to the blue when argon was near its critical point. Later, Egorov, *et al.* [56] showed that similar results could be obtained using semi-classical approximation. Therefore, line shape simulations using molecular dynamics and semi-classical line shape theory show comparable results.

We will use the semi-classical integral theory (introduced in Section 2.3 and expanded in detail in Section 3.4) to systematically model both atomic and molecular dopant low-n Rydberg transitions in atomic and molecular perturbers, the results of which are presented in Chapters 4 and 5.

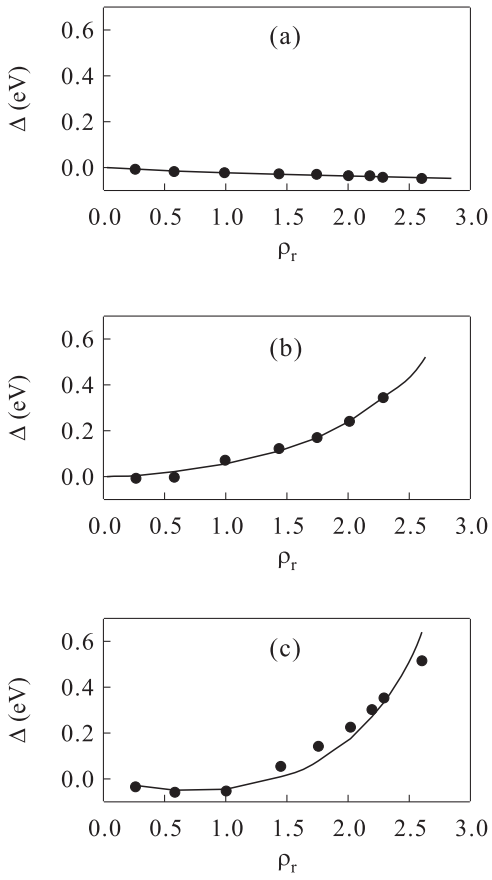

Figure 2.9: Experimental (•) and calculated (—) energy shift of the NO (a) the $B'^2\Delta \leftarrow X^2\Pi$ ($v' = 7,\ 0$) valence transition, (b) the $A^2\Sigma^+ \leftarrow X^2\Pi$ ($v' = 0,\ 0$) Rydberg transition and (c) the $C^2\Pi^+ \leftarrow X^2\Pi$ ($v' = 0,\ 0$) Rydberg transition plotted versus the reduced argon number density [54].

Chapter 3

Experiment and Modeling

3.1 Experimental apparatus

All of the photoabsorption measurements were obtained using the one-meter aluminum Seya-Namioka (Al-SEYA) beamline on bending magnet 8 of the Aladdin storage ring at the University of Wisconsin Synchrotron Radiation Center (SRC) in Stoughton, WI. This beamline, which was decommissioned during Winter 2007, produced monochromatic synchrotron radiation having a resolution of $\sim$ 8 meV in the energy range of 6 - 11 eV. Fig. 3.1 shows a schematic of our experimental endstation attached to the exit port of the Al-SEYA beamline. When the sapphire window is open, the monochromatic synchrotron radiation enters the vacuum chamber which is equipped with a sample cell (cf. Fig. 3.2). The photoabsorption signal is detected by a photomultiplier that is connected to the data collection computer via a Keithley 486 picoammeter. The pressure in the vacuum chamber is maintained at low 10^{-8} to high 10^{-9} Torr by a Perkin-Elmer ion pump. The experimental copper cell is equipped with entrance and exit MgF_2 windows (with an energy cut-off of 10.9 eV) that are capable of withstanding pressures of up to 100 bar and temperatures of up to 85°C. This cell, which has a path length of 1.0 cm, is connected to an open flow liquid

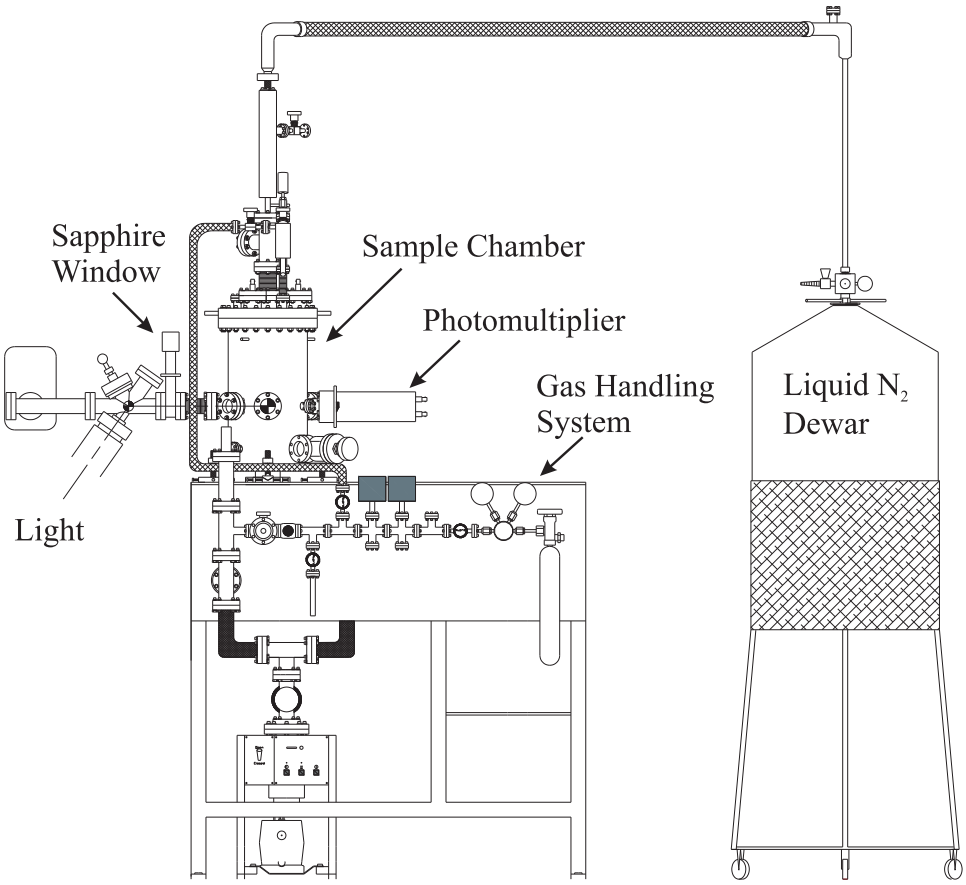

Figure 3.1: Schematic of the experimental endstation

nitrogen cryostat and resistive heater system allowing the temperature to be controlled to within ± 0.5°C with a Lakeshore 330 Autotuning Temperature controller. The gas sample is added through the gas handling system (GHS, cf. Fig. 3.3), which consists of 316-stainless steel components connected by copper gasket sealed flanges. The initial pressure for the GHS and sample cell is in the low 10^{-8} Torr range. A Pfeiffer-Balzers Turbo Molecular Pumping Station is used to remove gas from the GHS during sample preparation. This pumping station can maintain a pressure of low 10^{-7} Torr to high 10^{-8} Torr in the GHS during data acquisition.

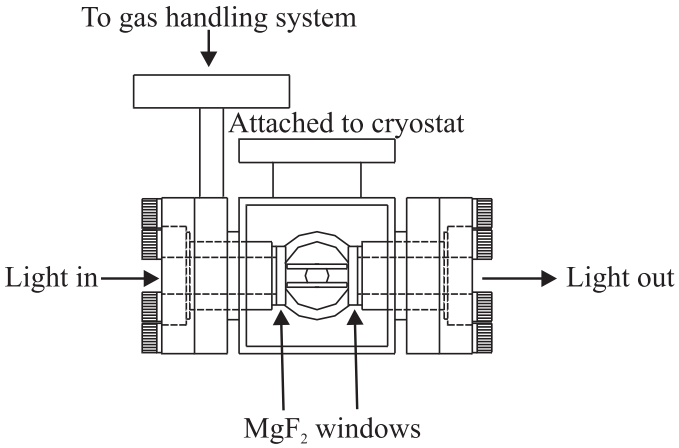

Figure 3.2: Schematic of the copper experimental cell.

3.2 Sample information and preparation

In this work, two dopants (i.e. methyl iodide and xenon) and five perturbers (i.e. argon, krypton, xenon, carbontetrafluoride and methane) were studied. All dopants and perturbers were used without further purification: methyl iodide (Aldrich, 99.45%), argon (Matheson Gas Products, 99.9999%), krypton (Matheson Gas Products, 99.998%), xenon(Matheson Gas Products, 99.995%), carbontetrafluoride (Matheson Gas Products, 99.999%) and methane (Matheson Gas Products, 99.999%). Photoabsorption spectra for each neat dopant and neat perturber were measured to verify the absence of impurities in the spectral range of interest.

The atomic perturber number densities were calculated from the Strobridge equation of state [78] with the parameters obtained from [79] for argon, [80] for krypton, and [81] for xenon. The equation of state for methane was a modified Benedict-Webb-Rubin equation of state [82] having parameters from [82]. For carbon tetrafluoride, the equation of state is the Benedict-Webb-Rubin equation of state [83] for $T \geq T_c$ and a Peng-Robinson equation of state [84] for $T < T_c$ with parameters from [85, 86].

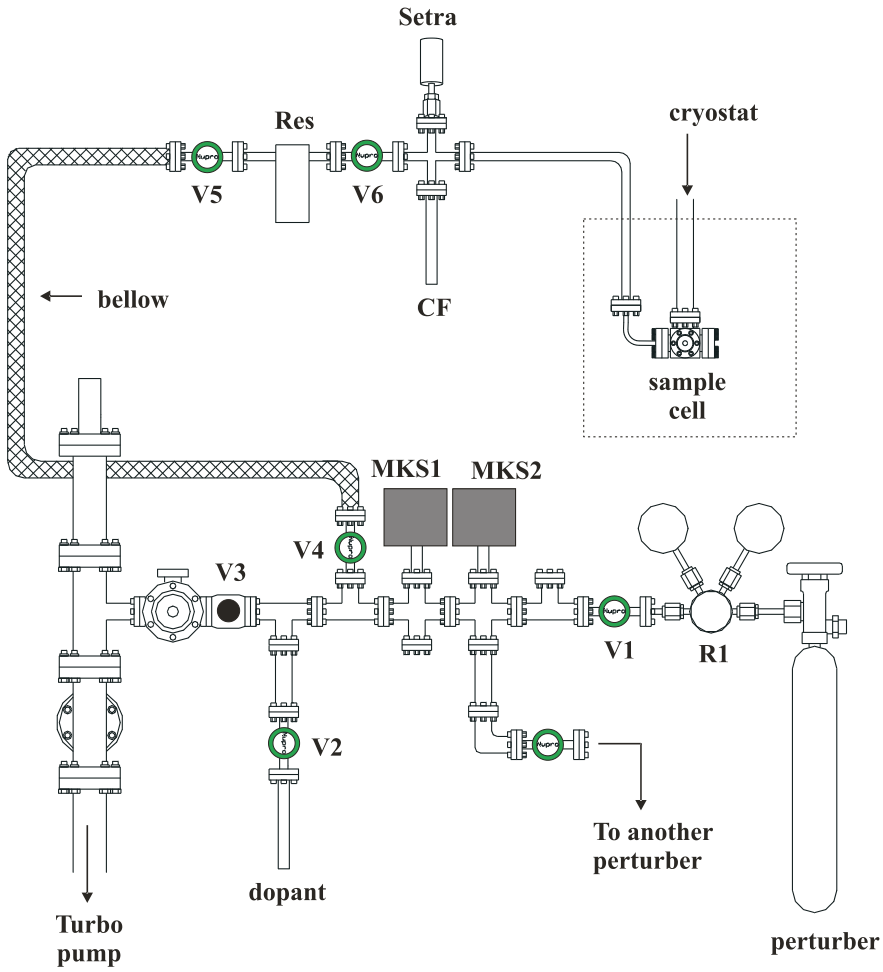

Figure 3.3: Schematic representation for a typical arrangement of the gas handling system. V1-V6: valves; R1: dual stage regulator; MKS1: pressure manometer (maximum range 10.000 mbar); MKS2: pressure manometer (maximum range 1.000 bar); Res: reservoir; Setra: pressure manometer (maximum range 200.00 bar); and CF: cold finger. For a gas phase dopant, such as xenon, the dopant cylinder is attached at the port provided for an additional perturber. Adapted from [77].

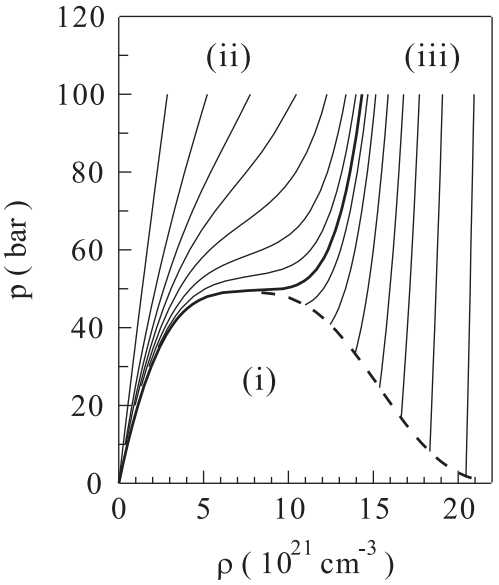

Figure 3.4: Phase diagram of Ar calculated from a Strobridge equation of state with coefficients from [78]. The thick solid line is the critical isotherm; the dashed line is the vapor pressure. Lines to the left of the critical isotherm represent $T > T_c$.

Fig. 3.4 shows a pressure-density-temperature graph for argon, which will be used here to exemplify our procedure for determining a series of samples to be investigated. The critical isotherm and vapor pressure line divide the phase diagram into three regions: (i) the two-phase liquid/gas region below the vapor pressure line, (ii) the single-phase supercritical region, and (iii) the single-phase dense gas region. The thick solid line is the critical isotherm; the dashed line is the vapor pressure. Lines to the left of the critical isotherm represent $T > T_c$. To obtain homogeneous samples for all seven systems investigated, our prepared samples are selected to be in regions (ii) and (iii). For temperatures above the critical temperature [i.e., samples in region (ii)], we are able to change the density by increasing the pressure on a single isotherm. Thus, for medium perturber densities we select two isotherms that are $2-10$°C apart and are at least 2°C (and preferably 5°C) above the critical temperature. Then, we slowly increase the perturber pressure, while maintaining a fixed temperature, in the

system to increase the perturber density. The isotherms are chosen so that the best overlap in densities is obtained. The first temperature below the critical temperature must also be at least 2°C below the critical temperature. Thus, to keep the density step size constant as we transition between region (ii) and region (iii), the latter of which has steeper slopes for the temperature isotherms, the isotherms above the critical temperature must be selected with care. The $2-5$°C temperature boundary around the critical temperature ensures that critical effects are not observed in the non-critical temperature data. The steepness of the isotherms in region (iii) prevents us from changing the density by changing the pressure. Thus, in this region we change the density by changing the temperature. The pressure is maintained at a minimum of 5 bar above the vapor pressure for each temperature in order to minimize the noise in the photoabsorption spectra due to increased cluster formation as the gas begins to form a liquid.

The quality of a data set was monitored by performing basic data analysis during measurements, and any anomalies were corrected by immediately re-measuring the photoabsorption spectrum for the problem density/temperature/pressure. Once a data set is obtained for non-critical temperatures, the photoabsorption data for perturber densities on an isotherm near the critical isotherm are then obtained. For these measurements we set the temperature to within +0.5°C of the critical temperature (chosen to prevent liquid formation in the cell during temperature stabilization near the critical density and to minimize critical opalescence during data acquisition). Near the critical density, the consistency of the density step is dependent on the slope of the critical isotherm. If the critical isotherm has a small slope in this

region, it becomes difficult to acquire samples at a constant density step size due to our inability to vary the perturber pressure practically by less than 0.01 bar and to the difficulties encountered in maintaining temperature stability. For instance, near the critical density of xenon, a 1 mbar change in pressure or a 0.001°C change in temperature causes a density change of 2.0×10^{21} cm^{-3}. Maintaining the necessary temperature stability (i.e., $\pm$ 0.2°C) during the acquisition of data along the critical isotherm is difficult with an open flow liquid nitrogen cryostat system and usually requires constant monitoring with manual adjustment of the nitrogen flow.

Our samples are prepared in the gas handling system (GHS) that is shown schematically in Fig. 3.3. During the initial bakeout, the whole GHS and the vacuum chamber are heated to 100°C under vacuum for several days to remove any water adsorbed onto the surface of the stainless steel. The initial bake is stopped when the base pressure of the GHS and sample chamber is in the low 10^{-7} or high 10^{-8} Torr range, so that upon cooling the final GHS base pressure is $10^{-8} - 10^{-9}$ Torr. Anytime a system is changed (either the dopant or the perturber), the GHS is again baked in order to return the system to near the starting base pressure. This prevents cross-contamination between dopant/perturber systems. When CH_3I in the dopant, prior to baking the CH_3I is degassed with three freeze/pump/thaw cycles. Once the initial bakeout is finished, the liquid nitrogen transfer line is installed in the system and the sample cell is aligned. Finally, since our chamber is used only during the summer, an empty cell spectrum is obtained to ensure the quality of the MgF_2 windows. This empty cell is also used to correct the experimental data (see below). Once the empty

cell is measured, we are ready to add a sample to the cell. For simplicity in what follows, we will describe the preparation of a CH_3I doped perturber.

The preparation of the sample begins by adding dopant to the sample cell. This is accomplished by closing valve V3 to stop pumping on the GHS, and valve V1 to protect the perturber regulator from the dopant since the dopant is usually difficult to pump back out of the system. Valve V2 is opened until the desired pressure of dopant (monitored using MKS1, which can measure pressures up to 10.000 mbar) has been added to the GHS. After dopant addition, V6 is closed to seal the sample cell and V3 is opened to pump the dopant out of the remainder of the GHS. Dopant is added as quickly as possible, since dopants tend to stick to the walls of the GHS and are difficult to pump out. The longer the dopant stays in the GHS, the longer one has to wait for the GHS to return to a base pressure of 10^{-7} Torr, which is necessary before the addition of the perturber. While the base pressure in the GHS is returning to 10^{-7} Torr, a reference spectrum of the dopant is measured as a check on the purity of the dopant.

The perturber is added by first verifying that valves V4 and V5 are open and that valve V1 is closed. Since most of the perturber cylinders are delivered with pressures of $600 - 2000$ psi ($40 - 130$ bar), it is important to ensure that the regulator (R1) is closed before the bottle is opened. Once R1 is open, high pressure exists in the GHS on the high pressure side of the regulator. To prevent accidents, the gas bottle never remains open during the addition of the perturber. Moreover, the regulator is set so that the low pressure side has a pressure of $15 - 30$ psi ($1 - 2$ bar) to ensure the safety of the thin walled flexible stainless steel bellows between V4 and V5. The perturber is

added by closing V3 and opening V1 until the desired pressure is reached, or 1 bar is added to the GHS. V6 is opened and then rapidly closed. This places approximately 900 mbar of the perturber in the cell if the pressure in the GHS is 1 bar. Any pressure over 1 bar is added by first collecting the sample (and 1 bar of perturber) into the cold finger using liquid nitrogen. (The small amount of perturber (i.e., 1 bar) is added before this collection to ensure that the dopant is not at the bottom of the cold finger. This allows for faster mixing of the dopant/perturber sample once the final pressure is reached.) The volume between V5 and V6 is approximately 3 times the volume in the sample cell and cold finger region when the sample cell is at room temperature, whereas the volume of the GHS between V1 and V6 is approximately 10 times that of the sample cell and cold finger region. Thus, the amount of perturber added to the gas handling system, and therefore which valves are closed before collecting the perturber into the cold finger, depends on the final pressure required in the sample cell. For instance, if 30 bar is the desired pressure, one can use 10 one-bar fills from the reservoir, or 3 one-bar fills using the entire GHS. Adding perturber gas to the cell using the entire GHS is usually faster if one is starting with higher pressures. However, this procedure is risky since V3 can slip open during the process of collecting the gas into the cold finger. Thus, V3 and the pumping speed of the vacuum pump (which drops dramatically if V3 slips) must be monitored during this procedure.

Once the desired perturber pressure is reached, the sample is mixed at the cold finger using three liquid nitrogen freeze/thaw cycles. Then the temperature of the sample cell is changed to the desired temperature (or the temperature is allowed to stabilize), and the photoabsorption spectrum is obtained. The next sample is

prepared by either adding additional perturber or by changing the temperature (or occasionally by adding dopant). Finally, we should note that the cold finger is always at room temperature (if the critical temperature of the perturber is below room temperature) and, therefore, that the sample cell itself represents a open thermodynamic system. Thus, time must be allowed after addition of a sample for the cell to stabilize at the desired temperature.

Occasionally, dopant must be added to the sample. The addition of dopant requires that two spectra be obtained at the same perturber number density in order to use Beer's law to calculate the new dopant concentration. Dopant is added by ensuring that the GHS is at a suitable base pressure. Then the necessary amount of dopant is added to the reservoir (on the assumption that the reservoir/sample cell ratio is 3:1). V5 is then closed and V6 is opened. The sample is mixed two times and then is collected back into the cold finger. V6 is then closed and the sample is mixed two more times. Since most of the gases in this study have low vapor pressures at liquid nitrogen temperature, all of the sample is collected into the cold finger and, therefore, the perturber density does not change. Care is taken to ensure that dopant does not need to be added during studies near the critical temperature and density of the perturber, where small pressure changes can lead to large density changes.

3.3 Data acquisition and analysis

The intensity of the synchrotron radiation exiting the monochromator is monitored by recording the beam current of the storage ring as well as the photoemission from a nickel mesh situated prior to the sample cell. The light then enters the experimental cell through a MgF_2 window, travels through the sample and then a second MgF_2

window before striking a thin layer of sodium salicylate powder on the inside of a glass window prior to the photomultiplier tube. The sodium salicylate powder has a large, flat quantum efficiency over most of the energy range of interest. An empty cell (acquired for a base pressure of 10^{-7} or 10^{-8} Torr) corrects the dopant absorption spectra for absorption by the windows and any fluctuations in the quantum efficiency of the sodium salicylate detector.

The basic data correction routine for a standard photoabsorption spectrum begins by dividing the spectrum by the current from the nickel mesh to correct for the exponential decay of the synchrotron radiation, and then by the empty cell absorption (which has also been corrected by a nickel mesh obtained during the acquisition of the empty cell). However, changes in the emittance of the synchrotron light source have increased the amount of second-order light from the Al-Seya monochromator. This second-order light, the intensity of which may change during the lifetime of one fill of the electron storage ring (approximately six hours), shows up in the nickel mesh but not in the sample absorption (i.e., the cell windows act as a bandpass filter). Thus, even after the empty cell correction, the baseline may not be flat in some cases. Therefore, the transmission spectra presented here are normalized to the incident light intensity by dividing first by the beam current saved during the data acquisition and then by the transmission of the empty cell (also corrected by the appropriate beam current). Once the spectrum is corrected by the empty cell, the spectrum is a transmittance spectrum. We then convert this spectrum to absorbance. An example of this type of data correction is shown in Fig. 3.5.

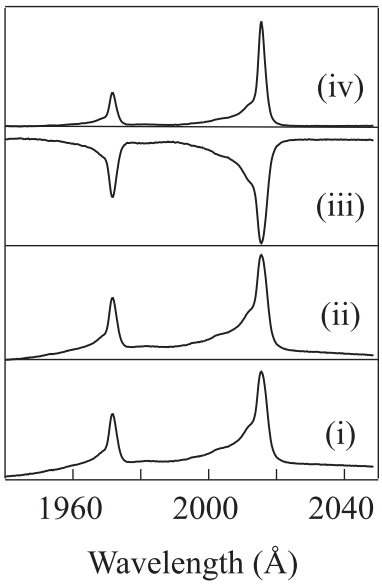

Figure 3.5: Data analysis routine. (i) is the raw photoabsorption data for CH_3I in low density Ar, (ii) is the absorption spectrum corrected by beam current, (iii) is the absorption spectrum corrected by the empty cell absorption to give a transmittance spectrum, (iv) is the transmittance spectrum converted to absorbance. All spectral absorbance are normalized to a relative scale so that they can be compared to line shape simulations. See discussion in text.

3.4 Line shape simulations

3.4.1 Line shape function

The experimental line shapes were simulated using the semi-classical statistical line shape function given in eq. (2.11). Rewriting eq. (2.11) in terms of the autocorrelation function allows eq. (2.11) to be given as a Fourier transform, namely [45,46,53,57]

$$\mathfrak{L}(\omega) \;=\; \frac{1}{2\,\pi}\,\mathrm{Re}\int_{-\infty}^{\infty} dt\;\mathrm{e}^{-i\,\omega\,t}\;\langle \mathrm{e}^{i\,\omega(\mathbf{R})\,t}\,\rangle\;, \tag{3.1}$$

where $\omega = \omega(\mathbf{R}) - \omega_0$, with ω_0 being the transition frequency for the neat dopant. Eq. (3.1) neglects lifetime broadening and assumes that the transition dipole moment is independent of $\mathbf{R}$. In the substitution of the exponential density expansion [i.e., eq. (2.12)] for the autocorrelation function, the general term A_n represents a (n+1)-body interaction [40]. However, since the strength of the interaction decreases as the number of bodies involved increases, and since the higher order interactions are more difficult to model, our line shape simulations are truncated at the second term $A_2(t)$, or three body interactions. Within this approximation, eq. (3.1) becomes

$$\mathfrak{L}(\omega) \;=\; \frac{1}{2\,\pi}\,\mathrm{Re}\int_{-\infty}^{\infty} dt\;\mathrm{e}^{-\,i\,\omega\,t}\;\exp\left[A_1(t)\;+\;A_2(t)\right] \quad , \tag{3.2}$$

where the two terms are recalled from eq. (2.15),

$$A_1(t) \;=\; 4\,\pi\,\rho_{\mathrm{P}}\int_0^{\infty} dr\;r^2\;g_{\mathrm{PD}}(r)\left[\;\mathrm{e}^{-\,i\,t\,\Delta V(r)}\;-\;1\;\right] \quad ,$$

and eq. (2.16),

$$A_2(t) \;=\; 4\,\pi\,\rho_{\rm P}^2 \int_0^\infty dr_1\; r_1^2\; g_{\rm PD}(r_1)\; \left[{\rm e}^{-\,i\,t\,\Delta V(r_1)} \;-\; 1\right] \times \int_0^\infty dr_2\; r_2^2\; g_{\rm PD}(r_2)\; \left[\; {\rm e}^{-\,i\,t\,\Delta V(r_2)} \;-\; 1\;\right] \times \frac{1}{r_1\; r_2} \int_{|r_1\,-\,r_2|}^{|r_1\,+\,r_2|} s\;\left[\; g_{\rm PP}(s) \;-\; 1\;\right] ds\;.$$

The required radial distribution functions (i.e., $g_{\rm PP}$ and $g_{\rm PD}$) were obtained from the analytical solution of the Ornstein-Zernike equation for a binary system within the Percus-Yevick (PY) closure [87], while the Fourier transform for eq. (3.2) was performed using a standard fast Fourier transform algorithm [88]. The line shape obtained from the transform for eq. (3.2) was convoluted with a standard Gaussian slit function to account for the finite resolution ($\sim$ 8 meV) of the monochromator. More detailed discussions are given below.

3.4.2 Fast Fourier transform

A Fourier transform has a general form [88]

$$F(\omega) = \frac{1}{2\,\pi} \int_{-\infty}^{\infty} f(t)\; {\rm e}^{-\,i\,\omega\,t}\; dt\;. \tag{3.3}$$

Since the line shape function is calculated numerically, the integration limits for (3.3) must be finite and, therefore, an appropriate integration range must be determined. For any Fourier transformation, the integration limit and the total number of steps are related through [88]

$$\delta t \;\times\; \delta\omega \;=\; \frac{2\,\pi}{N}\;, \tag{3.4}$$

where δ stands for the sampling interval (i.e., step size) of the corresponding variable and N is the total number of discrete points. Fourier transforms rely on the fact

that data are usually obtained in discrete steps and the generating functions $f(t)$ and $F(\omega)$ can be represented by the set of points

$$\begin{aligned} f_k \;&\equiv\; f(t_k)\,, \quad t_k \;=\; k\,\delta t\,, \quad k \;=\; 1, \ldots, N\,, \\ F_n \;&\equiv\; F(\omega_n)\,, \quad \omega_n \;=\; n\,\delta\omega\,, \quad n \;=\; -\,\frac{N}{2}, \ldots, \frac{N}{2} \;-\; 1\,. \end{aligned} \tag{3.5}$$

Therefore, the function $F(\omega)$ is determined point-wise using

$$\begin{aligned} F(\omega_n) \;&=\; \frac{1}{2\,\pi}\int_{-\infty}^{\infty} f(t)\,\mathrm{e}^{-\,i\,\omega_n\,t}\;dt \;=\; \frac{1}{2\,\pi}\;\sum_{k=1}^{N}\; f_k\;\mathrm{e}^{-\,i\,\omega_n\,t_k}\;\delta t \\ &=\; \frac{\delta t}{2\,\pi}\;\sum_{k=1}^{N}\; f_k\;\mathrm{e}^{-\,i\,2\,\pi\,n\,k/N}\;. \end{aligned} \tag{3.6}$$

For simplicity, we will define the discrete Fourier transform from time to angular frequency as eq. (3.6). When computing the Fourier transform from eq. (3.6), the quickest method is known as a fast Fourier transform (FFT) and requires that the number of steps N be a power of 2. In our calculations, we use a Cooley-Tukey FFT algorithm [88] with $N = 1024$. The requirements for calculating eq. (3.3) within this FFT algorithm are, therefore, a complex array of the calculated values of the time dependent autocorrelation function truncated to the second term.

Rewriting eq. (3.2) using Euler's relation gives [58]

$$\langle \mathrm{e}^{i\,\omega(\mathbf{R})\,t}\,\rangle \;=\; \mathrm{Re}\,\langle \mathrm{e}^{i\,\omega(\mathbf{R})\,t}\,\rangle \;+\; \mathrm{Im}\,\langle \mathrm{e}^{i\,\omega(\mathbf{R})\,t}\,\rangle\;, \tag{3.7}$$

where the real and the imaginary parts are given by

$$\begin{aligned} \mathrm{Re}\,\langle e^{i\,\omega(\mathbf{R})\,t}\rangle \;&=\; \exp\left[\mathrm{Re}\,(A_1(t) \;+\; A_2(t)\,)\,\right]\,\cos\left[\mathrm{Im}\,(A_1(t) \;+\; A_2(t)\,)\,\right]\;, \\ \mathrm{Im}\,\langle e^{i\,\omega(\mathbf{R})\,t}\rangle \;&=\; \exp\left[\mathrm{Re}\,(A_1(t) \;+\; A_2(t)\,)\,\right]\,\sin\left[\mathrm{Im}\,(A_1(t) \;+\; A_2(t)\,)\,\right]\;. \end{aligned} \tag{3.8}$$

In eq. (3.8),

$$\begin{aligned}
&\mathrm{Re}[A_1(t) \,+\, A_2(t)\,] \\
&\quad = \, 4\,\pi\,\rho_{\mathrm{P}} \int_0^\infty dr\; r^2\; g_{\mathrm{PD}}(r)\; [\cos(\Delta V(r)\,t) \,-\, 1\,] \\
&\quad + \, 4\,\pi\,\rho_{\mathrm{P}}^2 \int_0^\infty \int_0^\infty dr_1\; dr_2\; h(r_1, r_2)\; [\cos(\Delta V(r_1)\,t)\; \cos(\Delta V(r_2)\,t) \\
&\qquad\qquad + \, 1 \,-\, \sin(\Delta V(r_1)\,t)\; \sin(\Delta V(r_2)\,t) \\
&\qquad\qquad - \, \cos(\Delta V(r_1)\,t) \,-\, \cos(\Delta V(r_2)\,t)\,] \;,
\end{aligned} \tag{3.9}$$

and

$$\begin{aligned}
&\mathrm{Im}[A_1(t) \,+\, A_2(t)\,] \\
&\quad = \, -\, 4\,\pi\,\rho_{\mathrm{P}} \int_0^\infty dr\; r^2\; g_{\mathrm{PD}}(r)\; [\sin(\Delta V(r)\,t)\,] \\
&\quad - \, 4\,\pi\,\rho_{\mathrm{P}}^2 \int_0^\infty \int_0^\infty dr_1\; dr_2\; h(r_1, r_2)\; [\sin(\Delta V(r_1)\,t)\; \cos(\Delta V(r_2)\,t) \\
&\qquad\qquad + \, \cos(\Delta V(r_1)\,t)\; \sin(\Delta V(r_2)\,t) \\
&\qquad\qquad - \, \sin(\Delta V(r_1)\,t) \,-\, \sin(\Delta V(r_2)\,t)\,] \;,
\end{aligned} \tag{3.10}$$

with

$$h(r_1, r_2) \;=\; r_1\; g_{\mathrm{PD}}(r_1)\; r_2\; g_{\mathrm{PD}}(r_2) \int_{|r_1 - r_2|}^{|r_1 + r_2|} s\,[g_{\mathrm{PP}}(s) \,-\, 1\,]\; ds \;.$$

The output of the FFT is a complex function of frequency. The real portion of this complex function is obtained and then convoluted with a standard Gaussian slit function. The final output is the simulated line shape function. Since eqs. (3.2), (3.9) and (3.10) depend on both the radial distribution functions and the ground-state and excited-state intermolecular potentials, we will discuss these below.

3.4.3 Radial distribution function

After significant investigation, our group determined that the most stable calculation technique for obtaining the radial distribution functions was the analytical solution of

the Ornstein-Zernike relation within the Percus-Yevick (PY) closure [87]. Although this solution for a binary system yields four coupled integro-differential equations, dilute solutions (i.e., $\rho_{\rm D} \ll \rho_{\rm P}$) allows these equations to be reduced to the calculation of the perturber/dopant radial distribution function $g_{\rm PD}(r)$ and the perturber/perturber radial distribution function $g_{\rm PP}(r)$. This analytical solution is given by [32, 87]

$$\begin{aligned} g_{\rm PD}(r) &= r^{-1}\, {\rm e}^{-\beta\, V_{\rm g}(r)}\, Y_{\rm PD}(r) \\ g_{\rm PP}(r) &= r^{-1}\, {\rm e}^{-\beta\, V'_{\rm g}(r)}\, Y_{\rm PP}(r)\ , \end{aligned} \tag{3.11}$$

where

$$\begin{aligned} Y_{\rm PD}(r) &= \int_0^r dt\ \frac{dY_{\rm PD}(t)}{dt}\ , \\ Y_{\rm PP}(r) &= \int_0^r dt\ \frac{dY_{\rm PP}(t)}{dt}\ , \end{aligned} \tag{3.12}$$

with

$$\begin{aligned} \frac{d}{dr}Y_{\rm PD}(r) &= 1 + 2\,\pi\,\rho_{\rm P}\int_0^\infty dt\ \left({\rm e}^{-\beta\, V_{\rm g}(t)} - 1\right)\, Y_{\rm PD}(t) \\ &\quad \times \Big[{\rm e}^{-\beta\, V'_{\rm g}(r+t)}\, Y_{\rm PP}(r+t) \\ &\quad - \frac{r-t}{|r-t|}\, {\rm e}^{-\beta\, V'_{\rm g}(|r-t|)}\, Y_{\rm PP}(|r-t|) - 2\,t\Big]\ , \\ \frac{d}{dr}Y_{\rm PP}(r) &= 1 + 2\,\pi\,\rho_{\rm P}\int_0^\infty dt\ \left({\rm e}^{-\beta\, V'_{\rm g}(t)} - 1\right)\, Y_{\rm PP}(t) \\ &\quad \times \Big[{\rm e}^{-\beta\, V'_{\rm g}(r+t)}\, Y_{\rm PP}(r+t) \\ &\quad - \frac{r-t}{|r-t|}\, {\rm e}^{-\beta\, V'_{\rm g}(|r-t|)}\, Y_{\rm PP}(|r-t|) - 2\,t\Big]\ , \end{aligned} \tag{3.13}$$

and with $V_{\rm g}$ and $V'_{\rm g}$ being the ground state perturber/dopant and ground state perturber/perturber intermolecular potentials.

3.4.4 Intermolecular potentials

Eqs. (3.2), (3.7) - (3.13) are explicitly dependent on the excited-state and ground-state perturber/dopant intermolecular potentials through $\Delta V(r)$, and are implicitly dependent on the perturber/perturber and perturber/dopant ground-state intermolecular potential via $g_{\rm PP}(r)$ and $g_{\rm PD}(r)$. Thus, these simulations require one to develop a single set of ground-state and excited-state intermolecular potential parameters for each system. A standard Lennard-Jones 6-12 potential, or

$$V(r) \;=\; 4\,\varepsilon \left[\left(\frac{\sigma}{r} \right)^{12} \;-\; \left(\frac{\sigma}{r} \right)^{6} \right] , \tag{3.14}$$

was chosen for the atomic perturber/perturber ground-state intermolecular interactions, and non-polar dopant/perturber ground-state intermolecular interactions. The ground-state molecular perturber/perturber intermolecular potential was a two-Yukawa potential, or

$$V(r) \;=\; -\,\frac{\kappa_0\,\varepsilon}{r} \left[\mathrm{e}^{-\,z_1\,(r\,-\,\sigma)} \;-\; \mathrm{e}^{-\,z_2\,(r\,-\,\sigma)} \right] . \tag{3.15}$$

The ground-state polar dopant/perturber intermolecular interactions were modeled using a modified Stockmeyer potential

$$V(r) \;=\; 4\,\varepsilon' \left[\left(\frac{\sigma'}{r} \right)^{12} \;-\; \left(\frac{\sigma'}{r} \right)^{6} \right] \;-\; \frac{1}{r^6} \alpha_P {\mu_D}^2 , \tag{3.16}$$

which can be rewritten in standard Lennard-Jones 6-12 potential form [32], with

$$\varepsilon \;=\; \varepsilon' \left[1 \,+\, \frac{\alpha_P\,{\mu_D}^2}{4\,\varepsilon'\,\sigma'^6} \right]^2 \quad , \qquad \sigma \;=\; \sigma' \left[1 \,+\, \frac{\alpha_P\,{\mu_D}^2}{4\,\varepsilon'\,\sigma'^6} \right]^{-1/6} \quad .$$

The modified Stockmeyer potential includes orientational effects via an angle average that presumes the free rotation of the polar dopant molecule. An exponential-6

potential, given by

$$V(r) \;=\; \frac{\varepsilon}{1-(6/\gamma)}\left\{\frac{6}{\gamma}\,e^{\gamma(1-\chi)}-\chi^{-6}\right\}\,, \tag{3.17}$$

was chosen for the excited-state dopant/ground-state perturber interactions. In eqs. (3.14) - (3.17), ε is the well depth, σ is the collision parameter, α_P is the perturber polarizability, μ_D is dopant dipole moment, $\chi \equiv r/r_e$ (where r_e is the equilibrium distance), and γ is the potential steepness.

The Lennard-Jones parameters for the atomic fluids and the modified Stockmeyer parameters for the CH_3I/Ar and CH_3I/Kr interactions were identical to the parameters used to model accurately the perturber-induced shift of the dopant ionization energy for methyl iodide in argon [32–34, 89], krypton [32, 35, 89] and xenon [36, 89]. The parameters κ_0, z_1, z_2, ε and σ in eq. (3.15) are adjusted to give the best fit to the phase diagram of the perturber [89]. The parameters ε, σ, χ and γ in eq. (3.17) are adjusted by hand to give the "best" fit to the experimental absorption spectra of the dopant low-n Rydberg states in each of the fluids investigated here.

Chapter 4

Atomic perturbers

4.1 Xe low-n Rydberg states in Ar

4.1.1 Xe absorption

The Xe $6s$ and $6s'$ Rydberg states (where s and s' denote the $J = 3/2$ and $J = 1/2$ angular momentum core state, repsectively) were experimentally measured in dense argon. As is discussed in Section 2.4.1, when Xe interacts with Ar, ground and excited state dimers form. These dimers are evidenced by blue satellite bands that arise on the higher energy side of the primary Rydberg transition. The Xe $6s$ Rydberg transition has two such blue satellite bands corresponding to eqs. (2.25)-(2.26), whereas the Xe $6s'$ Rydberg transition has a single blue satellite band corresponding to eq. (2.25) (cf. Fig. 2.5) [42–44]. The absence of the ground state XeAr dimer to XeAr eximer transition [i.e., eq. (2.26)] for the Xe $6s'$ Rydberg state may be caused by an extremely short lifetime preventing our ability to detect the transition or by the XeAr eximer decomposing during the excitation.

Figs. 4.1 and 4.2 present selected experimental Xe $6s$ and $6s'$ Rydberg transitions doped into supercrtical argon at non-critical temperatures and along an isotherm near the critical isotherm offset by the argon number density. It can be clearly seen that the Rydberg transitions broaden as a function of the argon number density. The

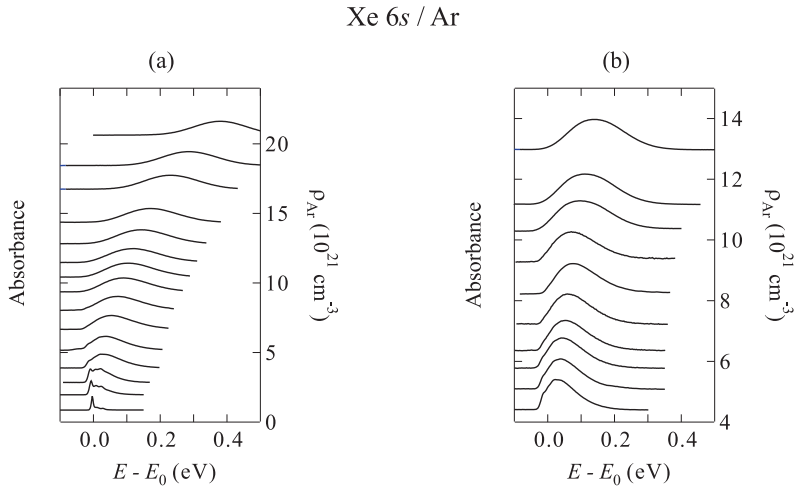

Figure 4.1: Selected absorption spectra for the Xe $6s$ Rydberg transition at (a) non-critical temperatures and (b) on an isotherm (i.e., $-121.8°$C) near the critical isotherm. The data are offset vertically by the argon number density ρ_{Ar}. The transition energy is $E_0 = 8.424$ eV for the unperturbed Xe $6s$ Rydberg transition. While all spectra have been normalized to 1 for future comparison with simulated line shapes, the integrated intensity is independent of argon number density.

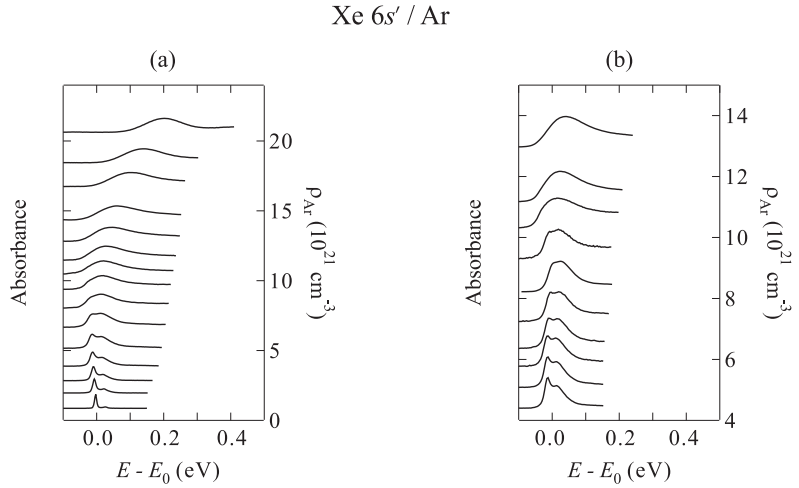

Figure 4.2: Selected absorption spectra for the Xe $6s'$ Rydberg transition at (a) non-critical temperatures and (b) on an isotherm (i.e., $-121.8°$C) near the critical isotherm. The data are offset vertically by the argon number density ρ_{Ar}. The transition energy is $E_0 = 9.557$ eV for the unperturbed Xe $6s'$ Rydberg transition. While all spectra have been normalized to 1 for future comparison with simulated line shapes, the integrated intensity is independent of argon number density.

maximum of the absorption band also shifts first slightly to the red and then strongly to the blue, similar to the original observations of Messing, *et al.* [45, 46]. Since the ground state interaction between Xe and Ar (or XeAr and Ar) is attractive, the ground states are stabilized by the argon solvent shell. The slight red shift observed at low argon number densities indicates that the xenon excited states (either Xe* or Xe*Ar) are also stabilized by the argon solvent shell. As the density increases, however, argon begins to shield the optical electron from the xenon cationic core, thereby decreasing the binding energy of the optical electron (cf. Fig. 2.4 as a visualization aid). Thus, as the density of argon increases the energy of the excited state also increases, leading to a blue shift in the transition energy at higher densities. Comparing Fig. 4.1a and 4.2a, the overall blue shift of the $6s$ Rydberg transition band is much larger than that of the $6s'$ band at the triple point liquid density of argon. This difference in overall shift is caused by the difference in the core state of the cation, since the $J = 1/2$ core state has a permanent quadrupole moment. This permanent quadrupole moment increases the interaction of the cationic core and the optical electron, thereby implying that the optical electron is less perturbed by the argon solvent shell.

However, since the blue satellite bands also broaden and shift with increasing argon density, the primary Xe transition becomes indistinguishable at medium to large argon number densities. Thus, the argon-induced energy shift of the primary Xe transition cannot be investigated directly using these data. Therefore, to probe perturber critical effects on the dopant excited states, we must first accurately simulate the absorption spectra over the entire argon density range at non-critical temperatures and on an isotherm near the critical isotherm.

Table 4.1: Intermolecular potential parameters for eqs. (3.14) and (3.16) used to simulate the Xe $6s$ and $6s'$ line shapes in Ar.

	$\varepsilon/k_{\mathrm{B}}$ (K)	r_e (Å)	γ
Ar/Ar[a]	119.5	3.826[b]	–
Xe/Ar	200.0	4.265[b]	–
XeAr/Ar	195.0	4.310[b]	–
Xe $6s$/Ar	300.0	5.20	16
Xe $6s'$/Ar	400.0	4.98	16
Xe($6s$)Ar/Ar	250.0	5.25	16

[a]Parameters obtained from Ref. [32].
[b]For a Lennard-Jones 6-12 potential [i.e., eq. (3.14)], $\sigma = 2^{-1/6} r_e$.

4.1.2 Line shape simulations

In order to simulate accurately the absorption spectra at high density, any line shape simulation has to include the primary transition, denoted a in Fig. 2.5 and given by eq. (2.24), as well as the two XeAr dimer transitions that yield the blue satellite bands, denoted b and c in Fig. 2.5 and given by eqs. (2.25) and (2.26), respectively. For the simulation of Xe in Ar, we chose to use eq. (3.14) for the ground state Ar/Ar, Xe/Ar, and XeAr/Ar interactions and eq. (3.17) for the Xe*/Ar and Xe*Ar/Ar interactions. We also required that the simulation use a single set of intermolecular potential parameters for the entire argon density range at non-critical temperatures and along the critical isotherm. All intermolecular potential parameters except the Ar/Ar ground state parameters were adjusted by hand to give the best simulated line shape in comparison to the experimental data. The values of these parameters are given in Table 4.1 [57].

The relative intensities of the simulated bands were set by comparison to the absorption spectra of Xe doped into argon at argon number densities where all bands could be clearly identified. Experimentally, at low argon number densities, the ratio

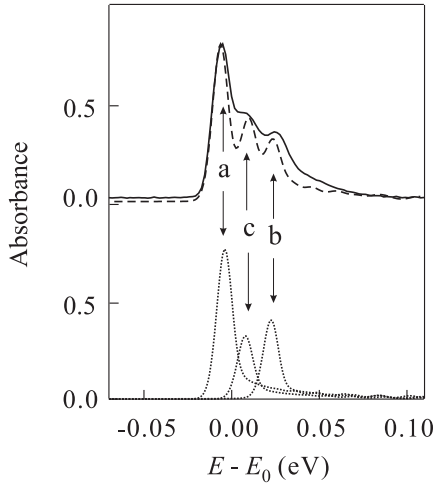

Figure 4.3: Photoabsorption spectrum (solid line, relative units) of the Xe $6s$ transition doped into Ar at an argon number density of $\rho_{\mathrm{Ar}} = 1.47 \times 10^{21}$ cm^{-3} and a temperature of 23.6°C. a corresponds to eq. (2.24), b to eq. (2.25), and c to eq. (2.26). The dashed line is the complete simulation, while the dotted lines represent the individual simulation using eq. (3.2) with the intermolecular potential parameters given in Table 4.1. For the primary transition a, $E_0 = 8.437$ eV. For the bands b and c, $E_0 = 8.4345$ eV and 8.432 eV, respectively.

of heights between the b band and the primary transition is 0.2 for both the Xe $6s$ and $6s'$ Rydberg states in Ar. For the Xe $6s$ Rydberg state in Ar, the ratio of heights between the c band and the primary transition is 0.45. Although for concentrated Xe systems, the ratio of heights for the blue satellite bands to the primary transition would increase with decreasing temperature or increasing perturber number density, this is not the case for the very dilute Xe/Ar system investigated here (i.e., [Xe] $<$ 10 ppm for all argon number densities). Therefore, we can assume that the intensity ratio of the blue satellite bands to the primary transitions stays constant at different temperatures and different argon densities. An example of a complete simulation is shown in Fig. 4.3.

Figs. 4.4a and 4.4b show a comparison between the simulated line shapes (dotted lines) and the experimental absorption spectra (solid lines) for the Xe $6s$ transition

at non-critical temperatures (cf. Fig. 4.4a) and on an isotherm (−121.8°C) near the critical isotherm (cf. Fig. 4.4b). A similar graph for the Xe $6s'$ transition is shown in Fig. 4.5. Clearly, the simulated spectra closely match the experimental spectra for all densities. Both the simulated and experimental line shapes show a slight red shift at low argon number densities, followed by a strong blue shift at high argon number densities. With these accurate line shape simulations, moment analyses can be performed on the primary transition in order to investigate perturber critical point effects, as well as to discuss trends in solvation of different dopant electronic transitions in the same simple atomic fluid.

4.1.3 Discussion

A line shape analysis was performed on the accurate simulations of the primary Xe $6s$ and $6s'$ Rydberg transitions in order to determine the average argon induced shift $\Delta(\rho_{\mathrm{Ar}})$ of the primary transition, as approximated from the first moment [i.e., eq. (2.22)]. This moment analysis is shown in Fig 4.6 as a function of reduced argon number density ρ_r, where $\rho_r = \rho_{\mathrm{Ar}}/\rho_c$ with $\rho_c \equiv 8.076 \times 10^{21}$ cm^{-3} [79]. Fig 4.6b shows an enhanced view of the perturber critical region with a critical effect in $\Delta(\rho_{\mathrm{Ar}})$ clearly apparent. The absence of the red shift observed by Messing, *et al.* [45, 46] (cf. Fig. 2.6) results from our performance of a moment analysis on a blue degraded band, instead of a direct non-linear least square analysis using a Gaussian fit function on the primary transition. In other words, while the peak of the primary transition red shifts slightly at low argon densities, the first moment of the band does not, due to the perturber induced broadening.

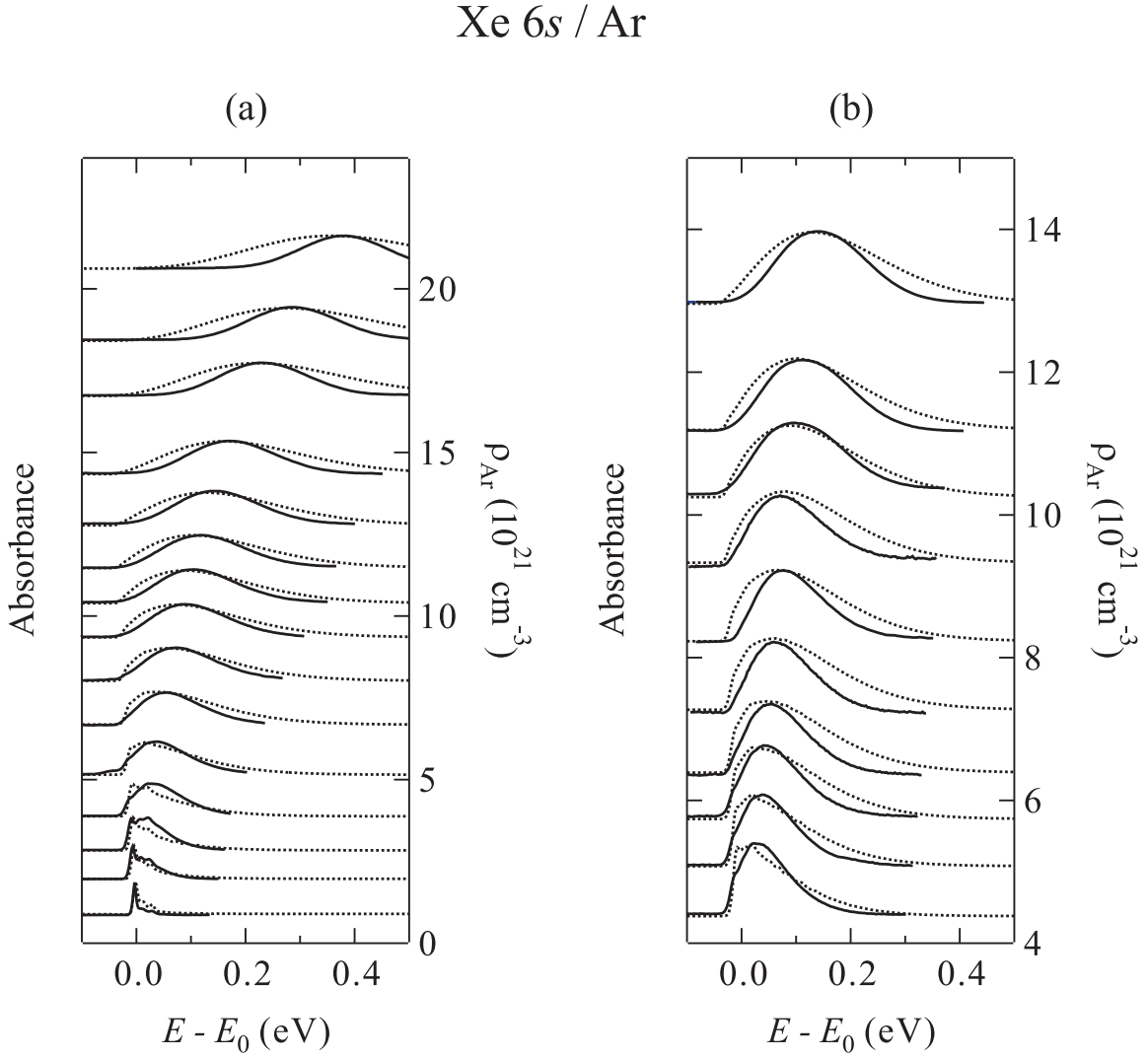

Figure 4.4: Selected photoabsorption spectra (–, relative scale) and simulated line shapes ($\cdots$) for the Xe 6s Rydberg transitions at (a) non-critical temperatures and (b) on an isotherm (i.e., -121.8°C) near the critical isotherm. The data are offset vertically by the argon number density ρ_{Ar}. The transition energy is $E_0 = 8.424$ eV for the unperturbed Xe 6s Rydberg transition.

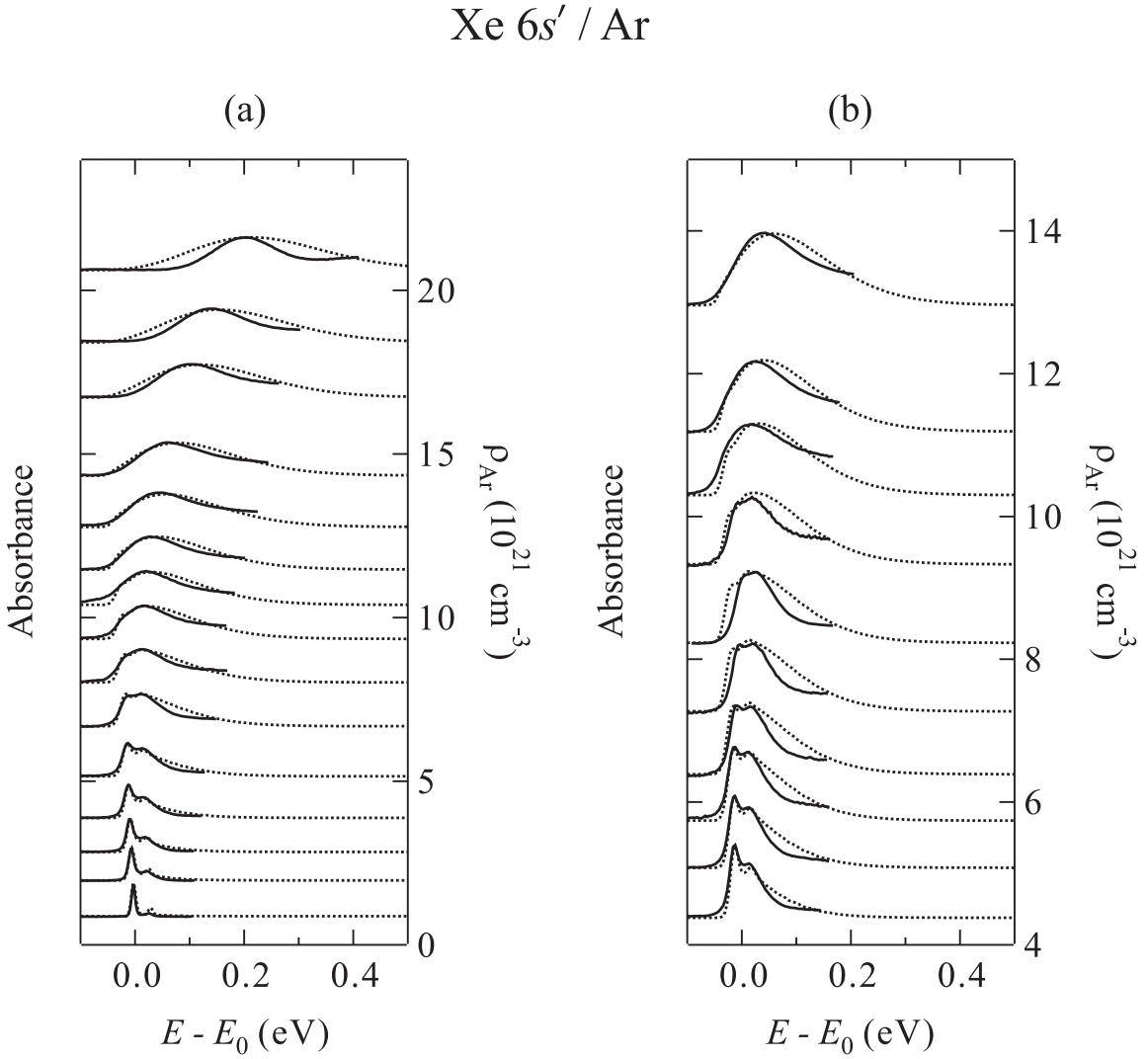

Figure 4.5: Selected photoabsorption spectra (–, relative scale) and simulated line shape ($\cdots$) for the Xe $6s'$ Rydberg transitions at (a) non-critical temperatures and (b) on an isotherm (i.e., $-121.8°$C) near the critical isotherm. The data are offset vertically by the argon number density ρ_{Ar}. The transition energy is $E_0 = 9.557$ eV for the unperturbed Xe $6s'$ Rydberg transition.

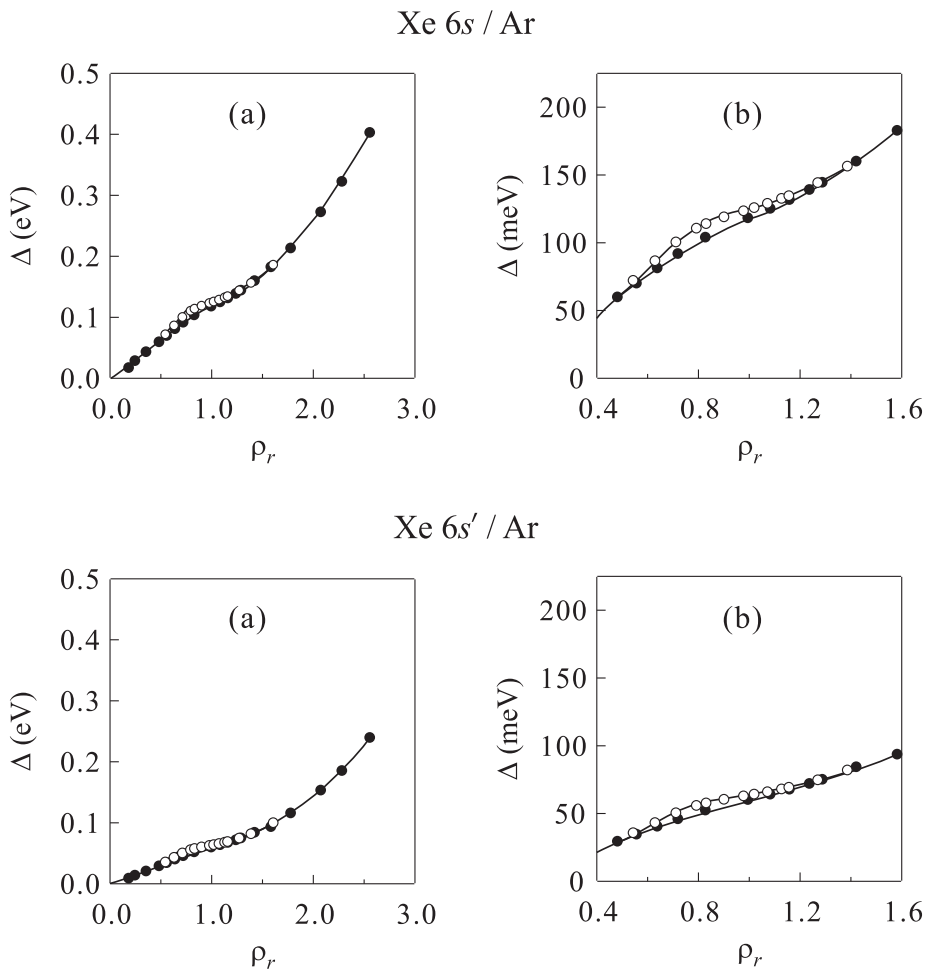

Figure 4.6: (a) The argon induced shift $\Delta(\rho_{\mathrm{Ar}})$, as approximated by eq. (2.22), of the primary transition for the Xe $6s$ and $6s'$ Rydberg states as a function of argon number density ρ_{Ar} at (•) non-critical temperatures and (○) along an isotherm near the critical isotherm. (b) An expanded view of $\Delta(\rho_{\mathrm{Ar}})$The solid lines are a visual aid. See text for discussion.

General trends emerged in the behavior of the simulated line shape as a function of the intermolecular potential parameters. For instance, we observed that the strength of the asymmetric blue broadening of a band increases with increasing $\Delta r_e \equiv r_e^{(g)} - r_e^{(e)}$ [where $r_e^{(i)}$ is the equilibrium dopant/perturber distance for either the ground state dopant ($i = g$) or the excited state dopant ($i = e$)]. However, the overall perturber-induced energy shift of the band depended on the ground state intermolecular po-

tential well depth $\varepsilon^{(g)}$ as well as Δr_e. The slight red shift at low perturber number densities, however, was controlled by the excited state intermolecular potential well depth $\varepsilon^{(e)}$. Comparison of Figs.4.4a and 4.5a shows that the $6s$ Rydberg state broadens and shifts to higher energies more quickly than does the $6s'$ state. Since both transitions are excited from the same ground state (implying that the ground state intermolecular potential parameters remain unchanged), Δr_e must decrease and $\varepsilon^{(e)}$ increase in order to simulate the Xe $6s'$ Rydberg state in argon correctly. These general trends proved helpful when determining the intermolecular potential parameters for new systems.

Messing, *et al.* [45, 46] concluded that the argon induced energy shift is density dependent and temperature independent. However, both our experimental absorption spectra and the line shape simulations show a distinct temperature dependence near the argon critical point. To test the sensitivity of the perturber critical point effect, we extracted the perturber dependent shift $\Delta(\rho_{Ar})$ of the simulated primary Xe $6s$ transition in supercritical argon near the critical density along three different isotherms (i.e., $T_r = 1.01$, 1.06 and 1.11, where $T_r = T/T_c$ with $T_c = -122.3°\mathrm{C}$). These data are shown in Fig. 4.7a and clearly show that the critical effect is extremely sensitive to temperature and can be easily missed if the temperature of the system is not maintained close to the critical isotherm. If we return to the line shape equation [i.e., eq. (3.2)], we observe that the two-body interaction term $A_1(t)$ and the three-body interaction term $A_2(t)$ depend on the difference between the excited state and ground state intermolecular potentials and on the perturber/dopant radial distribution function. Since the potential difference will not depend dramatically

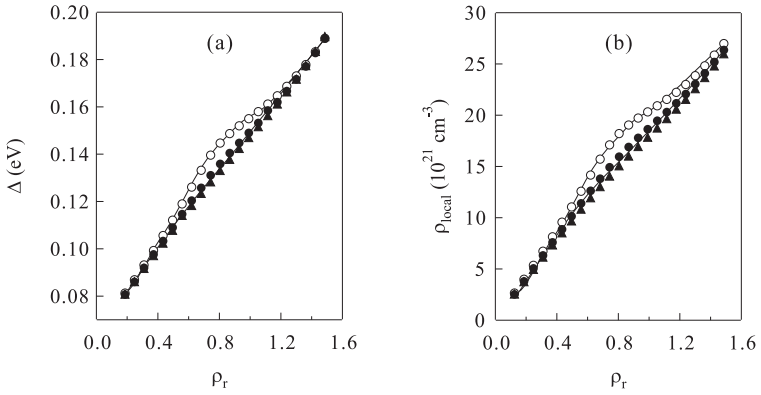

Figure 4.7: (a) The calculated argon induced shift $\Delta(\rho_{Ar})$ doped into supercritical argon plotted as a function of reduced argon number density at a reduced temperature $T_r = 1.01$ (○), 1.06 (●) and 1.11 (▲). (b) The local densities ($\rho_{\rm local} = g_{\rm max}\,\rho_{\rm bulk}$) of the first argon solvent shell around a central Xe atom plotted as a function of reduced argon number density at a reduced temperature $T_r \simeq 1.01$ (○), 1.06 (●) and 1.11 (▲). The solid lines are provided as visual aid.

on temperature, the critical point effect must be dominated by changes in the perturber/dopant radial distribution function $g_{\rm PD}(r)$. In Fig. 4.7b, we plot the local density of the first solvent shell as a function of the bulk reduced argon number density on the same three isotherms. The $T_r = 1.01$ isotherm shows a much larger density deviation near the critical density in comparison to the other two isotherms. Thus, the argon induced blue shift is caused by the first perturber shell shielding the cationic core from the optical election. This increase in shielding decreases the binding energy of the electron, thereby increasing the excitation energy.

4.2 CH_3I low-n Rydberg states in Ar, Kr and Xe

4.2.1 CH_3I absorption

The CH_3I $6s$ and $6s'$ Rydberg states doped into supercritical argon, krypton and xenon were investigated both experimentally and theoretically [58] from low perturber number density to the density of the triple point liquid, at both non-critical

temperatures and on an isotherm near (i.e., +0.5°C) the critical isotherm of the perturber. The CH_3I $6s$ and $6s'$ Rydberg states show perturber-induced energy shifts and broadening similar to that observed for the Xe low-n Rydberg states in supercritical argon. The peak positions of the absorption spectra shift to the red slightly and then strongly to the blue as a function of perturber number densities. This is similar to the behavior for CH_3I in dense rare gases observed by Messing, *et al.* [47,48]. Unlike Xe, which forms heterogenous dimers in argon, the CH_3I/perturber interactions are weaker. Thus, CH_3I does not possess blue satellite bands caused by dimer or excimer formation. However, CH_3I does possess a strong vibrational transition on the blue side of the adiabatic transition. Fig. 2.7 shows the absorption of both the $6s$ and $6s'$ Rydberg states of CH_3I and clearly illustrates the vibrational state, which represents the CH_3 group deformation vibrational band ν_2. Figs. 4.8 - 4.10 present selected photoabsorption spectra for the CH_3I $6s$ Rydberg transition doped into supercrtical argon, krypton and xenon, while similar graphs for the CH_3I $6s'$ transition are shown in Figs. 4.11 - 4.13. Experimental spectra of CH_3I in Xe at number densities between 5.0×10^{21} cm^{-3} and 7.0×10^{21} cm^{-3} could not be obtained, because of the large density deviation induced by small temperature fluctuations ($\approx 2.0 \times 10^{21}$ cm^{-3} for a 0.001°C temperature change) in this density region.

The experimental absorption of CH_3I low-n Rydberg transitions show that as the perturber number density increases, the ν_2 vibrational band broadens and shifts until it merges with the adiabatic transition. Therefore, determining the perturber induced shift $\Delta(\rho_P)$ of the adiabatic transition from a simple moment analysis of the spectra presented in Figs. 4.8 - 4.13 is not possible, and we must perform an

accurate line shape analysis of these data in order to extract $\Delta(\rho_{\rm P})$ and investigate the perturber critical effect. However, some qualitative information can be gleaned from Figs. 4.8 - 4.13. First, the rate of the broadening and the rate of shift for both the adiabatic transition band and the ν_2 vibrational transition band differ dramatically for different perturbers. However, the CH_3I $6s$ and $6s'$ transitions have almost the same perturber induced shift, which differs from the behavior observed for the Xe in Ar system previously presented.

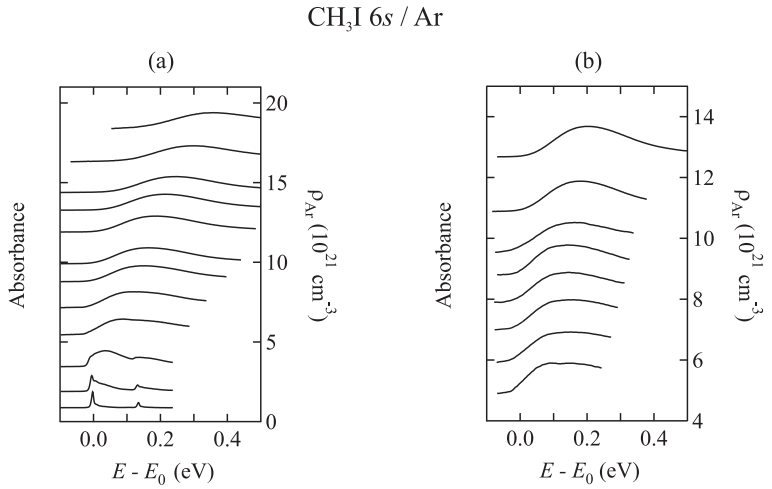

Figure 4.8: Selected photoabsorption spectra for the CH_3I $6s$ Rydberg transition in argon at (a) non-critical temperatures and (b) on an isotherm ($-121.8°$C) near the critical isotherm. The data are offset vertically by the argon perturber number density $\rho_{\rm Ar}$. The transition energy is $E_0 = 6.154$ eV for the unperturbed CH_3I $6s$ Rydberg transition. While all spectra have been normalized to 1 for future comparison to simulated line shapes, the integrated intensity is independent of $\rho_{\rm Ar}$.

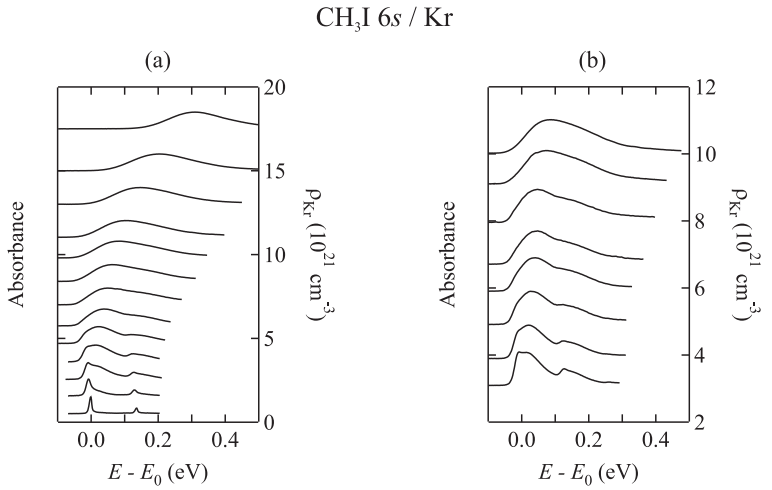

Figure 4.9: Selected photoabsorption spectra for the CH_3I 6s Rydberg transition in krypton at (a) non-critical temperatures and (b) on an isotherm (−63.3°C) near the critical isotherm. The data are offset vertically by the krypton number density ρ_{Kr}. The transition energy is $E_0 = 6.154$ eV for the unperturbed CH_3I 6s Rydberg transition. While all spectra have been normalized to 1 for future comparison with simulated line shapes, the integrated intensity is independent of ρ_{Kr}.

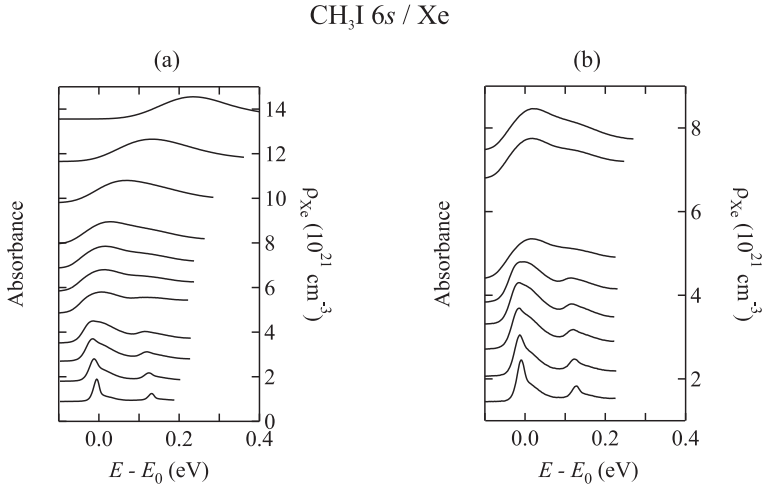

Figure 4.10: Selected photoabsorption spectra for the CH_3I 6s Rydberg transition in xenon at (a) non-critical temperatures and (b) on an isotherm (17.0°C) near the critical isotherm. The data are offset vertically by the xenon number density ρ_{Xe}. The transition energy is $E_0 = 6.154$ eV for the unperturbed CH_3I 6s Rydberg transition. While all spectra have been normalized to 1 for future comparison with simulated line shapes, the integrated intensity is independent of ρ_{Xe}.

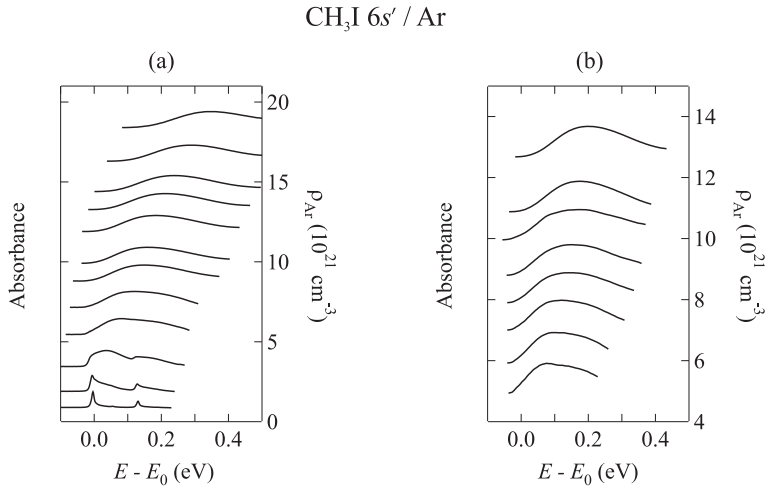

Figure 4.11: Selected photoabsorption spectra for the CH_3I $6s'$ Rydberg transition in argon at (a) non-critical temperatures and (b) on an isotherm ($-121.8°C$) near the critical isotherm. The data are offset vertically by the argon number density ρ_{Ar}. The transition energy is $E_0 = 6.767$ eV for the unperturbed CH_3I $6s'$ Rydberg transition. While all spectra have been normalized to 1 for future comparison with simulated line shapes, the integrated intensity is independent of ρ_{Ar}.

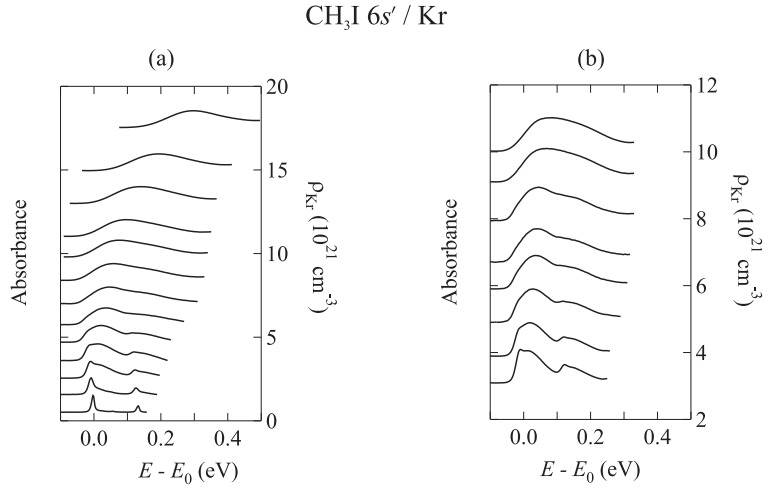

Figure 4.12: Selected photoabsorption spectra for the CH_3I $6s'$ Rydberg transition in krypton at (a) non-critical temperatures and (b) on an isotherm ($-63.3°C$) near the critical isotherm. The data are offset vertically by the krypton perturber number density ρ_{Kr}. The transition energy is $E_0 = 6.767$ eV for the unperturbed CH_3I $6s'$ Rydberg transition. While all spectra have been normalized to 1 for future comparison with simulated line shapes, the integrated intensity is independent of ρ_{Kr}.

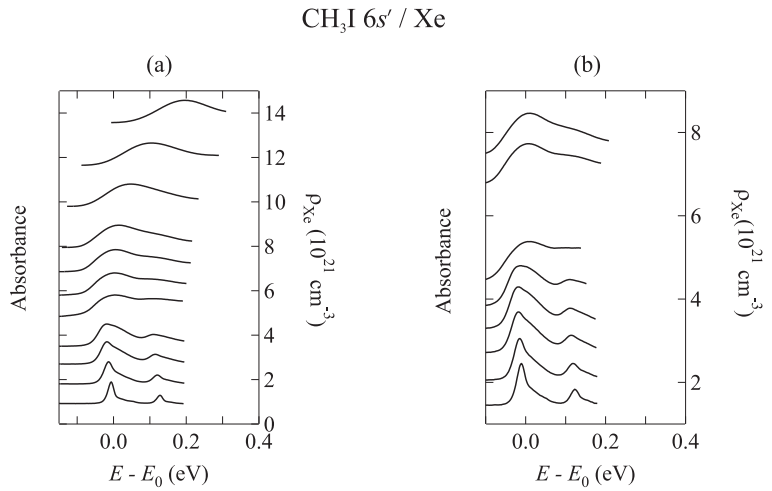

Figure 4.13: Selected photoabsorption spectra for the CH_3I $6s'$ Rydberg transition in xenon at (a) non-critical temperatures and (b) on an isotherm (17.0°C) near the critical isotherm. The data are offset vertically by the xenon perturber number density ρ_{Xe}. The transition energy is $E_0 = 6.767$ eV for the unperturbed CH_3I $6s'$ Rydberg transition. While all spectra have been normalized to 1 for future comparison with simulated line shapes, the integrated intensity is independent of ρ_{Xe}.

4.2.2 Line shape simulations

Although CH_3I in the rare gases does not form dimers or excimers, the accurate simulation of the low-n Rydberg transitions must include both the adiabatic transition, given by eq. (2.27) and denoted a in Fig. 2.7, as well as one quantum of the CH_3 deformation vibrational transition ν_2 in the excited state, given by eq. (2.28) and denoted b in Fig. 2.7. For all of the simulations presented here, we again chose eq. (3.14) for the ground-state perturber/perturber intermolecular interactions. All of the ground-state dopant/perturber interactions, on the other hand, were approximated with eq. (3.16). The excited-state dopant/ground state perturber interactions were again modeled using eq. (3.17). All intermolecular potential parameters except the Ar/Ar, Kr/Kr, Xe/Xe, CH_3I/Ar, and CH_3I/Kr ground state potential parameters were adjusted by hand to give the best simulated line shape in comparison to our ex-

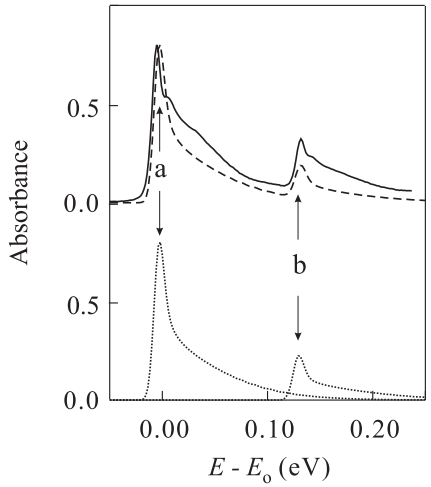

Figure 4.14: Photoabsorption spectra (solid line, relative intensity units) of the CH_3I $6s$ transition doped into Ar at an argon number density of $\rho_{Ar} = 1.89 \times 10^{21}$ cm^{-3} and a temperature of -79.8°C. a corresponds to eq. (2.27) and b to eq. (2.28). The dashed line is the complete simulation, while the dotted lines represent the individual simulation using (3.2) with the intermolecular potential parameters given in Table 4.2. For the adiabatic transition a, $E_0 = 6.154$ eV. For the vibrational transition b, $E_0 = 6.291$ eV.

perimental absorption spectra. (The Ar/Ar, Kr/Kr, Xe/Xe, CH_3I/Ar, and CH_3I/Kr ground-state potential parameters used are in accord with those employed in our earlier studies of the quasi-free electron energy in rare gas perturbers [32].) Table 4.2 gives the values for all intermolecular potential parameters used in the line shape simulations presented here. The relative intensities of the simulated bands were fixed by comparison to the absorption spectra of CH_3I at perturber number densities where all bands (i.e., the adiabatic and vibrational transitions) could be clearly identified. Experimentally, at low perturber number densities the ratio of the vibrational band intensity to the adiabatic transition intensity is 0.22 for both the CH_3I $6s$ and $6s'$ Rydberg states in all three perturbers. An example of a complete simulation of CH_3I low-n Rydberg state is shown in Fig. 4.14.

Table 4.2: Intermolecular potential parameters for all dopant/perturber systems.

	$\varepsilon/k_{\mathrm{B}}$ (K)	r_e (Å)	γ
Ar/Ar	119.5	3.826[a]	–
Kr/Kr	172.7	4.031[a]	–
Xe/Xe	229.0	4.552[a]	–
CH_3I/Ar	162.2	4.572[a]	–
CH_3I/Kr	196.7	4.676[a]	–
CH_3I/Xe	297.46	4.896[a]	–
CH_3I $6s$/Ar	110.0	6.300	12.75
CH_3I $6s$/Kr	245.0	6.200	11.30
CH_3I $6s$/Xe	400.0	6.390	10.25
CH_3I $6s$ ν_2/Ar	150.0	6.300	12.15
CH_3I $6s$ ν_2/Kr	225.0	6.300	10.75
CH_3I $6s$ ν_2/Xe	360.0	6.500	9.50
CH_3I $6s'$/Ar	110.0	6.300	12.75
CH_3I $6s'$/Kr	245.0	6.200	11.30
CH_3I $6s'$/Xe	400.0	6.290	10.25
CH_3I $6s'$ ν_2/Ar	150.0	6.300	12.15
CH_3I $6s'$ ν_2/Kr	225.0	6.300	10.75
CH_3I $6s'$ ν_2/Xe	360.0	6.350	9.50

[a]For a Lennard-Jones 6-12 potential, $\sigma = 2^{-1/6} r_e$.

Figs.4.15 - 4.20 present a comparison between the simulated line shapes (dotted lines) and the experimental absorption of the low-n CH_3I Rydberg transitions in the atomic perturbers at non-critical temperatures and on an isotherm near the critical isotherm of the perturber. As was true for Xe in Ar, the simulated spectra closely match the experimental spectra for all densities. Both the simulated and experimental line shapes show a slight red shift at low perturber number densities, followed by a strong blue shift at high perturber densities. Given the accuracy of the simulated line shapes, simulated spectra for CH_3I in Xe in the region where experimental data

were unobtainable are also presented in Figs. 4.17 and 4.20. We should note here that we were able to model the CH_3I $6s$ and $6s'$ Rydberg states in Ar using the same set of intermolecular potential parameters for both states. This behavior was also observed for the CH_3I $6s$ and $6s'$ Rydberg states in Kr. With identical potential parameters, the perturber induced shift $\Delta(\rho_P)$ will be the same for the $6s$ and $6s'$ states. The independence of $\Delta(\rho_P)$ on the dopant cationic core state is different from that observed for Xe low-n Rydberg states in Ar and will be discussed in more detail below. The accurate line shape simulations allow $\Delta(\rho_P)$ for the adiabatic transitions to be extracted using eq. (2.22).

4.2.3 Discussion

As with Xe in Ar, the accurate line shape simulations allow a moment analysis to be performed on the CH_3I low-n adiabatic Rydberg transition to obtain the perturber induced shift $\Delta(\rho_P)$ from eq.(2.22). The first moment of the simulated CH_3I $6s$ adiabatic transition is plotted as a function of the reduced perturber number density ρ_r in Fig. 4.21 and in Fig. 4.22 for the $6s$ and $6s'$ transition, respectively. The first moment of the simulated adiabatic band does not red shift at low perturber density, as was originally stated by Messing, *et al.* [47,48]. This absence of a red shift is again caused by the blue degradation of the adiabatic transition, which places the average energy (i.e., the first moment) of the band to the high energy side of the absorption maximum. The ground state interaction between CH_3I and the perturber is attractive, and therefore the ground state of the dopant is stabilized by the perturber solvent shell. The slight red shift of the absorption maximum observed at low perturber number densities is indicative of the stabilization of the CH_3I excited states by the perturber

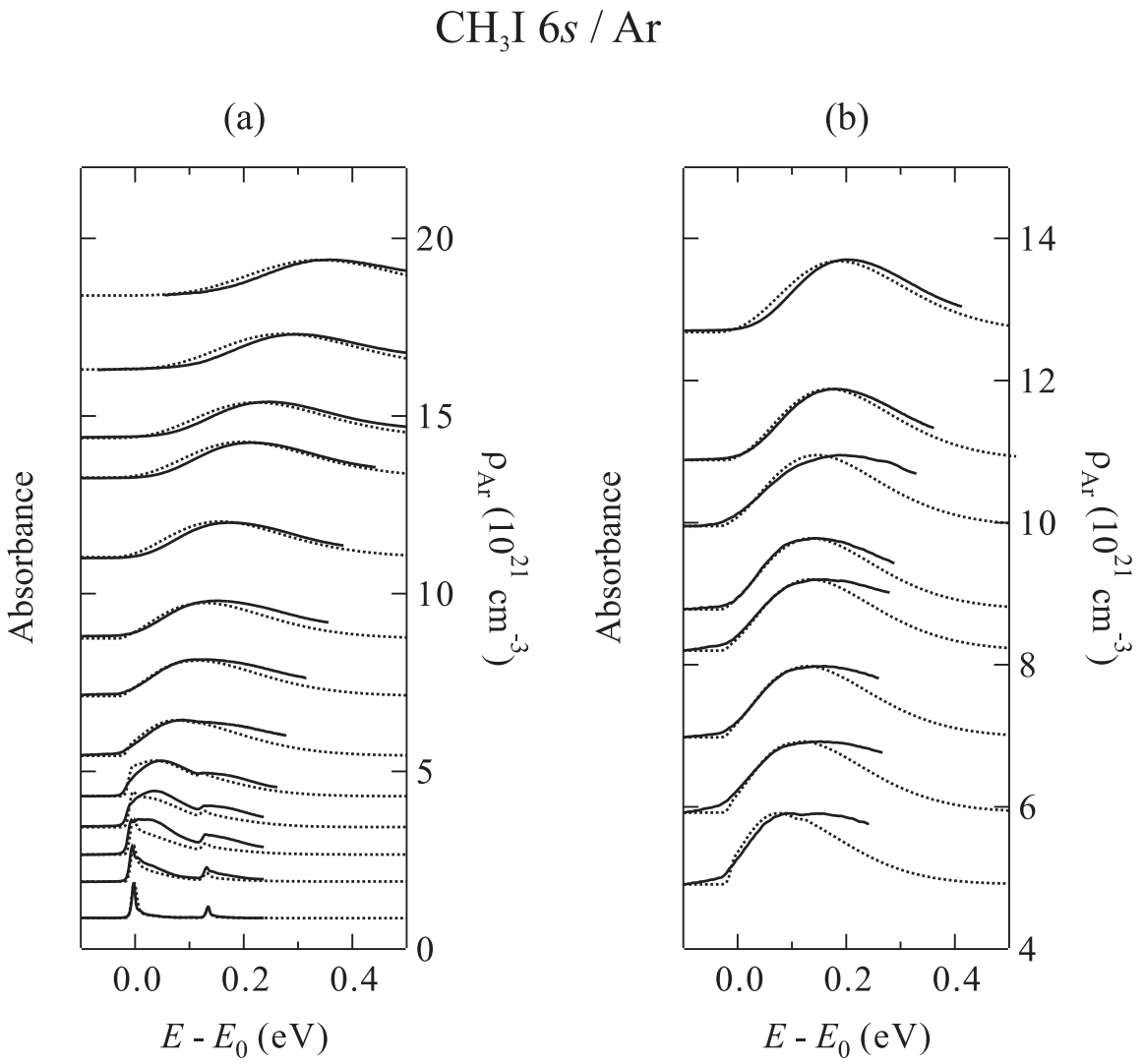

Figure 4.15: Selected photoabsorption spectra (—, relative units) and simulated line shapes ($\cdots$) for the CH_3I 6s Rydberg transition in argon at (a) non-critical temperatures and (b) on an isotherm ($-121.8°$C) near the critical isotherm. The data are offset vertically by the argon number density ρ_{Ar}. The transition energy is $E_0 = 6.154$ eV for the unperturbed CH_3I 6s Rydberg transition. The variation between experiment and simulation is caused by other vibrational transitions and by perturber-dependent lifetime broadening not modeled here.

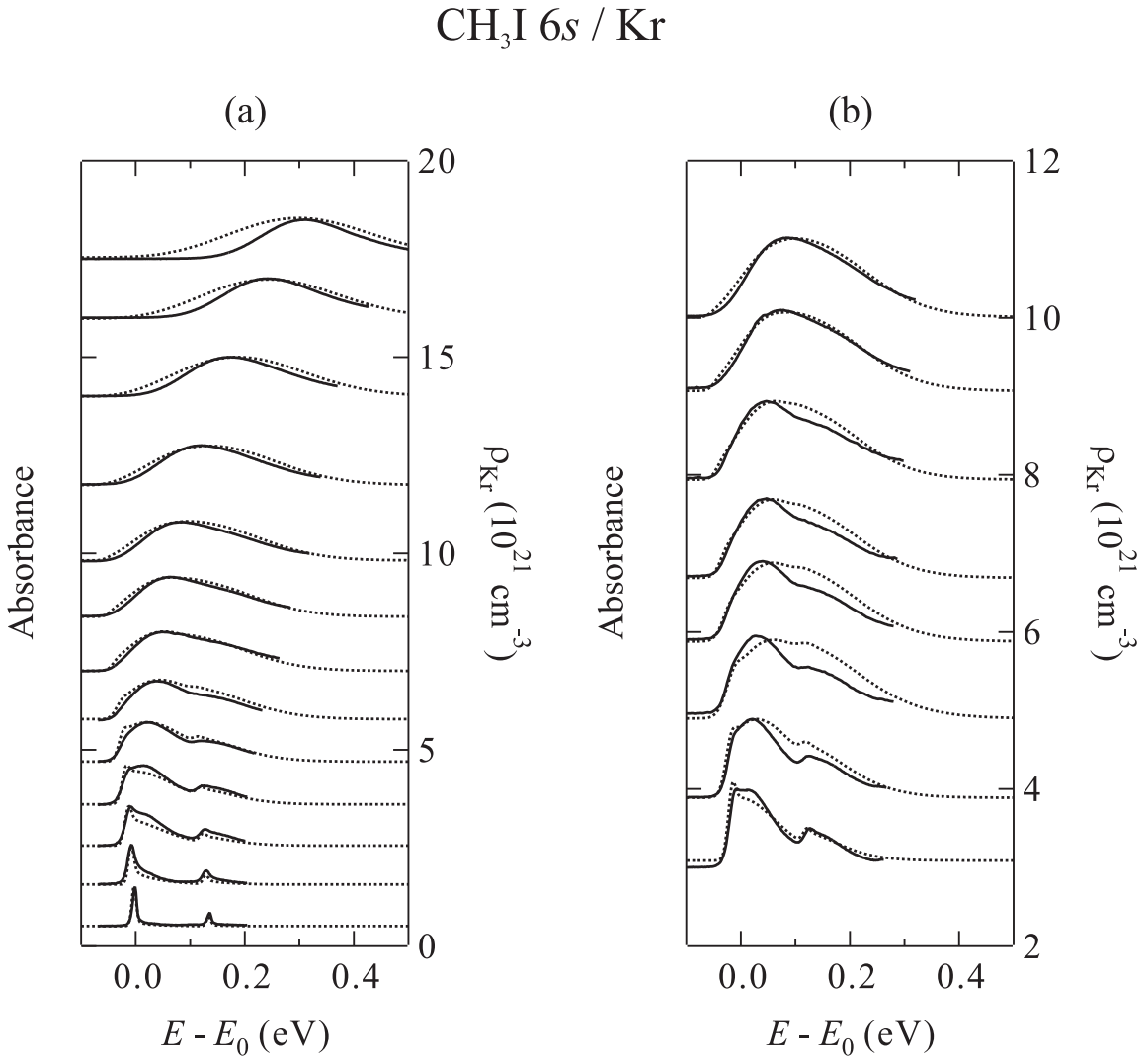

Figure 4.16: Selected photoabsorption spectra (—, relative units) and simulated line shapes ($\cdots$) for the CH_3I 6s Rydberg transition in krypton at (a) non-critical temperatures and (b) on an isotherm ($-63.3°C$) near the critical isotherm. The data are offset vertically by the krypton number density ρ_{Kr}. The transition energy is $E_0 = 6.154$ eV for the unperturbed CH_3I 6s Rydberg transition. The variation between experiment and simulation is caused by other vibrational transitions and by perturber-dependent lifetime broadening not modeled here.

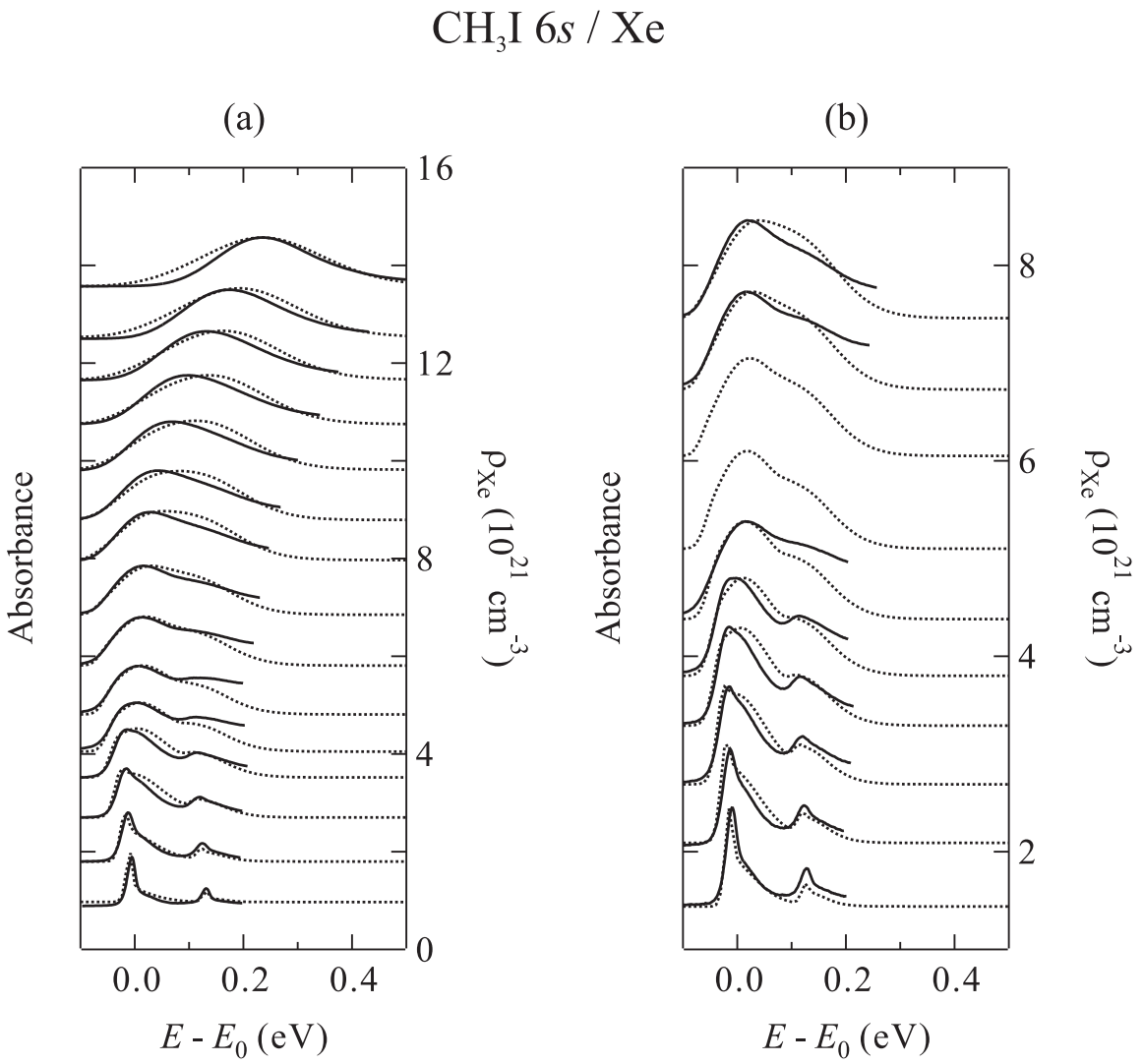

Figure 4.17: Selected photoabsorption spectra (—, relative units) and simulated line shapes ($\cdots$) for the CH_3I 6*s* Rydberg transition in xenon at (a) non-critical temperatures and (b) on an isotherm (17.0°C) near the critical isotherm. The data are offset vertically by the xenon number density ρ_{Xe}. The transition energy is $E_0 = 6.154$ eV for the unperturbed CH_3I 6*s* Rydberg transition. The variation between experiment and simulation is caused by other vibrational transitions and by perturber-dependent lifetime broadening not modeled here.

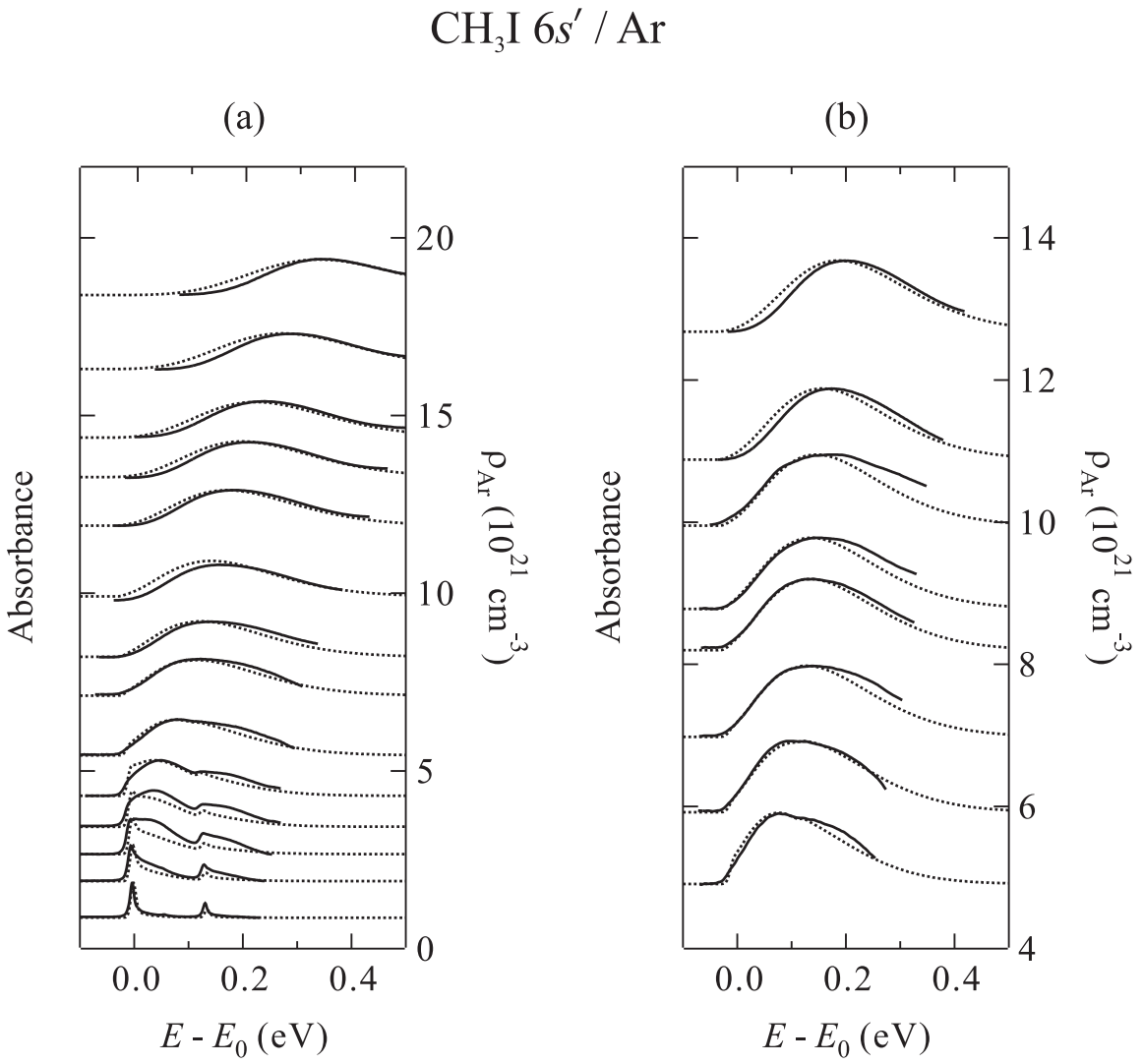

Figure 4.18: Selected photoabsorption spectra (—, relative units) and simulated line shapes ($\cdots$) for the CH_3I $6s'$ Rydberg transition in argon at (a) non-critical temperatures and (b) on an isotherm ($-121.8°C$) near the critical isotherm. The data are offset vertically by the argon number density ρ_{Ar}. The transition energy is $E_0 = 6.767$ eV for the unperturbed CH_3I $6s'$ Rydberg transition. The variation between experiment and simulation is caused by other vibrational transitions and by perturber-dependent lifetime broadening not modeled here.

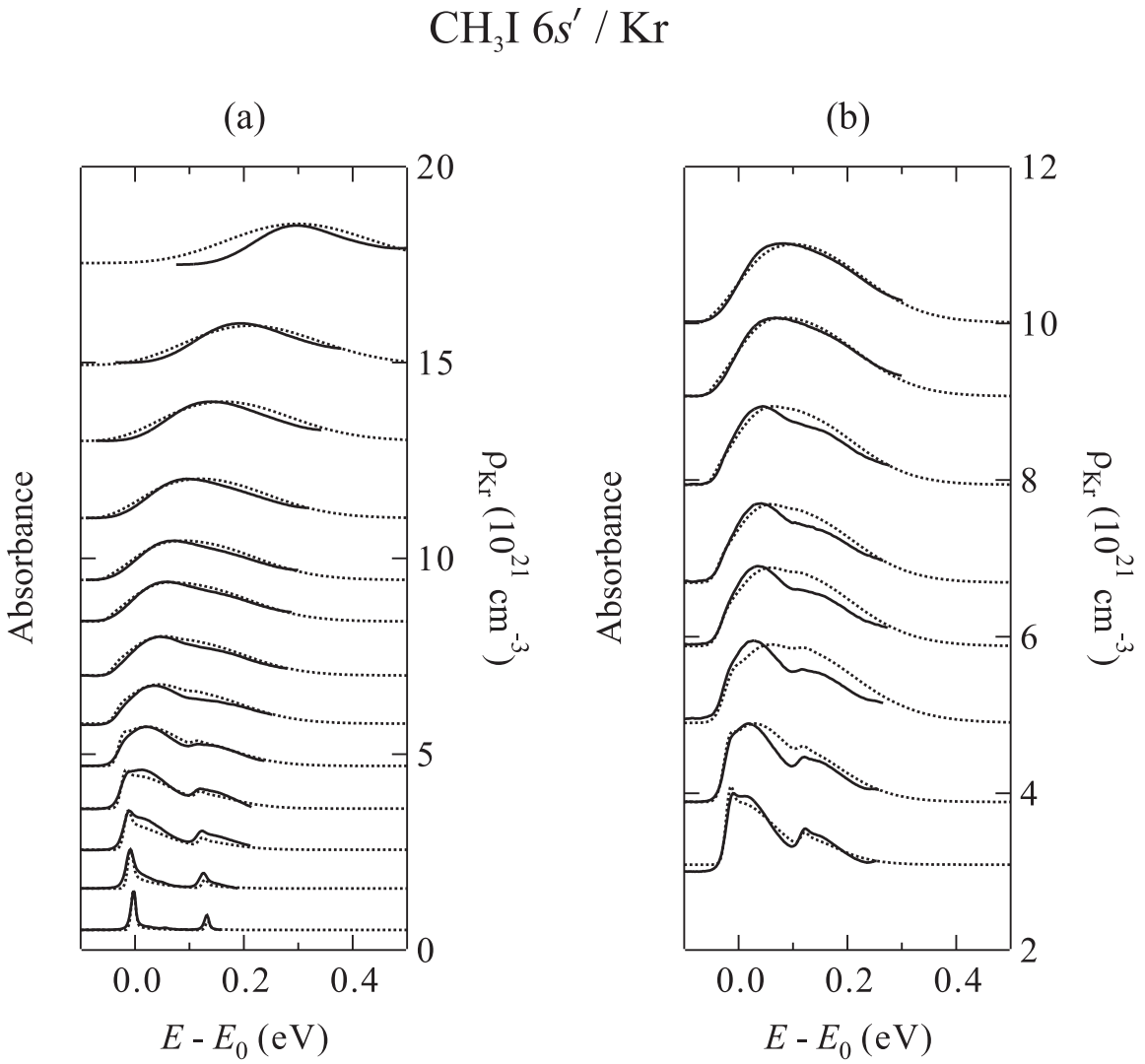

Figure 4.19: Selected photoabsorption spectra (—, relative units) and simulated line shapes ($\cdots$) for the CH_3I $6s'$ Rydberg transition in krypton at (a) non-critical temperatures and (b) on an isotherm ($-63.3°C$) near the critical isotherm. The data are offset vertically by the krypton number density ρ_{Kr}. The transition energy is $E_0 = 6.767$ eV for the unperturbed CH_3I $6s'$ Rydberg transition. The variation between experiment and simulation is caused by other vibrational transitions and by perturber-dependent lifetime broadening not modeled here.

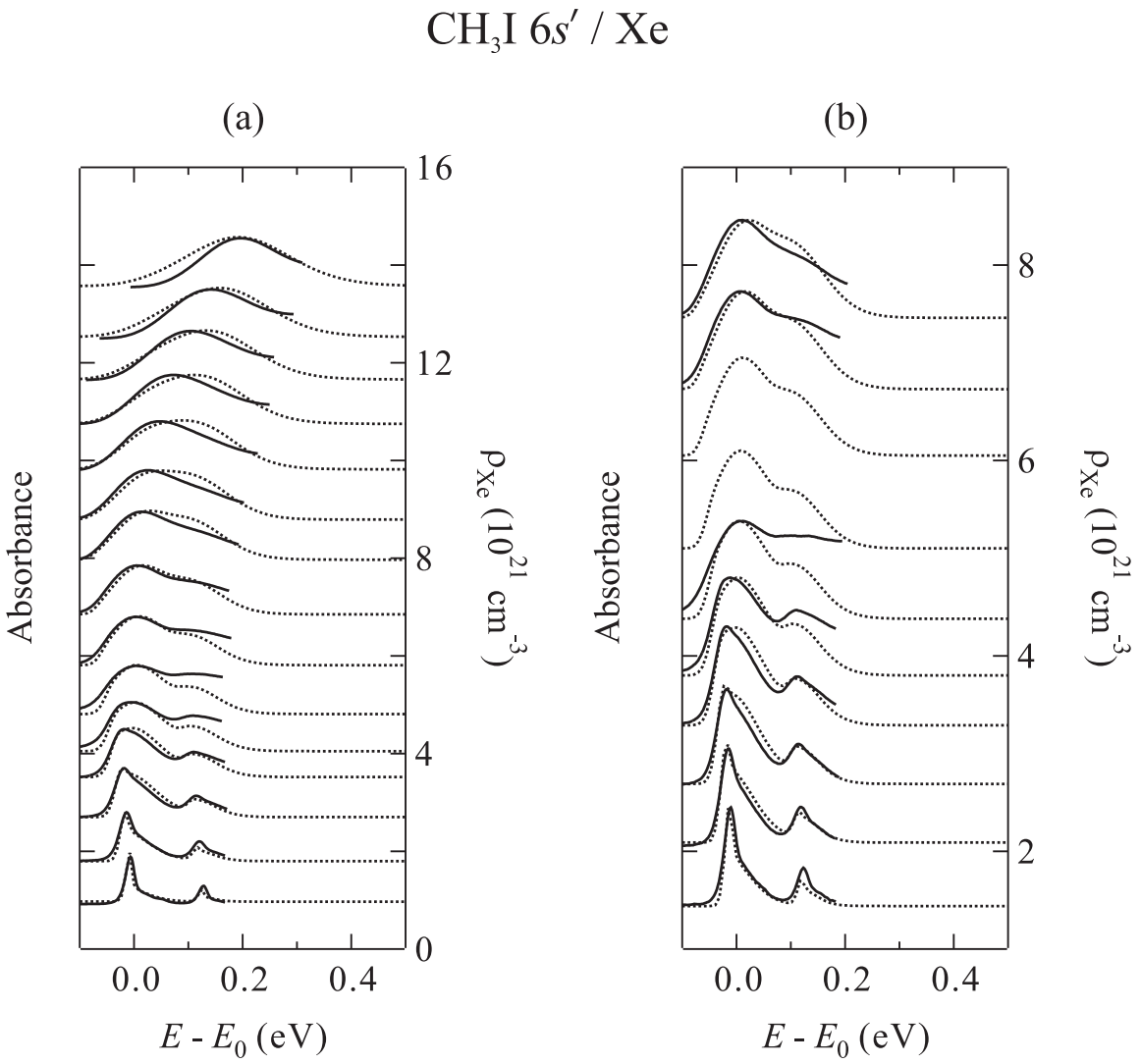

Figure 4.20: Selected photoabsorption spectra (—, relative units) and simulated line shapes ($\cdots$) for the CH_3I $6s'$ Rydberg transition in xenon at (a) non-critical temperatures and (b) on an isotherm (17.0°C) near the critical isotherm. The data are offset vertically by the xenon number density ρ_{Xe}. The transition energy is $E_0 = 6.767$ eV for the unperturbed CH_3I $6s'$ Rydberg transition. The variation between experiment and simulation is caused by other vibrational transitions and by perturber-dependent lifetime broadening not modeled here.

solvent shell. As the density increases, however, perturber molecules begin to shield the optical electron from the CH_3I cationic core, thereby increasing the excitation energy of the optical electron. Thus, as the perturber density increases, the energy of the excited state also increases, leading to a blue shift at higher perturber densities.

The $6s$ and $6s'$ Rydberg states correspond to an optical electron in the same Rydberg orbital, but with the cation in a different core state: $J = 3/2$ for s and $J = 1/2$ for s', where J is the total angular momentum of the core. In our investigation of $\Delta(\rho_{\mathrm{P}})$ for Xe in Ar (cf. Section 4.1), we found that $\Delta(\rho_{\mathrm{P}})$ of the $6s$ transition is 0.2 eV larger than that for the $6s'$ transition, indicating that the change in the core quadrupole moment affects the dopant/perturber interactions in a dense perturbing medium. However, $\Delta(\rho_{\mathrm{P}})$ for the CH_3I $6s$ and $6s'$ Rydberg transitions near the triple point density are identical to within experimental error for the perturbers argon and krypton, and differ only slightly (i.e., 30 meV) for CH_3I in xenon. The insensitivity of these CH_3I/perturber systems to the change in the CH_3I cationic core is probably caused by the large permanent dipole moment of CH_3I, which masks the effect of the quadrupole moment. Xenon, however, is extremely sensitive to electric fields because of its large polarizability. Therefore, the slight difference between the xenon induced shifts of the CH_3I $6s$ and $6s'$ Rydberg transitions may well be caused by small changes in the permanent dipole moment of CH_3I influencing changes in the induced dipole or local quadrupoles in the xenon perturber.

A critical point effect on the $6s$ and $6s'$ transition energies is also apparent in Figs. 4.21 and 4.22 for all three perturbers. The CH_3I $6s$ adiabatic transition in argon is blue-shifted by 20 meV near the critical temperature and critical density, while those

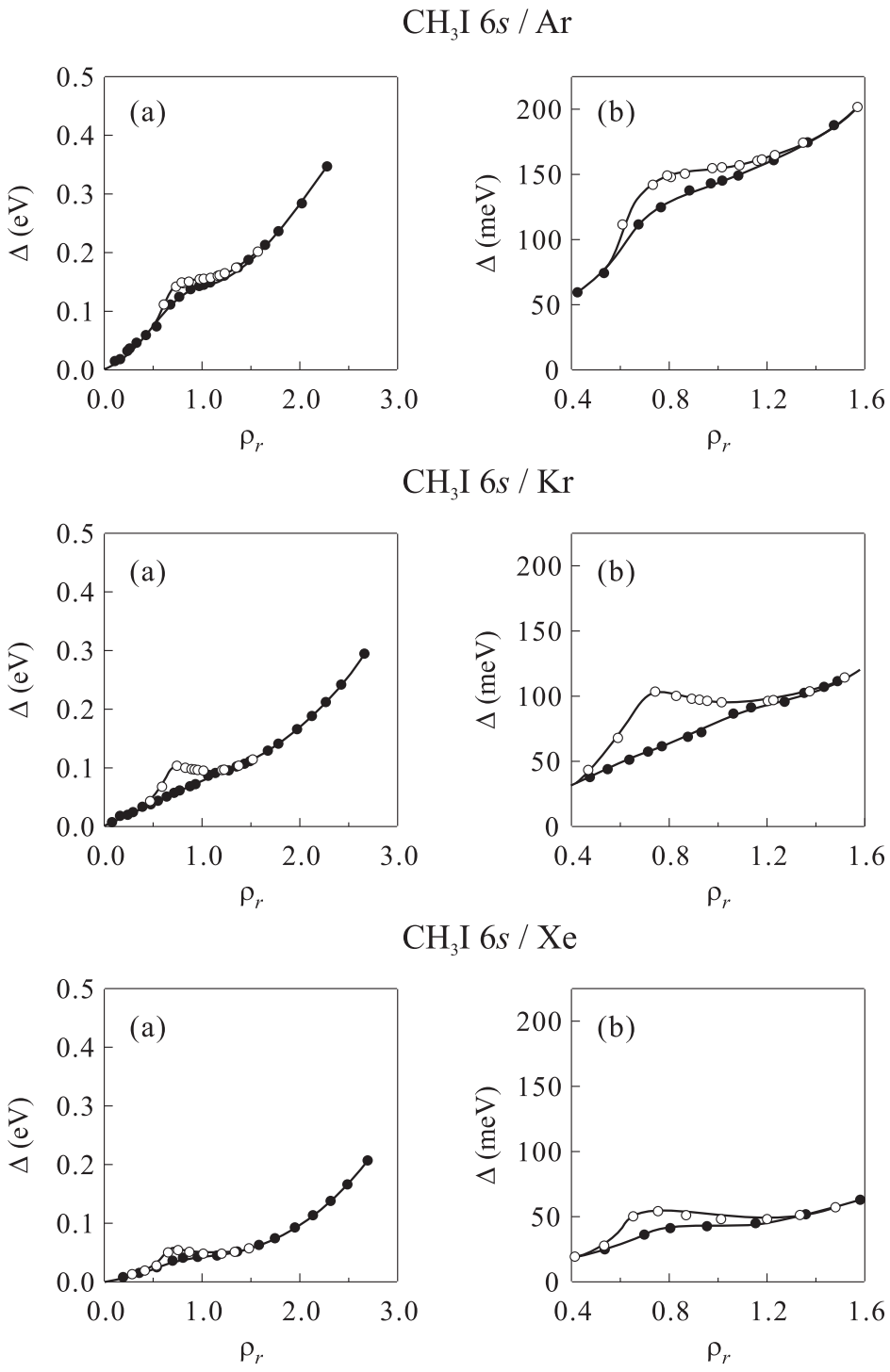

Figure 4.21: (a) The perturber induced shift $\Delta(\rho_{\rm P})$, as approximated by a moment analysis [i.e., eq. (2.22)], of the simulated primary transition for the CH_3I 6s Rydberg state as a function of the reduced perturber number density ρ_r for argon, krypton and xenon. (•), simulations obtained at noncritical temperatures; (∘), simulations near the critical isotherm. (b) An expanded view of $\Delta(\rho_{\rm P})$ near the perturber critical point. $\rho_c = 8.0 \times 10^{21}$ cm^{-3} for argon, $\rho_c = 6.6 \times 10^{21}$ cm^{-3} for krypton and $\rho_c = 5.0 \times 10^{21}$ cm^{-3} for xenon [32]. The solid lines provide a visual aid. See text for discussion.

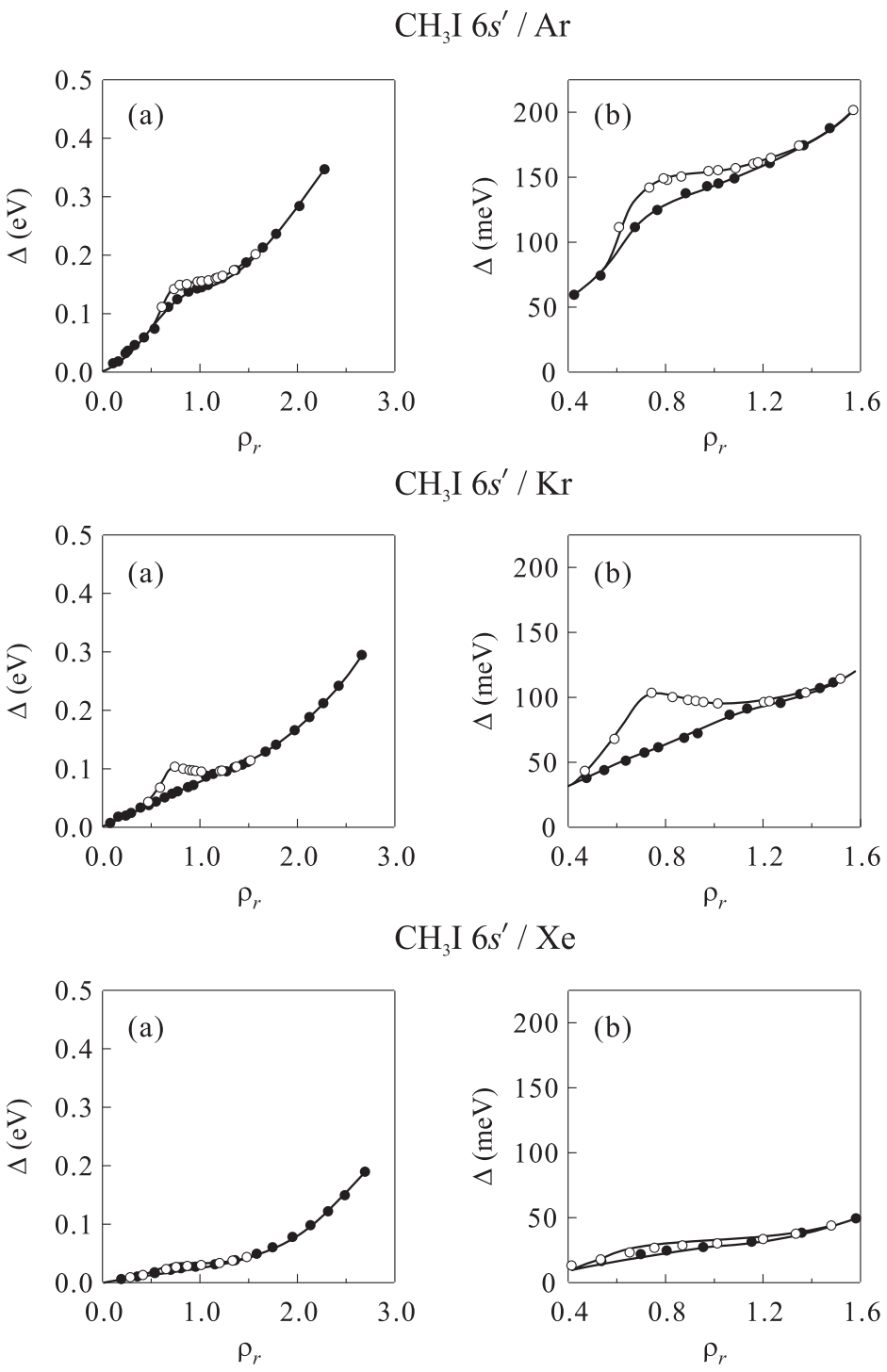

Figure 4.22: The perturber induced shift $\Delta(\rho_{\rm P})$, as approximated by a moment analysis [i.e., eq. (2.22)], of the simulated primary transition for the CH_3I $6s'$ Rydberg state as a function of the reduced perturber number density ρ_r. See the caption of Fig. 4.21.

in krypton and xenon are blue-shifted by 30 meV and 15 meV, respectively. Identical results are obtained for the CH_3I $6s'$ adiabatic transitions in argon and krypton. However, a smaller critical effect of 5 meV is observed for the CH_3I $6s'$ transition in xenon, which is related to the smaller overall blue shift of the CH_3I $6s'$ transition in comparison to the $6s$ transition.

In the low to medium density range, the energy of the absorption maximum for the $6s$ and $6s'$ CH_3I Rydberg states has a larger red shift in xenon, which is caused by the larger xenon polarizability. The CH_3I Rydberg states also broaden more quickly in xenon. This increased broadening is probably due to a combination of increased xenon polarizability and an increase in the probability of collisional de-excitation due to the size of xenon. However, $\Delta(\rho_{\text{P}})$ is larger for argon than for krypton and xenon. This change is caused by an overall decrease in the total number of perturber atoms within the first solvent shell surrounding the CH_3I dopant as the perturber atoms become larger. The variation in the critical point effect, with krypton having a larger effect than argon and xenon, is caused by the strength of the perturber/CH_3I interactions in comparison to the perturber/perturber interactions, coupled with the differences in the ground-state and excited-state dopant/perturber interaction potentials. The CH_3I/Kr ground state potential well depth is close (i.e., 24 K) to the Kr/Kr potential well depth. This implies that the CH_3I/Kr interactions near the krypton critical point will be comparable to the Kr/Kr interactions, thereby leading to a large increase in the local perturber density near the critical point of the perturber, and a larger critical point effect. Similarly, the critical point effect decreases as one goes from krypton to

argon to xenon because the difference in well depth for all intermolecular potentials increases.

4.3 Conclusions

In this chapter, we have shown that a semi-classical line shape simulation can be used to model a wide variety of dopant/atomic perturber systems with an appropriate choice of intermolecular potentials. We also illustrated that a single choice of intermolecular potentials was sufficient to simulate accurately the line shapes across the entire perturber density range at non-critical temperatures and along the critical isotherm. Using these simulations, we were able to extract the perturber induced shift of the primary electronic transitions, which allowed us to observe a perturber critical effect for the first time. The understanding of perturber effects on atomic and molecular transitions in dense atomic fluids has led to valuable insights into dopant/perturber intermolecular interactions. We have also shown that the local perturber structure around the dopant molecule strongly influences the strength of the perturber critical point effects on dopant electronic transitions. In the next chapter, we will extend our analysis to dopant/molecular perturber systems.

Chapter 5

Molecular perturbers

5.1 Xe 6s Rydberg state in CF_4

The Xe 6s Rydberg state doped into supercritical CF_4 [59] was investigated both experimentally and theoretically from low CF_4 number density to the density of the triple point liquid, at non-critical temperatures and on an isotherm (i.e., $-44.9°C$) near the CF_4 critical isotherm. The Xe 6s Rydberg state shows a similar perturber-induced energy shift and broadening as that observed in the previous Xe/atomic pertuber systems. However, no ground state dopant/perturber dimers or dopant/perturber excimers are formed in this system, as evidenced by the lack of satellite bands. Our group also attempted to measure the Xe 6s' Rydberg transition in supercritical CF_4. The Xe 6s' Rydberg state shows similar perturber-induced energy shifts at low to medium CF_4 number densities. Regretably, the ultrahigh purity CF_4 contains a nitrogen impurity that becomes concentrated enough to absorb light at higher CF_4 number densities. (The change in the nitrogen concentration is caused by the fact that the number density of CF_4 is increased by adding perturber gas containing the nitrogen impurity.) As the CF_4 number density increases, the Xe 6s' transition shifts to higher energies, which moves this transition into the region where the nitrogen

Table 5.1: Intermolecular potential parameters for eqs. (3.14) and (3.17) used to simulate the Xe $6s$ line shapes in CF_4.

	ε/k_B (K)	r_e (Å)	γ
CF_4/CF_4	181.02	4.708 [a]	–
Xe/CF_4	199.34	4.629[a]	–
Xe $6s/CF_4$	135.0	6.55	12.25

[a]For a Lennard-Jones 6-12 potential [i.e., eq. (3.14)], $\sigma = 2^{-1/6} r_e$.

absorption occurs. Thus, the Xe $6s'$ Rydberg state cannot be fully studied over the entire perturber density range. Because we lack a complete data set for the Xe $6s'$ transition, we chose not to show these data here.

Without blue satellite bands or vibrational transitions, the Xe $6s$ Rydberg state simulation only involves the primary Rydberg transition [i.e., eq. (2.24)]. For all the simulations presented here, we chose the Lennard-Jones 6-12 potential [i.e., eq. (3.14)] for both the ground-state CF_4/CF_4 intermolecular interaction and the ground-state Xe/CF_4 interaction. The excited-state Xe/ground-state CF_4 interaction was again modeled using the exponential-6 potential [i.e., eq. (3.17)]. All intermolecular potential parameters were adjusted by hand to give the best simulated line shape in comparison to our experimental absorption spectra. Table 5.1 gives the values for all intermolecular potential parameters used in the line shape simulation presented here. Figs. 5.1a and 5.1b show a comparison between the simulated line shapes (dotted lines) and the experimental absorption spectra (solid lines) for the Xe $6s$ transition at non-critical temperatures (cf. Fig. 5.1a) and on an isotherm (-44.9°C) near the critical isotherm (cf. Fig. 5.1b). The simulated spectra closely match the experimental spectra for all densities. With these accurate line shape simulations, moment analyses can be performed on the Xe $6s$ transition to investigate perturber critical

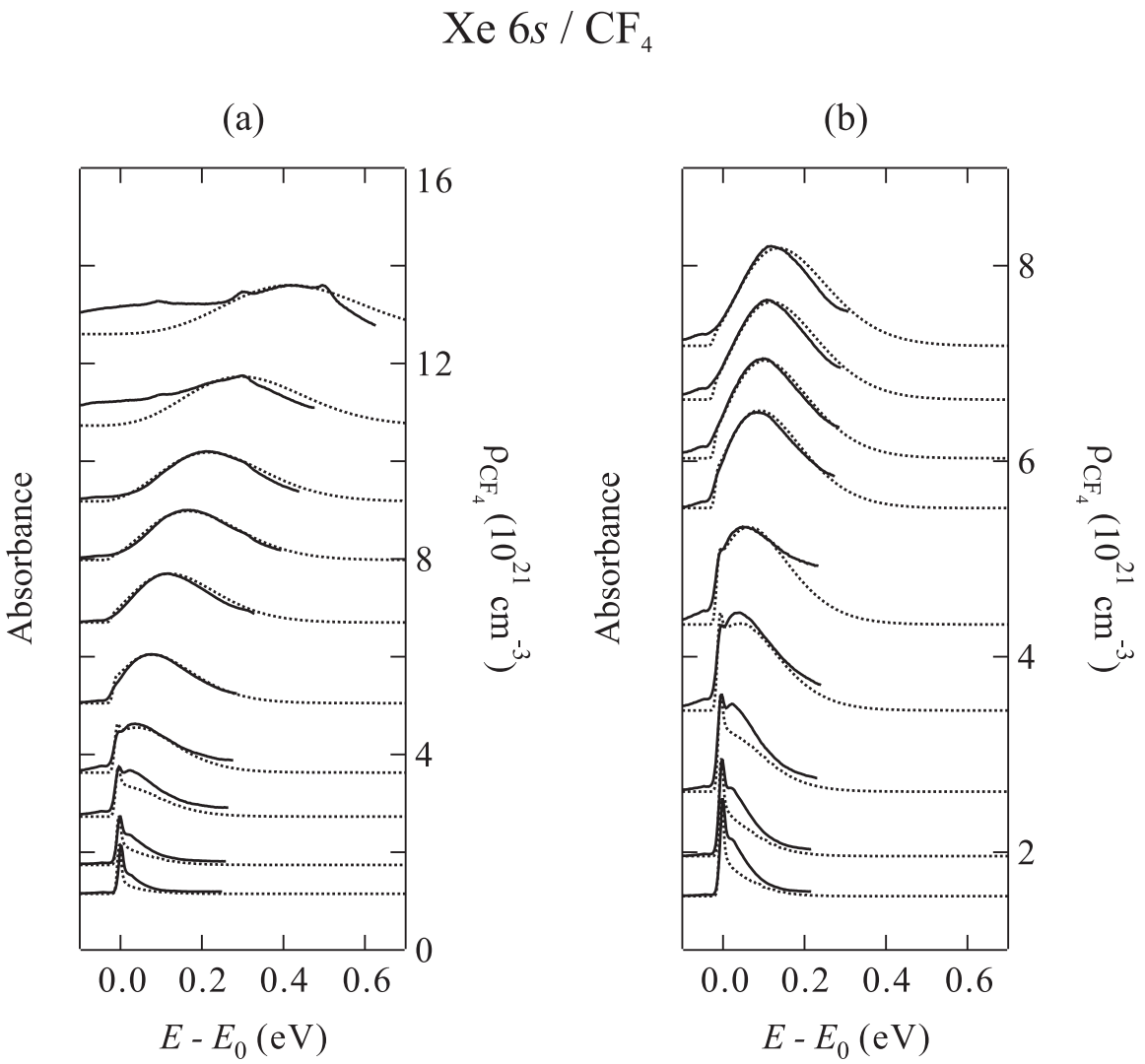

Figure 5.1: Selected photoabsorption spectra (–, relative scale) and simulated line shapes ($\cdots$) for the Xe 6*s* Rydberg transition at (a) non-critical temperatures and (b) on an isotherm (i.e., −44.9°C) near the critical isotherm. The data are offset vertically by the CF_4 number density ρ_{CF_4}. The transition energy is $E_0 = 8.424$ eV for the unperturbed Xe 6*s* Rydberg transition. The variation between experiment and simulation may be caused by perturber-dependent lifetime broadening not modeled here. While all experimental spectra have been normalized to 1 for comparison with the simulated line shapes, the integrated intensity is independent of ρ_{CF_4}. The obvious bumps on the 6*s* Rydberg absorbance band at high CF_4 number densities are caused by the strong absorption of a nitrogen impurity.

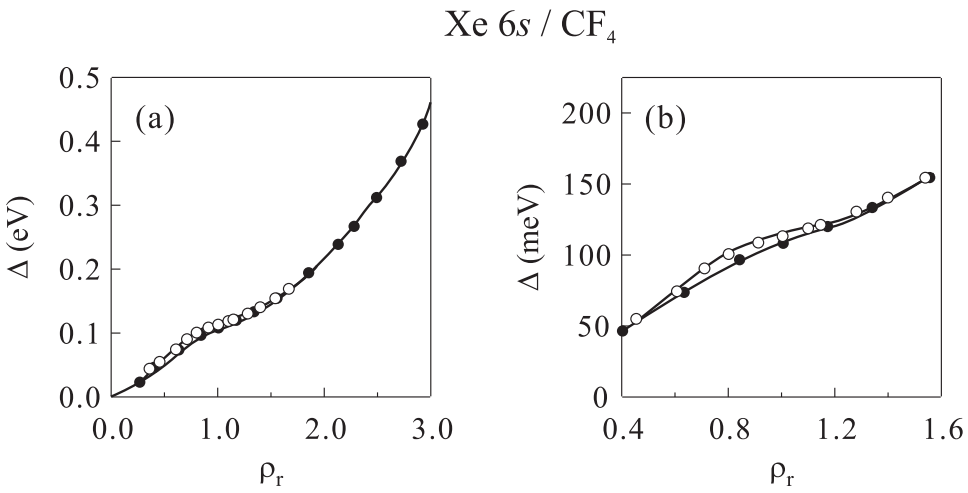

Figure 5.2: (a) The CF_4 induced shift $\Delta(\rho_{CF_4})$ of the Xe $6s$ transition as a function of reduced number density ρ_r at (•) non-critical temperatures and (○) along an isotherm (i.e., −44.9°C) near the CF_4 critical isotherm. In order to aid comparison between all data sets, we chose to keep the same energy and reduced density scale, even though this prevents the final density point from showing on this graph. (b) An expanded view of $\Delta(\rho_{CF_4})$ near the CF_4 critical point. $\rho_c = 4.309\times10^{21}\text{cm}^{-3}$ for CF_4 [83–86]. The solid lines are a visual aid. See text for discussion.

point effects. The average CF_4 induced shift $\Delta(\rho_{CF_4})$ of the Xe $6s$ transition as a function of reduced CF_4 number density is shown in Fig. 5.2. Fig. 5.2b shows an enhanced view of the perturber critical region with a total critical point effect of ∼ 10 meV. The reason for such a small critical point effect will be discussed later in this chapter.

5.2 CH_3I low-n Rydberg states in CH_4

The CH_3I $6s$ and $6s'$ Rydberg states doped into supercritical CH_4 [59] were investigated both experimentally and theoretically from low CH_4 number density to the density of the triple point liquid, at non-critical temperatures and on an isotherm (i.e., − 81.5°C) near the CH_4 critical isotherm. The CH_3I $6s$ and $6s'$ Rydberg states show similar perturber-induced energy shifts and broadening as that observed in the

CH_3I/atomic pertuber systems discussed in Section 4.2. Both the adiabatic transition and the vibrational transition broaden and shift as the number density of CH_4 increases. In comparison to the atomic perturber systems, both the CH_3I $6s$ and $6s'$ Rydberg transitions in CH_4 broaden faster on both the low energy and high energy side of the transition bands. This increased broadening is caused by the interaction of the vibrational and rotational degrees of freedom in the perturber with those in the excited state dopant, creating more pathways for energy distribution during the dopant/perturber interaction. Moreover, the CH_3I line shapes distinctly change near the critical density and temperature of the perturber (cf. Figs. 5.3b and 5.4b below).

As discussed in Section 4.2, accurate modeling of the CH_3I low-n Rydberg state absorption spectra requires the simulation of both the adiabatic transition and the vibrational transition ν_2, which are denoted a and b in Fig. 2.7, respectively. For all of the simulations, we chose the two-Yukawa potential in eq. (3.15) for the ground state CH_4/CH_4 intermolecular interactions. Although either the Lennard-Jones 6-12 potential or the two-Yukawa potential with proper parameters can be used to simulate the experimental CH_3I line shapes in CH_4, the two-Yukawa form showed a better fit to the quasi-free electron energy and the equation of state [39,89]. (We should note here that the insensitivity of these calculations to the ground state perturber/perturber intermolecular potential arises because this potential is only necessary to calculate the perturber/perturber radial distribution function used in the third order interaction term of eq. (3.2).) Again, the ground-state CH_3I/CH_4 interaction is taken to be the modified Stockmeyer intermolecular potential in the Lennard-Jones 6-12 form [i.e., eq. (3.14)], and the excited-state CH_3I/CH_4 interaction is a standard exponential-6

Table 5.2: Intermolecular potential parameters for eqs. (3.15), (3.14) and (3.17) used to simulate the CH_3I absorption line shapes in CH_4.

	ε/k_B (K)	r_e (Å)	γ	κ_0 (Å)	z_1 (Å^{-1})	z_2 (Å^{-1})
CH_4/CH_4	141.5	3.704[a]	–	8.50	0.90	4.25
CH_3I/CH_4	195.80	4.243[a]	–	–	–	–
CH_3I $6s/CH_4$	145.0	6.55	10.10	–	–	–
CH_3I $6s$ ν_2/CH_4	105.0	6.65	9.95	–	–	–
CH_3I $6s'/CH_4$	145.0	6.55	10.10	–	–	–
CH_3I $6s'$ ν_2/CH_4	105.0	6.65	9.95	–	–	–

[a]For a two-Yukawa potential [i.e., eq. (3.15)] and a Lennard-Jones 6-12 potential [i.e., eq. (3.14)], $\sigma = 2^{-1/6} r_e$.

potential [i.e., eq. (3.17)]. All the intermolecular potential parameters are adjusted manually to achieve the best fit to the experimental absorption spectra, and these parameters are presented in Table 5.2. The intensity of the simulated vibrational transition relative to that of the adiabatic transition is again taken to be 0.22.

Fig. 5.3 shows a comparison between the simulated line shapes (dotted lines) and the experimental absorption spectra (solid lines) for the CH_3I $6s$ transition at non-critical temperatures (cf. Fig. 5.3a) and on an isotherm (−81.5°C) near the critical isotherm (cf. Fig. 5.3b). Similar data are presented in Figs. 5.4a and 5.4b for the CH_3I $6s'$ transition in CH_4. Clearly, the simulated spectra closely match the experimental spectra for all perturber densities. (There are slight differences in the simulated line shapes and the experimental data near the critical density and temperature. These differences are probably caused by increased perturber-induced lifetime broadening due to the large correlation length of the solvent and the added degrees of freedom in the solvent.) With these accurate line shape simulations, moment analyses were performed on the CH_3I $6s$ and $6s'$ Rydberg transitions in order to investigate perturber critical point effects. The average CH_4 induced shift $\Delta(\rho_{CH_4})$

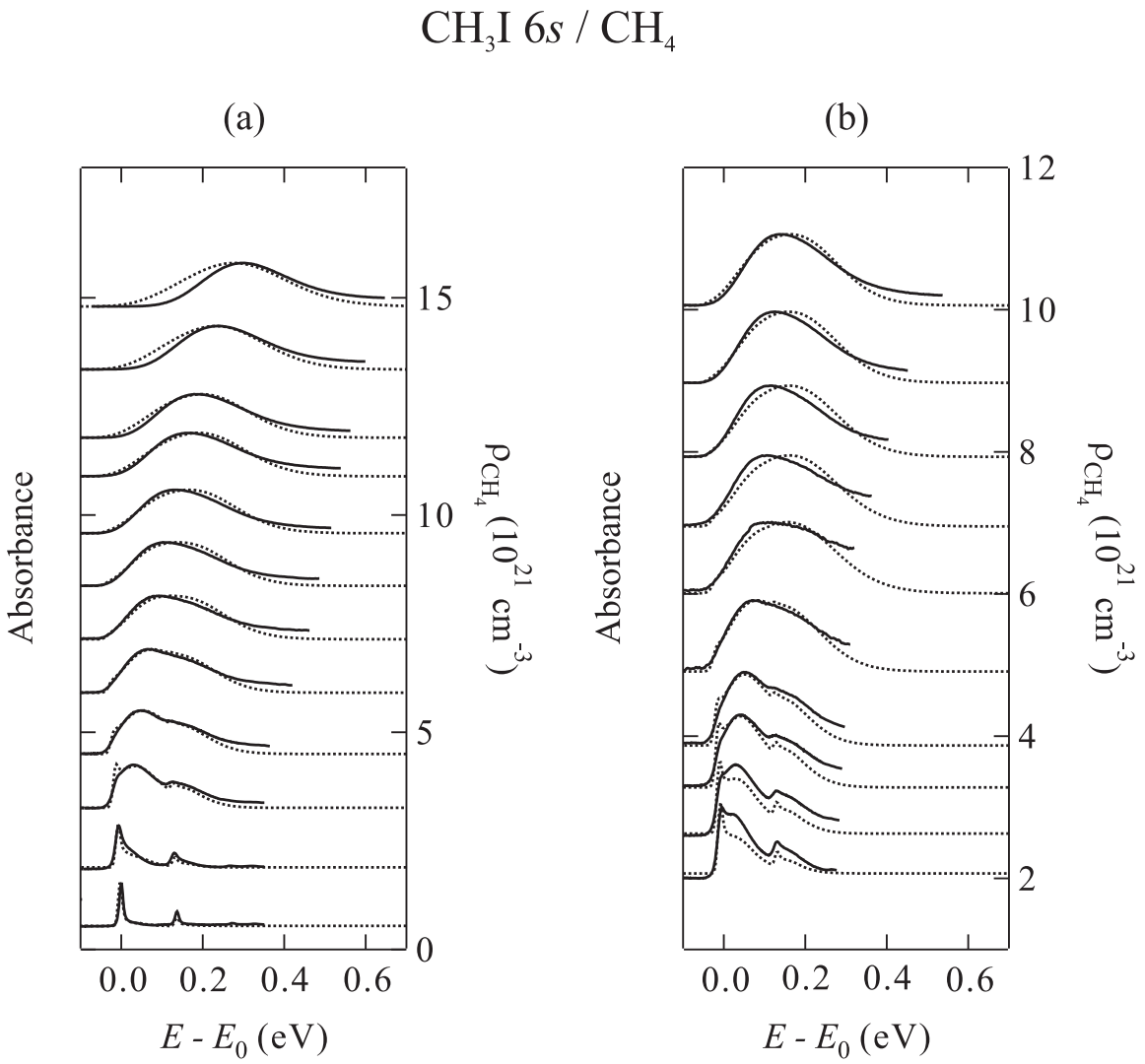

Figure 5.3: Selected photoabsorption spectra (–, relative scale) and simulated line shapes ($\cdots$) for the CH_3I 6*s* Rydberg transitions at (a) non-critical temperatures and (b) on an isotherm ($-81.5°C$) near the critical isotherm. The data are offset vertically by the CH_4 number density ρ_{CH_4}. The transition energy is $E_0 = 6.154$ eV for the unperturbed CH_3I 6*s* Rydberg transition. The variation between experiment and simulation is caused by other vibrational transitions and by perturber-dependent lifetime broadening not modeled here. While all experimental spectra have been normalized to 1 for comparison with the simulated line shapes, the integrated intensity is independent of ρ_{CH_4}.

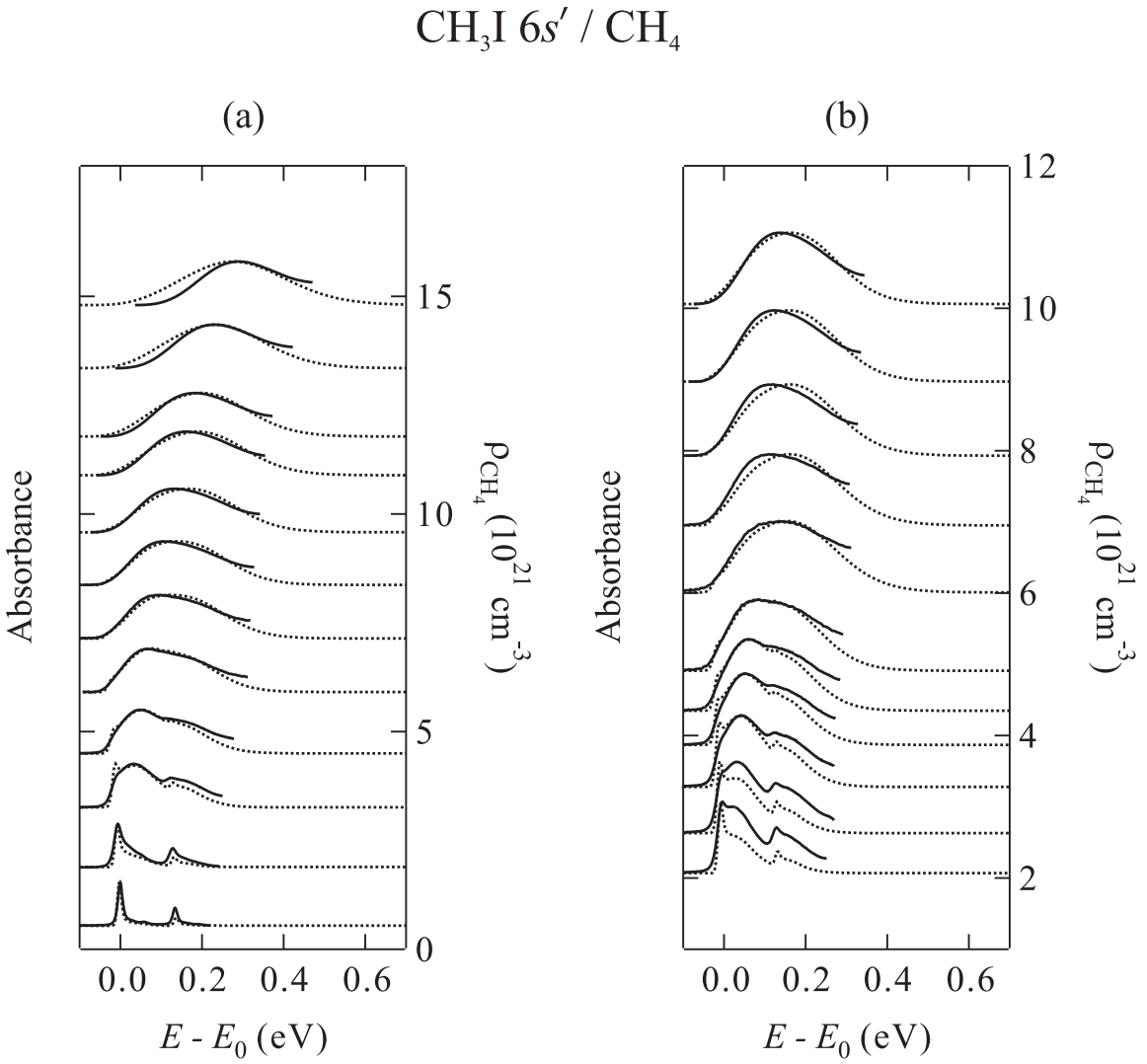

Figure 5.4: Selected photoabsorption spectra (–, relative scale) and simulated line shapes ($\cdots$) for the CH_3I $6s'$ Rydberg transitions at (a) non-critical temperatures and (b) on an isotherm ($-81.5°C$) near the critical isotherm. The data are offset vertically by the CH_4 number density ρ_{CH_4}. The transition energy is $E_0 = 6.767$ eV for the unperturbed CH_3I $6s'$ Rydberg transition. The variation between experiment and simulation is caused by other vibrational transitions and by perturber-dependent lifetime broadening not modeled here. While all experimental spectra have been normalized to 1 for comparison with the simulated line shapes, the integrated intensity is independent of ρ_{CH_4}.

of the CH_3I adiabatic transitions as a function of reduced CH_4 number density are shown in Fig. 5.5. Fig. 5.5b enlarges the perturber critical region where a significant critical point effect ($\sim$ 50 meV) appears. The reasons for this large critical point effect will be discussed later in this chapter.

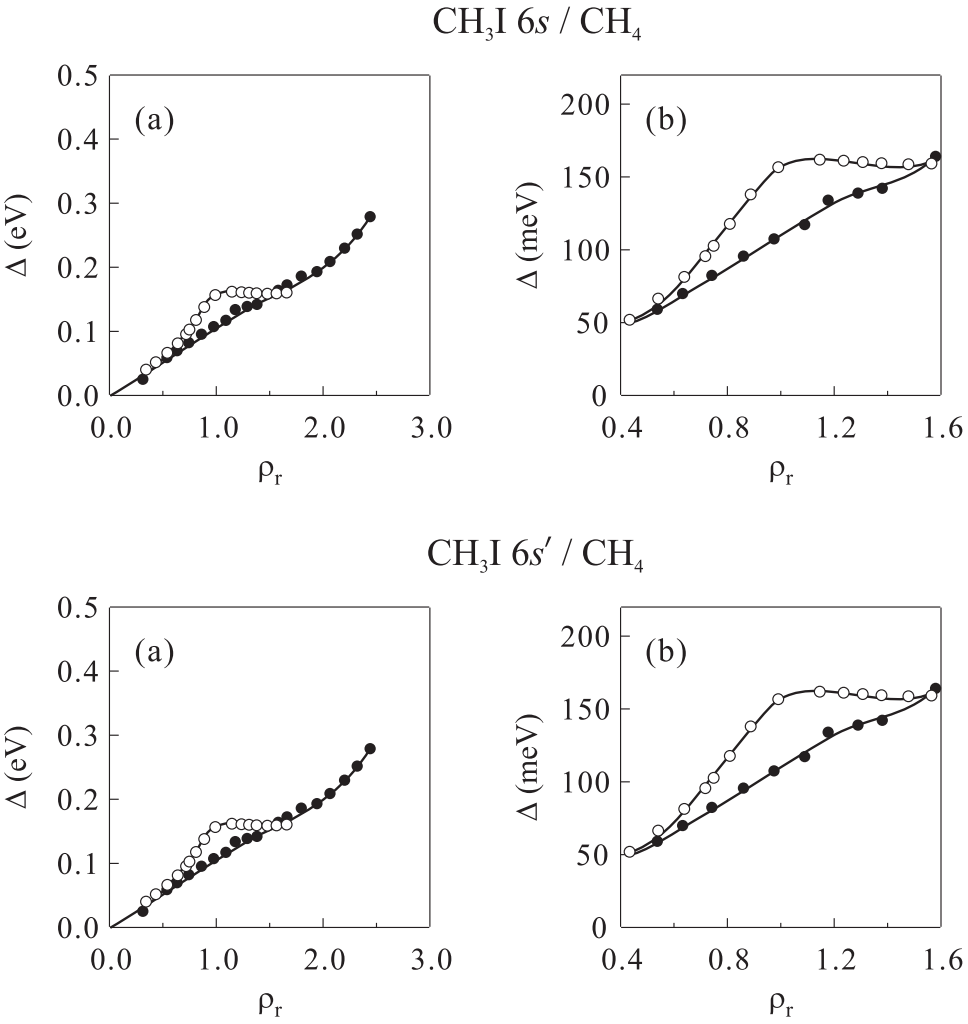

Figure 5.5: (a) The CH_4 induced shift $\Delta(\rho_{CH_4})$ of the CH_3I $6s$ and $6s'$ Rydberg transitions as a function of reduced number density ρ_r at (•) non-critical temperatures and (○) along an isotherm near the critical isotherm. (b) An expanded view of $\Delta(\rho_{CH_4})$ near the CH_4 critical point. $\rho_c = 6.068\times10^{21}\text{cm}^{-3}$ for CH_4 [82]. The solid lines are a visual aid. See text for discussion.

Table 5.3: Intermolecular potential parameters for eqs. (3.14) and (3.17) used to simulate the CH_3I $6s$ line shapes in CF_4.

	ε/k_B (K)	r_e (Å)	γ
CF_4/CF_4	181.02	4.708 [a]	–
CH_3I/CF_4	256.01	5.016 [a]	–
CH_3I $6s/CF_4$	185.0	6.84	12.10
CH_3I $6s$ ν_2/CF_4	135.0	6.84	11.90
CH_3I $6s'/CF_4$	185.0	6.84	12.10
CH_3I $6s'$ ν_2/CF_4	135.0	6.84	11.90

[a]For a Lennard-Jones 6-12 potential [i.e., eq. (3.14)], $\sigma = 2^{-1/6} r_e$.

5.3 CH_3I low-n Rydberg states in CF_4

The CH_3I $6s$ and $6s'$ Rydberg states doped into supercritical CF_4 [59] were measured from low CF_4 number density to the density of the triple point liquid, at various non-critical temperatures and on an isotherm (i.e., -44.9°C) near the CF_4 critical temperature. All absorption spectra were compared to a full line shape simulation that included the adiabatic transition and a dominant vibrational transition (denoted by a and b, respectively, in Fig. 2.7). A Lennard-Jones 6-12 potential was used for the ground state CF_4/CF_4 interaction, since we do not have enough experimental data for the quasi-free electron energy in CF_4 [89] to independently fix this intermolecular potential. The modified Stockmeyer potential in a Lennard-Jones 6-12 form was used for the ground state CH_3I/CF_4 interaction. We again employed a standard exponential-6 potential for all of the excited-state CH_3I/CF_4 interactions. All intermolecular potential parameters (cf. Table 5.3) were manually varied to achieve the best fit to the experimental spectra. The ratio between the intensity of the vibrational transition and that of the adiabatic transition was again maintained at 0.22.

Figs. 5.6 and 5.7 show a comparison between the simulated line shapes (dotted lines) and the experimental absorption spectra (solid lines) for the CH_3I $6s$ and $6s'$ transitions at non-critical temperatures (cf. Figs. 5.6a and 5.7a) and on an isotherm ($-44.9°C$) near the critical isotherm (cf. Figs. 5.6b and 5.7b). The simulated spectra again closely match the experimental spectra for all perturber number densities. The accurate line shape simulations allow us to perform a moment analysis on the primary Rydberg transition in order to determine the average perturber-induced energy shift. The average CF_4 induced shift $\Delta(\rho_{CF_4})$ of the CH_3I $6s$ and $6s'$ transitions as a function of reduced CF_4 number density is shown in Fig. 5.8a. Fig. 5.8b presents an enhanced view of the perturber critical region with a critical point effect of ~ 25 meV.

5.4 Discussion

The low-n Rydberg state transitions in supercritical molecular fluids show similar behavior to that seen in atomic fluids. The first moment $\Delta(\rho_P)$ of the simulated adiabatic transitions are plotted as functions of the reduced perturber density ρ_r in Figs. 5.2, 5.5 and 5.8. All of these graphs illustrate a perturber-induced blue shift from low density to the density of the triple point liquid with a striking change in the shift near the critical density and temperature of the perturber. The first solvent shell of the perturber shields the optical electron from the cationic core. Thus, as the perturber number density increases, the low-n Rydberg state excitation energy shifts more to the blue. Near the perturber critical point region, the local density of the perturber increases due to increased perturber fluctuations. Thus, the low-n Rydberg state excitation energy shifts more to the blue near the critical point. As mentioned previously, the experimental spectra also show that the low-n Rydberg transitions

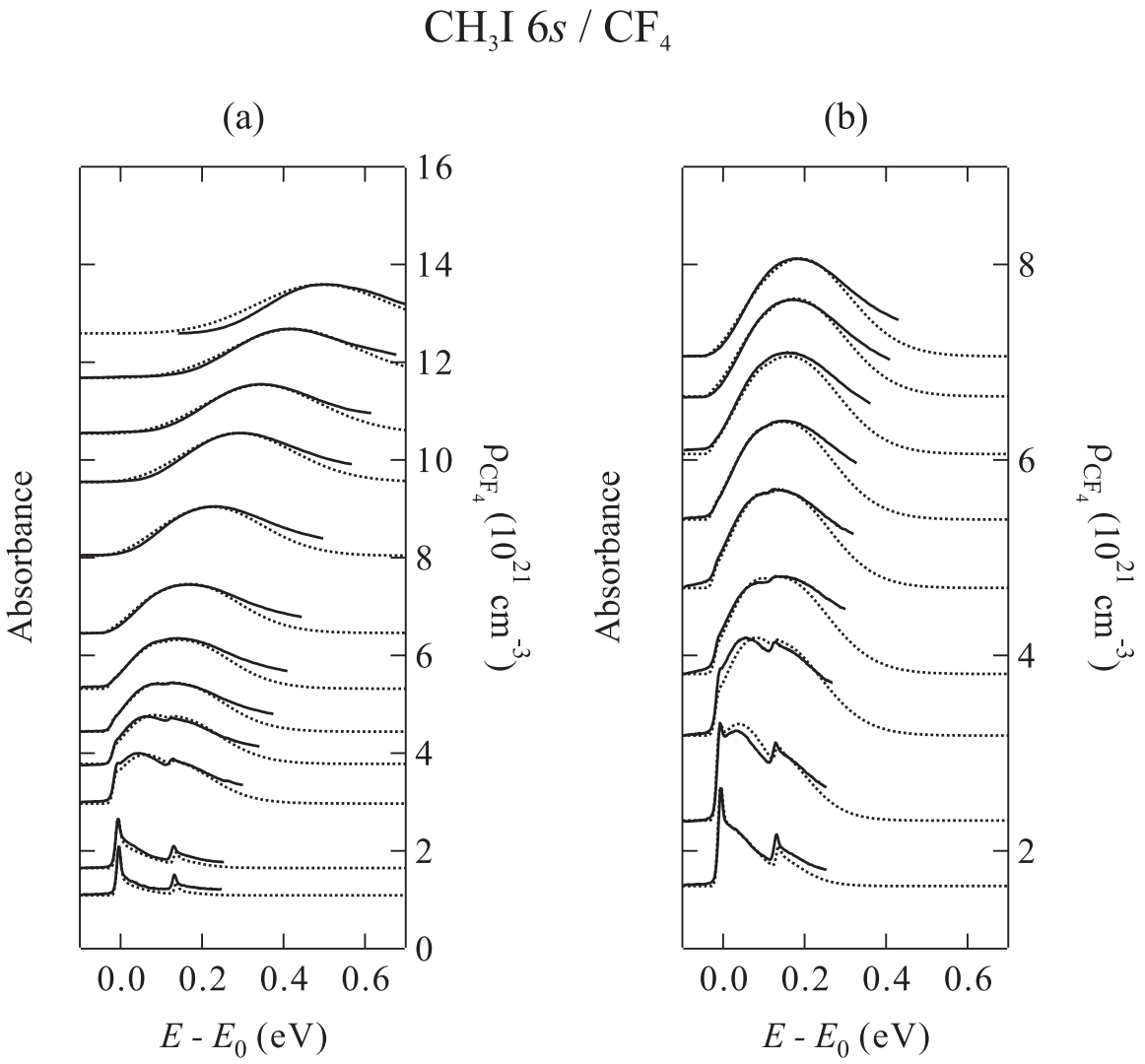

Figure 5.6: Selected photoabsorption (–, relative scale) and simulated line shapes ($\cdots$) for the CH_3I $6s$ Rydberg transition at (a) non-critical temperatures and (b) on an isotherm (-44.9°C) near the critical isotherm. The data are offset vertically by the CF_4 number density ρ_{CF_4}. The transition energy is $E_0 = 6.154$ eV for the unperturbed CH_3I $6s$ Rydberg transition. The variation between experiment and simulation is caused by other vibrational transitions and by perturber-dependent lifetime broadening not modeled here. While all experimental spectra have been normalized to 1 for comparison with the simulated line shapes, the integrated intensity is independent of ρ_{CF_4}.

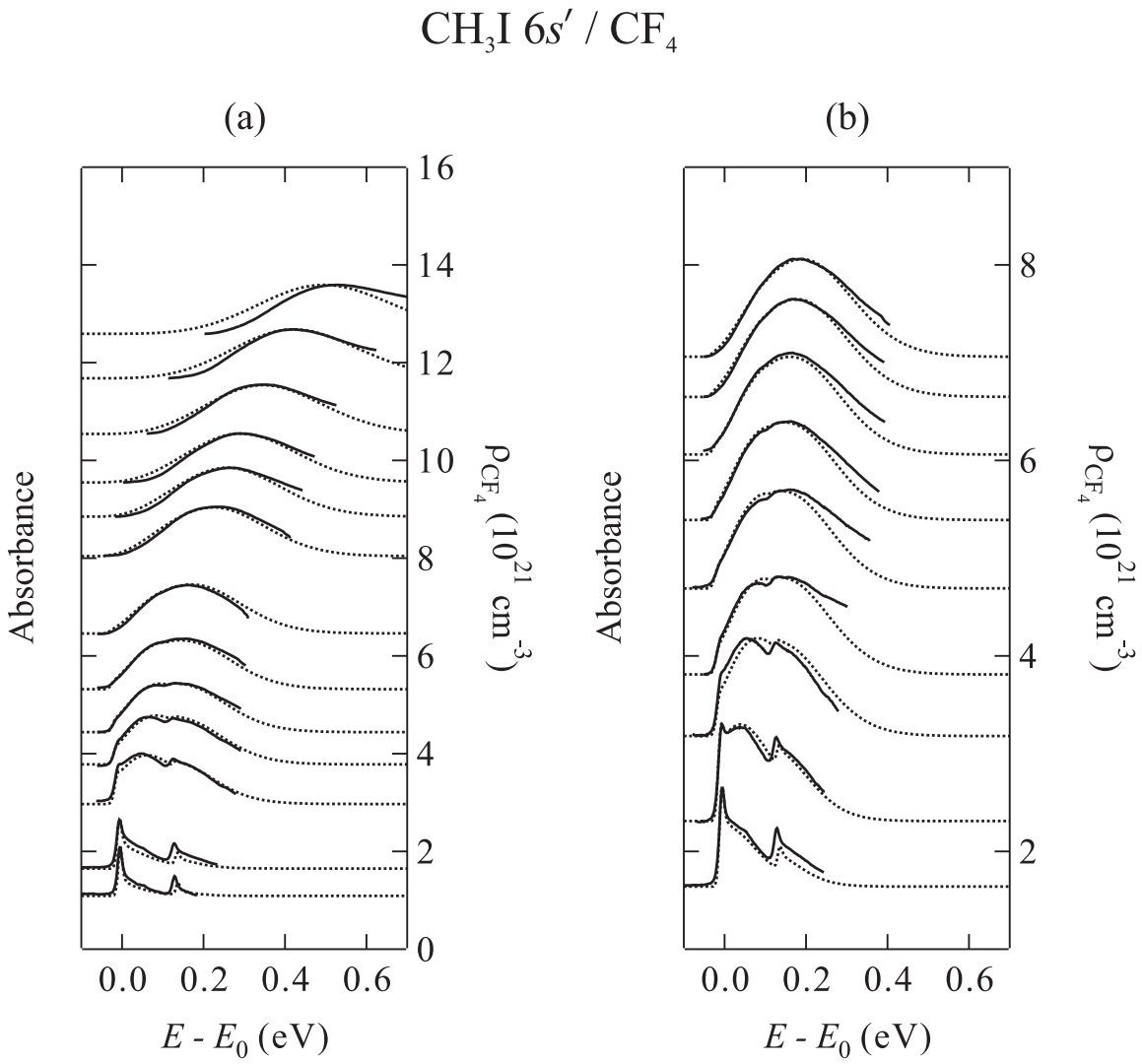

Figure 5.7: Selected photoabsorption spectra (–, relative scale) and simulated line shapes ($\cdots$) for the CH_3I $6s'$ Rydberg transition at (a) non-critical temperatures and (b) on an isotherm ($-44.9°C$) near the critical isotherm. The data are offset vertically by the CF_4 number density ρ_{CF_4}. The transition energy is $E_0 = 6.767$ eV for the unperturbed CH_3I $6s'$ Rydberg transition. The variation between experiment and simulation is caused by other vibrational transitions and by perturber-dependent lifetime broadening not modeled here. While all experimental spectra have been normalized to 1 for comparison with the simulated line shapes, the integrated intensity is independent of ρ_{CF_4}.

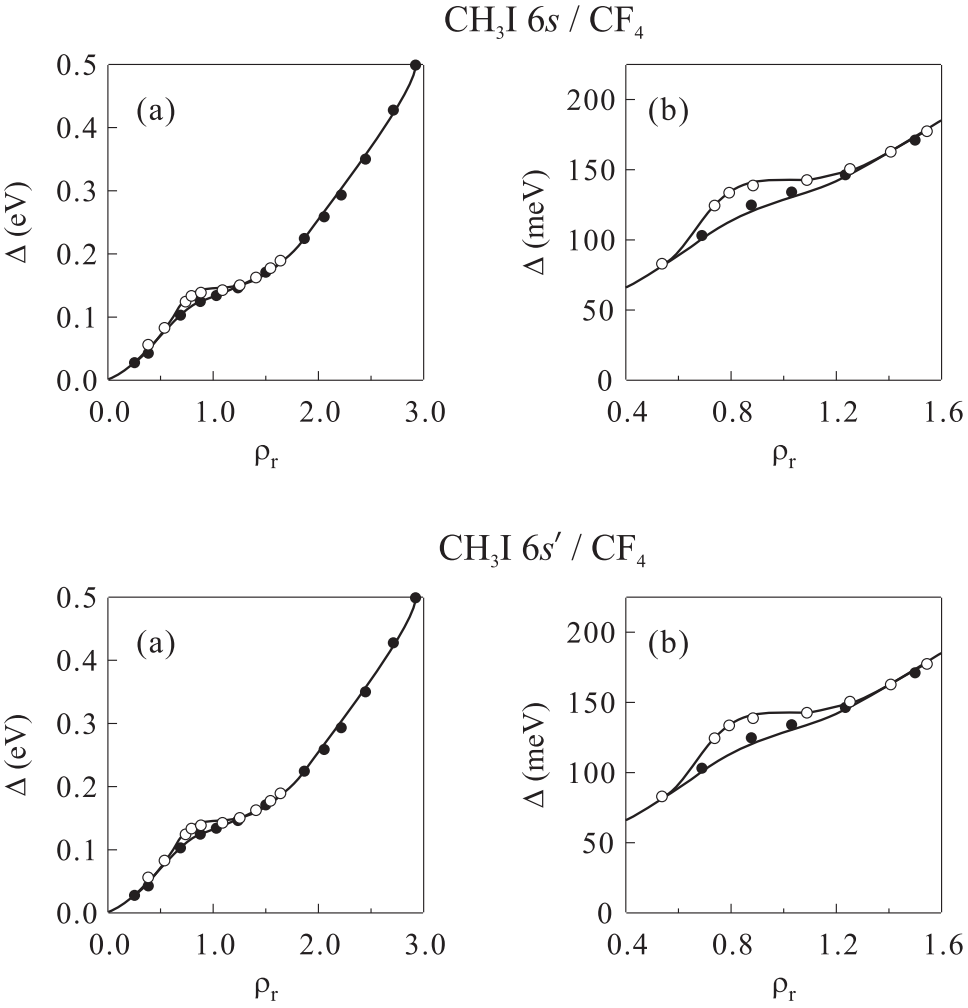

Figure 5.8: (a) The CF_4 induced shift $\Delta(\rho_{CF_4})$ of the CH_3I $6s$ and $6s'$ Rydberg transitions plotted as a function of reduced number density ρ_r at (•) non-critical temperatures and (◦) along an isotherm near the critical isotherm. (b) An expanded view of $\Delta(\rho_{CF_4})$ near the CF_4 critical point. $\rho_c = 4.309\times10^{21}\text{cm}^{-3}$ for CF_4 [83–86]. The solid lines are a visual aid. See text for discussion.

broaden faster in molecular perturbers when compared to atomic perturbers, although the perturber induced shift is comparable.

When comparing the average perturber induced shift $\Delta(\rho_{\mathrm{P}})$ between atomic perturbers and molecular perturbers, we observe that the perturber CF_4 shifts both the atomic and molecular Rydberg transitions to a larger extent than do the other perturbers. According to the law of corresponding states, all gases should deviate from ideal behavior to approximately the same degree, when reduced variables are used. Since all of the gases in this investigation are highly symmetric, the reduced density at the triple point should be similar for them all. This is indeed the case for the rare gases and methane, where the reduced triple point density is approximately 2.65 ± 0.05. However, the reduced triple point density of CF_4 is 3.00. Moreover, the compressibility factor for CF_4 at high densities is significantly smaller than that for Ar and CH_4, indicating that CF_4 is a more attractive gas at high densities. Thus, CF_4 is more compressible and, therefore, is packed closer together at high densities in comparison to the other gases in this study. This higher compressibility should lead to larger local perturber densities in CF_4 around a dopant molecule, which will yield a larger overall blue shift. The weak critical point effect is caused by the low overall critical density of CF_4. Although there is a significant enhancement of the local CF_4 density around the excited dopant when CF_4 is near the critical point, the bulk critical density is 4.28×10^{21} cm^{-3}. Thus, any enhancement at these densities does not yield a large shift.

Explaining the behavior of the methane induced shift $\Delta(\rho_{\mathrm{P}})$ of the dopant Rydberg states in comparison with the atomic gases, however, requires a more complex

argument. As we saw with the atomic systems, the perturber dependent behavior of the $6s$ and $6s'$ CH_3I Rydberg states is insensitive to the changing quadrupole of the dopant cationic core. This is probably caused by the large permanent dipole moment of CH_3I masking the effect of the quadrupole moment. However, comparison of the data in Figs. 4.21 and 4.22 with those in Fig. 5.5 indicates that CH_3I/CH_4 behaves in a manner similar to CH_3I in Kr. Although the intermolecular potential parameters for these two systems are distinctly different, methane and krypton have similar critical densities (i.e., $\rho_c = 6.068 \times 10^{21}$ cm^{-3} for Kr and $\rho_c = 6.587 \times 10^{21}$ cm^{-3} for CH_4) and similar polarizabilities. Thus, the polarizability of the perturber influences the overall shift $\Delta(\rho_R)$. Just as the large critical effect in krypton was driven by the similarities between the well depth of the CH_3I/Kr and Kr/Kr interactions, the well depth of the CH_3I/CH_4 and CH_4/CH_4 interactions are also comparable. We would, however, predict from this simple argument that the CH_3I/Kr system should have a larger critical effect, since the difference between the well depths is smaller. However, the CH_3I/CH_4 system has the stronger critical point effect. This larger effect is caused by the fact that the excited state CH_3I/CH_4 interaction is also comparable to the ground state CH_4/CH_4 interaction. Thus both the ground and excited state CH_3I are strongly stabilized in the supercritical fluid.

5.5 Autocorrelation function study

We have presented experimental and theoretical investigations of the low-n Rydberg states in atomic and molecular perturbers. In the line shape simulation used in this work, the autocorrelation function, given by eq. (3.1), is always truncated to the second term in the density expansion. This second term represents the interaction of

a single dopant molecule with two perturber molecules, or a three-body interaction. Egorov, *et.al.* [53] simulated the $6s$ Rydberg state doped into low density argon with the autocorrelation function truncated to the first term, which represents the interaction of a single dopant with a single perturber (i.e., two-body interactions), but assumed that the three-body correlation would be necessary to model line shapes at higher perturber number densities. The accurate intermolecular potentials obtained in our investigations allow us to probe the truncation effect in a more detailed manner. We have chosen to perform this investigation using the CH_3I $6s$ Rydberg state doped into CH_4, instead of argon, because the broadening and critical effects are larger in CH_4 in comparison to Ar.

Fig. 5.9 presents selected simulated line shapes with the autocorrelation function truncated to the first term A_1 (dotted lines) and to the second term A_2 (solid lines) at non-critical temperatures [c.f. Figs. 5.9(i)- (iii)] and near the critical isotherm [c.f. Fig. 5.9(iv)]. For the simulations at non-critical temperatures, the line shapes obtained by assuming only two-body interactions are identical to those obtained from the assumption of both two-body and three-body interactions, even at high perturber number densities. However, near the critical point, the simulated line shape containing both two-body (i.e., A_1) and three-body (i.e., A_2) interactions is broader than the line shape simulated under the assumption of only two-body interactions. Thus, the increasing correlation length of the perturber near the critical point requires the inclusion of three-body interactions in order to model accurately the dopant absorption line shape. However, as originally predicted by Messing, Raz and Jortner [45,47], the perturber-induced energy shift $\Delta(\rho_P)$ depends only on two-body interactions (cf.

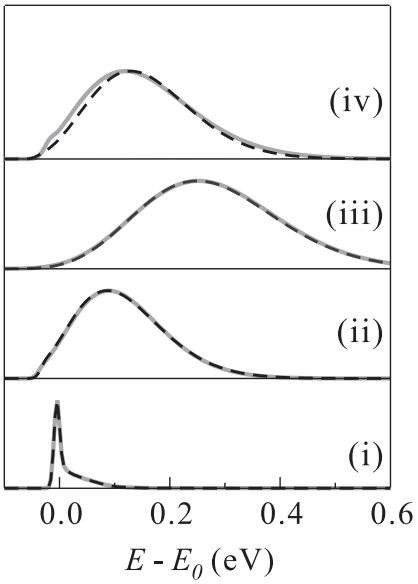

Figure 5.9: Comparison of the simulated line shapes for the CH_3I 6s adiabatic Rydberg transition in CH_4 calculated from eq. (3.2) with the autocorrelation function truncated to the second term A_2 (grey solid line) and truncated to the first term A_1 (black dashed line). The CH_4 densities ρ_{CH_4} presented are (i) the low density 1.16×10^{21} cm^{-3}; (ii) 6.61×10^{21} cm^{-3}, which is near the critical density; and (iii) the density 1.48×10^{22} cm^{-3}, which is near the density of the triple point liquid at non-critical temperatures. A single critical temperature calculation at 6.01×10^{21} cm^{-3} is presented in (iv).

Fig. 5.10), even along the critical isotherm. Moreover, truncation of the autocorrelation function to include only two-body interactions significantly reduces the calculation time (from $30 - 60$ minutes to $1 - 5$ minutes/density point). Thus, future investigations should use the truncated calculation to simulate the dopant absorption line shapes of low-n Rydberg states at non-critical temperatures when adjusting intermolecular potential parameters, and only use the three-body interactions when calculating line-shapes near the critical point of the perturber.

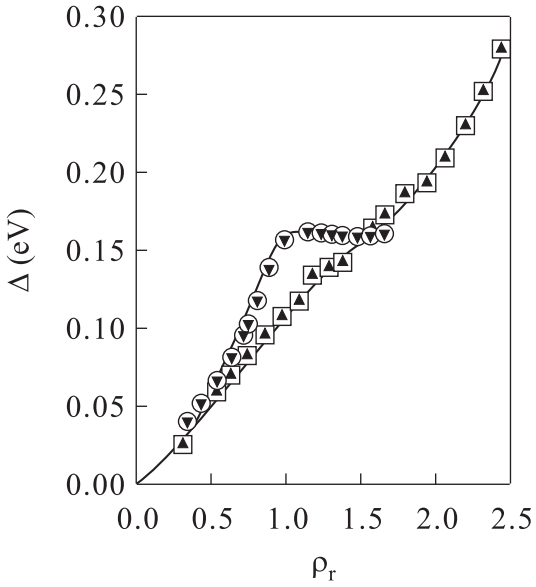

Figure 5.10: Comparison of the first moment of the simulated adiabatic transition for CH_3I in CH_4 calculated from eq. (3.2). The open and closed markers represent the autocorrelation function truncated to the second term A_2 and first term A_1, respectively. (□, ▲) are data obtained at non-critical temperatures, while (○, ▼) are data obtained on an isotherm near the critical isotherm. The solid lines are provided as a visual aid.

5.6 Conclusions

In this chapter, we have presented investigations of various dopant low-n Rydberg states in symmetric molecular perturbers. We showed that the appropriate choice of intermolecular potentials and parameters allowed us to accurately simulate the experimental line shapes. The perturber-induced energy shift $\Delta(\rho_{\rm P})$ in molecular perturbers showed trends similar to those observed in atomic perturbers. However, the large compressibility of CF_4 leads to a larger than expected shift, while the strong CH_3I/CH_4 interactions yielded the largest critical effect observed in these studies. Finally, we showed that two-body interactions are sufficient to model the dopant

absorption line shapes for all perturber densities and temperatures except near the critical point of the perturber.

Chapter 6

Conclusion

In this work, the structure of low-n Rydberg states doped into supercritical fluids was investigated in a myriad of perturbers. Both the experimental absorption spectra and full line shape simulations over the entire perturber density range at non-critical temperatures and along isotherms near perturber critical isotherms were presented for all dopant/perturber systems. These accurate line shape simulations allowed us to extract the perturber-induced energy shift $\Delta(\rho_{\mathrm{P}})$ from the simulated primary low-n Rydberg transitions. These shifts showed a striking critical point effect in all dopant/perturber systems.

In all of the systems presented here, the dopant low-n Rydberg states are extremely sensitive to the nature of the perturbing fluid. When these states are doped into supercritical fluids, the surrounding perturbers interact with the central dopant causing shifts both in the dopant ground state energy and in the excited state energy. At low perturber number densities, the dopant/perturber interaction stabilizes the dopant ground state and the low-n Rydberg state. As the perturber density increases, perturber/dopant interactions causes the formation of a perturber solvent shell around the dopant core, thereby inducing local perturber density inhomogeneities. This solvent shell begins to shield the optical electron from the cationic core. Therefore, the

dense perturber fluid increases the dopant excitation energy, resulting in a blue shift of the abosrption band, which is observed experimentally. The local density of the first perturber solvent shell is almost proportional to the perturber bulk density at non-critical temperatures. However, near the critical isotherm and critical density of the perturber, the dopant/perturber interactions strengthen due to the increased perturber/perturber correlation length. This increased order yields a corresponding increase of the local density in the solvent shell that, in turn, leads to a stronger shielding of the optical electron from the cationic core. Thus, increased blue shifts of the low-n absorption bands are observed in all dopant/perturber systems near the critical point of the perturber. The area of this critical effect is demarcated by the turning points that bound the saddle point in the critical isotherm.

For fluids with similar compressibilities, the structures of low-n dopant Rydberg states in the perturbing fluid show systematic behaviors. At non-critical temperatures, $\Delta(\rho_{\mathrm{P}})$ is determined by the polarizability and size of the perturbing fluid. The larger the polarizability and, therefore, the larger the size, the smaller the perturber-induced energy shift of the dopant absorption bands. This is caused by the number of atoms that can exist between the quasi-free electron and the dopant cationic core, coupled with the strength of the shielding. The large overall energy shift observed in the dopant low-n Rydberg states perturbed by CF_4, on the other hand, was caused by the larger compressibility of CF_4 in comparison to the other gases in this study. This larger compression implies that CF_4 is closer together on average at high perturber number densities than are the other perturbers studied, which increases the local density of CF_4 and, therefore, increases the blue shift in this perturber.

The critical point effect, on the other hand, is dominated by the similarity of the perturber/perturber interaction with the dopant/perturber ground state and dopant/perturber excited state interactions, coupled with the overall local density of the system. In krypton, the well depth of the ground state perturber/perturber intermolecular potential and the dopant/perturber intermolecular potential shows greater similarity in comparison to that in Ar and Xe. Moreover, the excited state CH_3I/Kr interaction is slightly stronger than the ground state Kr/Kr interaction. These facts dictate that the largest critical point effect for CH_3I in atomic perturbers is in Kr. Similarly, the largest overall critical effect was observed in CH_3I/CH_4. This large critical effect is caused by both the ground state and excited state CH_3I/CH_4 interactions having strengths comparable to the CH_4/CH_4 interaction. Although the excited state CH_3I/CF_4 interactions are comparable in strength to the CF_4/CF_4 interactions, the ground state CH_3I/CF_4 interactions are not close to those of CF_4/CF_4. Similarly, the Xe/CF_4 ground state interactions are comparable to the ground state CF_4/CF_4 interactions, but the excited state Xe/ground state CF_4 interactions are weaker. Moreover, the bulk critical density in CF_4 is small in comparison to the rest of the perturbers investigated here. This results in the CF_4 critical effect on $\Delta(\rho_{\mathrm{P}})$ being the smallest one observed.

These data sets also allowed us to generate a consistent set of intermolecular potential parameters for various dopant/perturber systems, which are summarized in Table 6.1. Several general trends in these parameters can be observed. For atomic perturbers, the steepness of the exponential-6 intermolecular potential (i.e., γ) used to model the dopant excited state/perturber intermolecular interaction decreases with

Table 6.1: A summary of the intermolecular potential parameters used to simulate the absorption line shapes in various perturbers.

	$\varepsilon/k_{\mathrm{B}}$ (K)	r_e (Å)	γ
Ar/Ar	119.5	3.826	–
Kr/Kr	172.7	4.031	–
Xe/Xe	229.0	4.552	–
CH_4/CH_4[a]	141.5	3.704	–
CF_4/CF_4	181.02	4.708	–
Xe/Ar	200.0	4.265	–
XeAr/Ar	195.0	4.310	–
Xe/CF_4	199.3	4.629	–
CH_3I/Ar	162.2	4.572	–
CH_3I/Kr	196.7	4.676	–
CH_3I/Xe	297.5	4.896	–
CH_3I/CH_4	195.8	4.243	–
CH_3I/CF_4	256.0	5.016	–
Xe $6s$/Ar	300.0	5.20	16.00
Xe $6s/CF_4$	135.0	6.55	12.25
CH_3I $6s$/Ar	110.0	6.30	12.75
CH_3I $6s$/Kr	245.0	6.20	11.30
CH_3I $6s$/Xe	400.0	6.39	10.25
CH_3I $6s/CH_4$	145.0	6.55	10.10
CH_3I $6s/CF_4$	185.0	6.84	12.10
Xe $6s'$/Ar	400.0	4.98	16.00
CH_3I $6s'$/Ar	110.0	6.30	12.75
CH_3I $6s'$/Kr	245.0	6.20	11.30
CH_3I $6s'$/Xe	400.0	6.29	10.25
CH_3I $6s'/CH_4$	145.0	6.55	10.10
CH_3I $6s'/CF_4$	185.0	6.84	12.10
Xe($6s$)Ar/Ar	250.0	5.25	16.00
CH_3I $6s$ ν_2/Ar	150.0	6.30	12.15
CH_3I $6s$ ν_2/Kr	225.0	6.30	10.75
CH_3I $6s$ ν_2/Xe	360.0	6.50	9.50
CH_3I $6s$ ν_2/CH_4	105.0	6.65	9.95
CH_3I $6s$ ν_2/CF_4	135.0	6.84	11.90
CH_3I $6s'$ ν_2/Ar	150.0	6.30	12.15
CH_3I $6s'$ ν_2/Kr	225.0	6.30	10.75
CH_3I $6s'$ ν_2/Xe	360.0	6.35	9.50
CH_3I $6s'$ ν_2/CH_4	105.0	6.65	9.95
CH_3I $6s'$ ν_2/CF_4	135.0	6.84	11.90

[a] Two-Yukawa potential with $\kappa_0 = 8.50$ Å, $z_1 = 0.90$ Å^{-1}, and $z_2 = 4.25$ Å^{-1}.

increasing perturber size and polarizability. This trend is reversed in molecular perturbers, were the larger, more compressible CF_4 has a steeper repulsive component in comparison to CH_4. The excited vibrational states of CH_3I always have exponential-6 potentials with a smaller γ in comparison to the CH_3I adiabatic transition in the same perturbing gas. Moreover, the vibrational states always have an equilibrium collision radius that is identical or larger than the collision radius of the adiabatic transition. The excited state collision radii are always larger than the ground state collision radii, as one would expect. However, the interaction strength of the excited state (as gauged by the well depth) can be stronger or weaker than that for the ground state of the same system. These changing interactions are what dominate the variations observed in the critical effects for each of the dopant/perturber systems investigated here.

An understanding of the structure of low-n Rydberg states in supercritical fluids is an important tool in the investigation of solvation effects, since these studies can yield accurate dopant/perturber ground state and excited state intermolecular potentials. We conclude from the present work that the absorption line shapes can be adequately simulated within a simple semi-classical line shape analysis. However, this work focused on highly symmetric perturbers. Future studies should concern more asymmetric perturbers and polar perturbers. Such an extension will require changing the calculation techniques involved in determining the radial distribution functions as well as the type of Fourier transform used to simulate the line shape. Since the excited state is sensitive to the structure of the perturbing fluid, we anticipate that multi-site intermolecular potentials and angular dependent intermolecular potentials

will need to be used as the perturber complexity increases, in order to model the full line shape accurately.

References

[1] R. Noyori, "Supercritical fluids: introduction," Chem. Rev. 99, 353 (1999).

[2] C. L. Phelps, N. G. Smart, C. M. Wai, "Past, present, and possible future applications of supercritical fluid extraction technology," J. Chem. Ed. 73, 1163 (1996), and references therein.

[3] J. R. Dean, S. Hitchen, eds., *Applications of Supercritical Fluids in Industrial Analysis* (Springer, New York, 1993), and references therein.

[4] J. R. Williams, A. A. Clifford, eds., *Supercritical Fluids: Methods and Protocols* (Humana Press, New Jersey, 2000), and references therein.

[5] L. B. Davenhall, J. B. Rubin, "Composition and method for removing photoresist materials from electronic components," Patent No. US 6, 403, 544 B1, (2002).

[6] P. York, "Strategies for particle design using supercritical fluid technologies," Pharm. Sci. Technol. Today 2, 430 (1999).

[7] P. R. Loconto, ed., *Trace Environmental Quantitative Analysis: Principles, Techniques, and Applications* (Marcel Dekker, New York, 2001), and references therein.

[8] J. R. Dean, ed., *Extraction Methods for Environmental Analysis* (Wiley, New York, 1998), and references therein.

[9] M. Poliakoff, J. M. Fitzpatrick, T. R. Farren, P. T. Anastas, "Green chemistry: science and politics of change," Science 297, 807 (2002).

[10] V. K. Jain, "Supercritical fluids tackle hazardous wastes," Environ. Sci. Technol. 27, 806 (1993).

[11] K. Anton, C. Berger, eds., *Supercritical Fluid Chromatography with Packed Columns: Techniques and Applications* (CRC Press, New York, 1998), and references therein.

[12] A. Baiker, "Supercritical fluids in heterogeneous catalysis," Chem. Rev. 99, 453 (1999).

[13] P. G. Jessop, T. Ikariya, R. Noyori, "Homogeneous catalysis in supercritical fluids," Chem. Rev. 99, 475 (1999).

[14] J. A. Darr, M. Poliakoff, "New directions in inorganic and metal-organic coordination chemistry in supercritical fluids," Chem. Rev. 99, 495 (1999).

[15] A. J. Mesiano, E. J. Beckman, A. J. Russell, "Supercritical biocatalysis," Chem. Rev. 99, 623 (1999).

[16] J. L. Kendall, D. A. Canelas, J. L. Young, J. M. DeSimone, "Polymerizations in supercritical carbon dioxide," Chem. Rev. 99, 543 (1999).

[17] C. F. Kirby, M. A. McHugh, "Phase behavior of polymers in supercritical fluid solvents," Chem. Rev. 99, 565 (1999).

[18] J. F. Brennecke, J. E. Chateauneuf, "Homogeneous organic reactions as mechanistic probes in supercritical fluids," Chem. Rev. 99, 433 (1999).

[19] P. E. Savage, "Organic chemical reactions in supercritical water," Chem. Rev. 99, 603 (1999).

[20] O. Kajimoto, "Solvation in supercritical fluids: its effects on energy transfer and chemical reactions," Chem. Rev. 99, 355 (1999), and reference therein.

[21] M. B. Robin, *Higher Excited States of Polyatomic Molecules* Vol.I-Vol.III (Academic Press, New York, 1974, 1975, 1985), and references therein.

[22] R. Reininger, U. Asaf, I. T. Steinberger, S. Basak, "Relationship between the energy V_0 of the quasi-free-electron and its mobility in fluid argon, krypton, and xenon," Phys. Rev. B 28, 4426 (1983).

[23] R. Reininger, U. Asaf, I. T. Steinberger, "The density dependence of the quasi-free electron state in fluid xenon and krypton," Chem. Phys. Lett. 90, 287 (1982).

[24] A. O. Allen, W. F. Schmidt, "Determination of the energy level V_0 of electrons in liquid argon over a range of densities," Z. Naturforsch. 37a, 316 (1982).

[25] W. von Zdrojewski, J. G. Rabe, W. F. Schmidt, "Photoelectric determination of V_0-values in solid rare gases," Z. Naturforsch. 35a, 672 (1980).

[26] B. Halpern, J. Lekner, S. A. Rice, R. Gomer, "Drift velocity and energy of electrons in liquid argon," Phys. Rev. 156, 351 (1967).

[27] W. Tauchert, H. Jungblut, W. F. Schmidt, "Photoelectric determination of V_0 values and electron ranges in some cryogenic liquids," Can. J. Chem. 55, 1860 (1977).

[28] J. R. Broomall, W. D. Johnson, D. G. Onn, "Density dependence of the electron surface barrier for fluid helium-3 and helium-4," Phys. Rev. B 14, 2819 (1976).

[29] J. Jortner, A. Gaathon, "Effects of phase density on ionization processes and electron localization in fluids," Can. J. Chem. 55, 1801 (1977).

[30] N. Schwenter, E. -E. Koch, J. Jortner, *Electronic Excitations in Condensed Rare Gases* (Springer-Verlag, Berlin, 1985), p.75.

[31] U. Asaf, R. Reininger, I. T. Steinberger, "The energy V_0 of the quasi-free electron in gaseous, liquid, and solid methane," Chem. Phys. Lett. 100, 363 (1983).

[32] C. M. Evans, G. L. Findley, "Energy of the quasifree electron in argon and krypton," Phys. Rev. A 72, 022717 (2005).

[33] C. M. Evans, G. L. Findley, "Energy of the quasi-free electron in supercritical argon near the critical point," Chem. Phys. Lett. 410, 242 (2005).

[34] C. M. Evans, G. L. Findley, "Field ionization of C_2H_5I in supercritical argon near the critical point," J. Phys. B: At. Mol. Opt. Phys. 38, L269 (2005).

[35] Luxi Li, C. M. Evans, G. L. Findley, "Energy of the quasi-free electron in supercritical krypton near the critical point," J. Phys. Chem. A 109, 10683 (2005).

[36] Xianbo Shi, Luxi Li, C. M. Evans, G. L. Findley, "Energy of the quasi-free electron in xenon," Chem. Phys. Lett. 432, 62 (2006).

[37] Xianbo Shi, Luxi Li, C. M. Evans, G. L. Findley, "Energy of the quasi-free electron in argon, krypton and xenon," Nucl. Inst. Meth. A 582, 270 (2007).

[38] Xianbo Shi, Luxi Li, G. M. Moriarty, C. M. Evans, G. L. Findley, "Energy of the quasi-free electron in low density Ar and Kr: extension of the local Wigner-Seitz model," Chem. Phys. Lett. 454, 12 (2008).

[39] Xianbo Shi, Luxi Li, C. M. Evans, G. L. Findley, "Energy of the excess electron in methane and ethane,"in preparation.

[40] G. D. Mahan, "Satellite bands in alkali-atom spectra," Phys. Rev. A 6, 1273 (1972).

[41] M. Lax, "The Franck-Condon principle and its application to crystals," J. Chem. Phys. 20, 1752 (1952).

[42] R. Granier, M. C. Castex, J. Granier, J. Romand, "Perturbation of the xenon 1469 A. resonance line by various rare gases and hydrogen," C. R. Acad. Sci. Ser. B 264, 778 (1967).

[43] M. C. Castex, R. Granier, J. Romand, "Perturbation of the 1236-A. resonance line of krypton and the 1295-A. resonance line of xenon by various rare gases," C. R. Acad. Sci. Ser. B 268, 552 (1969).

[44] M. C. Castex, "Absorption spectra of xenon-rare gas mixtures in the far UV region (1150-1500 Å): high resolution analysis and first quantitative absorption measurements," J. Chem. Phys. 66, 3854 (1977).

[45] I. Messing, B. Raz, J. Jortner, "Medium perturbations of atomic extravalence excitations," J. Chem. Phys. 66, 2239 (1977).

[46] I. Messing, B. Raz, J. Jortner, "Solvent perturbations of extravalence excitations of atomic xenon by rare gases at high pressures," J. Chem. Phys. 66, 4577 (1977).

[47] I. Messing, B. Raz, J. Jortner, "Perturbations of molecular extravalence excitations by rare-gas fluids," Chem. Phys. 25, 55 (1977).

[48] I. Messing, B. Raz, J. Jortner, "Medium effects on the vibrational structure of some molecular Rydberg excitations," Chem. Phys. 23, 351 (1977).

[49] A. M. Halpern, "Iterative Fourier reconvolution spectroscopy: van der Waals broadening of Rydberg transitions; the ∼B ← ∼X (5p, 6s) transition of methyl iodide," J. Phys. Chem. 96, 2448 (1992).

[50] T. Kalbfleisch, R. Fan, J. Roebber, P. Moore, E. Jacobson, L.D. Ziegler, "A molecular dynamics study of electronic absorption line broadening in high-pressure nonpolar gases," J. Chem. Phys. 103, 7673 (1995).

[51] R. Fan, T. Kalbfleisch, L. D. Ziegler, "A molecular dynamics analysis of resonance emission: optical dephasing and inhomogeneous broadening of CH_3I in CH_4 and Ar," J. Chem. Phys. 104, 3886 (1996).

[52] T. S. Kalbfleisch, L. D. Ziegler, T. Keyes, "An instantaneous normal mode analysis of solvation: methyl iodide in high pressure gases," J. Chem. Phys. 105, 7034 (1996).

[53] S. A. Egorov, M. D. Stephens, J. L. Skinner, "Absorption line shapes and solvation dynamics of CH_3I in supercritical Ar," J. Chem. Phys. 107, 10485 (1997).

[54] E. Morikawa, A. M. Köhler, R. Reininger, V. Saile, P. Laporte, "Medium effects on valence and low-n Rydberg states: NO in argon and krypton," J. Chem. Phys. 89, 2729 (1988).

[55] P. Larrégaray, A. Cavina, M. Chergui, "Ultrafast solvent response upon a change of the solute size in non-polar supercritical fluids," Chem. Phys. 308, 13 (2004).

[56] C. N. Tiftickjian, S. A. Egorov, "Absorption and emission lineshapes and solvation dynamics of NO in supercritical Ar," J. Chem. Phys. 128, 114501 (2008).

[57] Luxi Li, Xianbo Shi, C. M. Evans, G. L. Findley, "Xenon low-n Rydberg states in supercritical argon near the critical point," Chem. Phys. Lett. 461, 207 (2008).

[58] Luxi Li, Xianbo Shi, C. M. Evans, G. L. Findley, "CH_3I low-n Rydberg states in supercritical atomic fluids near the critical point," Chem. Phys., in press.

[59] Luxi Li, Xianbo Shi, C. M. Evans, G. L. Findley, "Low-n Rydberg states in supercritical molecular fluids: CF_4 and CH_4," in preparation.

[60] S. C. Tucker, "Solvent density inhomogeneities in supercritical fluids," Chem. Rev. 99, 391 (1999), and references therein.

[61] Y. -P. Sun, ed., *Supercritical Fluid Technology in Material Science and Engineering: Syntheses, Properties and Applications* (Dekker, New York, 2002).

[62] Y. Arai, T. Sako, Y. Takebayashi, ed., *Supercritical Fluids: Molecular Interactions, Physical Properties, and New Applications* (Springer-Verlag, Berlin, 2002).

[63] J. P. Cason, K. Khambaswadkar, C. B. Roberts, "Supercritical fluid and compressed solvent effects on metallic nanoparticle synthesis in reverse micelles," Ind. Eng. Chem. Res. 39, 4749 (2000).

[64] Y. Zhang, C. Erkey, "Preparation of supported metallic nanoparticles using supercritical fluids: a review," J. Supercritical Fluids 38, 252 (2006), and references therein.

[65] P. Attard, "Spherically inhomogeneous fluids. I. Percus-Yevick hard spheres: osmotic coefficients and triplet correlations," J. Chem. Phys. 91, 3072 (1989).

[66] P. Attard, "Spherically inhomogeneous fluids. II. Hard-sphere solute in a hard-sphere solvent," J. Chem. Phys. 91, 3083 (1989).

[67] J. Zhang, D. P. Roek, J. E. Chateauneuf, J. F. Brennecke, "A steady-state and time-resolved fluorescence study of quenching reactions of anthracene and 1,2-benzanthracene by carbon tetrabromide and bromoethane in supercritical carbon dioxide," J. Am. Chem. Soc. 119, 9980 (1997).

[68] Y. Sun, M. A. Fox, K. P. Johnston, "Spectroscopic studies of p-(N,N-dimethylamino)benzonitrile and ethyl p-(N,N-dimethylamino)benzoate in supercritical trifluoromethane, carbon dioxide, and ethane," J. Am. Chem. Soc. 114, 1187 (1992).

[69] R. S. Urdahl, D. J. Myers, K. D. Rector, P. H. Davis, B. J. Cherayil, M. D. Fayer, "Vibrational lifetimes and vibrational line positions in polyatomic supercritical fluids near the critical point," J. Chem. Phys. 107, 3747 (1997).

[70] R. S. Urdahl, K. D. Rector, D. J. Myers, P. H. Davis, M. D. Fayer, "Vibrational relaxation of a polyatomic solute in a polyatomic supercritical fluid near the critical point," J. Chem. Phys. 105, 8973 (1996).

[71] T. F. Gallagher, *Rydberg Atoms* (Cambridge University Press, Cambridge, 1994), and the references therein.

[72] R. P. Futrelle, "Unified theory of spectral line broadening in gases," Phys. Rev. A 5, 2162 (1972).

[73] J. K. Percus, in: H. L. Frisch, S. L. Lebowitz (Eds.) *Classical Fluids* (Benjamin, New York, 1964).

[74] M. Born, H. S. Green, "A general kinetic theory of liquids. I. The molecular distribution functions," Proc. R. Soc. London Ser. A 188, 10 (1946).

[75] R. Kubo, Y. Toyozawa, "Application of the method of generating function to radiative and non-radiative transitions of a trapped electron in a crystal," Prog. Theo. Phys. Japan 13, 160 (1955).

[76] H. C. Jacobson, "Moment analysis of atomic spectral lines," Phys. Rev. A 4, 1363 (1971)

[77] C. M. Evans, *Subthreshold Photoionization in Molecular Dopant/perturber Systems*, Ph.D. Dissertation, Louisiana State University, Baton Rouge, LA, 2001; see also C. M. Evans, J. D. Scott, and G. L. Findley, Rec. Res. Chem. Phys. 3, 351 (2002).

[78] T. R. Strobridge, "The thermodynamic properties of nitrogen from 64 to 300 °K between 0.1 and 200 atmospheres," Tech. Note 129, Nat. Bur. Std. (U.S.) (1962).

[79] A. L. Gosman, R. D. McCarty, J. G. Hust, "Thermodynamics properties of argon from the triple point to 300 K at pressures to 1000 atmostpheres," Tech. Note 27, Nat. Bur. Std. (U.S.) (1969).

[80] W. B. Streett, L. A. K. Straveley, "Experimental study of the equation of state of liquid krypton," J. Chem. Phys. 55, 2495 (1971).

[81] W. B. Streett, L. S. Sagan, L. A. K. Staveley, "Experimental study of the equation of state of liquid xenon," J. Chem. Thermodynamics 5, 633 (1973) .

[82] B. A. Younglove, J. F. Ely, "Thermophysical properties of fluids. II. Methane, ethane, propane, isobutane, and normal butane," J. Phys. Chem. Ref. Data, 16, 577 (1987).

[83] T. E. Morsy, "Extended Benedict-Webb-Rubin equation of state. Application to eight fluorine compounds," J. Chem. Eng. Data, 15, 256 (1970).

[84] H. Orbey, S. I. Sandler, "Equation of state modeling of refrigerant mixtures," Ind. Eng. Chem. Res. 34, 2520 (1995).

[85] N. B. Wilding, "Critical-point and coexistence-curve properties of the Lennard-Jones fluid: a finite-size scaling study," Phys. Rev. E, 52, 602 (1995).

[86] J. M. Caillol, "Critical-point of the Lennard-Jones fluid: a finite-size scaling study," J. Chem. Phys. 109, 4885 (1998).

[87] E. W. Grundke, D. Henderson, R. D. Murphy, "Evaluation of the Percus-Yevick theory for mixtures of simple liquids," Can. J. Phys. 51, 1216 (1973).

[88] W. H. Press, S. A. Teukolsky, W. T. Vetterling, and B. P. Flannery, *Numerical Recipes in FORTRAN: The Art of Scientific Computing* (Cambridge University Press, New York, 1992).

[89] Xianbo Shi, *Energy of the Quasi-free Electron in Atomic and Molecular Fluids*, Ph.D. Dissertation, The Graduate Center of the City University of New York, New York, NY, 2009.